

职称申报材料附件

姓名：王斌

单位：控制科学与工程学院

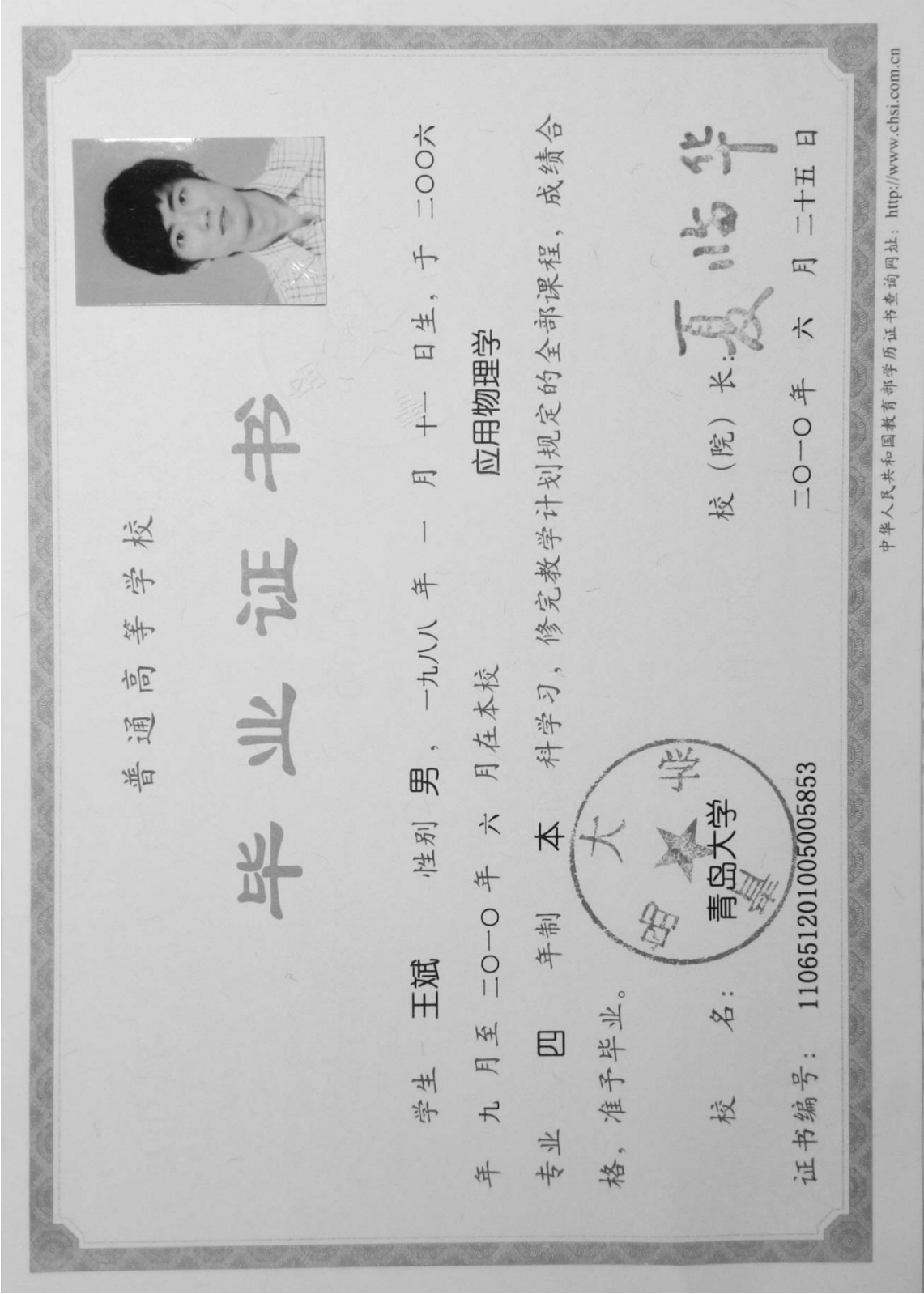
2020 年 03 月
中国石油大学（华东）

目 录

1. 学历和学位证书	1
1.1 本科	1
1.2 硕博	3
2. 岗前培训合格证书	5
3. 班主任、学业导师工作经历	7
3.1 聘书及聘用证明	7
3.2 优秀班主任证明	9
4. 收录证明及全文	13
4.1 论文收录证明	13
4.2 论文全文	20
5. 专利授权证书	69
6. 项目合同书、任务书	71
6.1 主持国家自然科学基金（41704124）	71
6.2 主持山东省自然科学基金（ZR2017BEE026）	77
6.3 主持山东省重点研发计划（2018GGX101020）	79
6.4 主持自主创新计划（15CX02120A）	88
6.5 主持自主创新计划（18CX02112A）	104
6.6 主持校级教改项目（QN201813）	110
6.7 参与校级教改项目（QN201516）	126
6.8 参与山东省自然科学基金（ZR2019MEE095）	131
7. 教学比赛获奖证明材料	133
7.1 校级教学比赛获奖	133
7.2 院级教学比赛获奖	134
8. 指导学生学位论文获得校优秀论文	135
9. 参与平台、课程建设证明材料	136
9.1 作为骨干参与《测量仪表与自动化》在线开放课程建设	136
9.2 主持《测控技术与测控网络系统》、《电磁场与微波技术》在线课程建设	141
9.3 作为骨干参与《测量仪表与自动化》国家级一流在线课程申报	142
10. 参加国际学术会议证明材料	146
11. 其他证明材料	149
11.1 青年教师卓越教学能力培养计划	149
11.2 优秀工会会员	150
11.3 积极参加集体活动，代表学院取得优异成绩	151

1. 学历和学位证书

1.1 本科





学士学位证书

青岛大学

王斌，男，1988年1月11日生。在

应用物理学

专业完成了本科学学习计划，业已

毕业，经审核符合《中华人民共和国学位条例》的规定，授予

理学

学士学位。

校 长

青岛大学

夏临华

学位评定委员会主席

证书编号：1106542010005853

二〇一〇年六月二十五日

(普通高等教育本科毕业生)



博士研究生 毕业证书			
研究生 王斌	性别 男	1988 年 01 月 11 日生	于
2010 年 09 月至	2015 年 06 月	在	无线电物理
专业学习，学制 五 年，修完博士研究生培养计划规定的全部课程，成绩合格，			
毕业论文答辩通过，准予毕业。			
培养单位： 山 东 大 学	校(院、所)长： 张荣		
证书编号：104221201501000241	2015 年 06 月 30 日		

中华人民共和国教育部学历证书查询网址：<http://www.chsi.com.cn>



博士学位证书

王斌，男，1988年01月11日生。在山东大学

无线电物理

学科(专业)已通过博士学位的课程

考试和论文答辩，成绩合格。根据《中华人民共和国学位条例》的规

定，授予理学博士学位。

山东大学

校长

张荣


学位评定委员会主席



证书编号:10422222015100245

二〇一五年六月十六日


2. 岗前培训合格证书



结业证书

编号: 2016037

王斌同志, 于 2015-2016 学年
参加学校组织的青年教师上岗培训, 考核
合格, 准予结业, 特发此证。



中国石油大学(华东)
二〇一六年六月

培训内容

模 块	内 容
师德修养与职业 规划	专题讲座: 谈高校青年教师专业发展的路径与策略
	名师工作坊: 高校青年教师成长与发展的自我意识
教学热点与理念	专题讲座: 我思我行我 MOOC
	专题讲座: 开放式研究性教学
	教学工作坊: 校级教学名师讲坛
	专题讲座: 浅谈驾驭课堂的动力与能力
	专题讲座: 构建以学生为中心、鲜活、高效的课堂
课堂设计与实施	教学公开课 5 次
	课堂观摩 20 学时
	教案展评
教学方法与技巧	试讲点评 2 次
	专题讲座: 减轻声带压力, 科学运用嗓音
	专题讲座: 吸引学生上课兴趣的方法和手段
	教学工作坊: 基本教学技巧
	教学工作坊: 如何写好教案与板书
现代教学技术	专题讲座: 多媒体课件 PPT 的制作技巧
	教学工作坊: 如何更有效地使用校内网络资源
	教学工作坊: 智慧教室的使用
其 他	视频讲座; 参观考察; 教学沙龙; 座谈会

编号: 201611112

山东省高等学校教师岗前培训考试暨教师资格笔试合格证



王斌 同志参加2016年度
山东省高等学校教师岗前培训。
经考试，成绩合格。特发此证。

姓名: 王斌

性别: 男

身份证号: 370702198801112215

工作单位: 中国石油大学(华东)

发证单位:

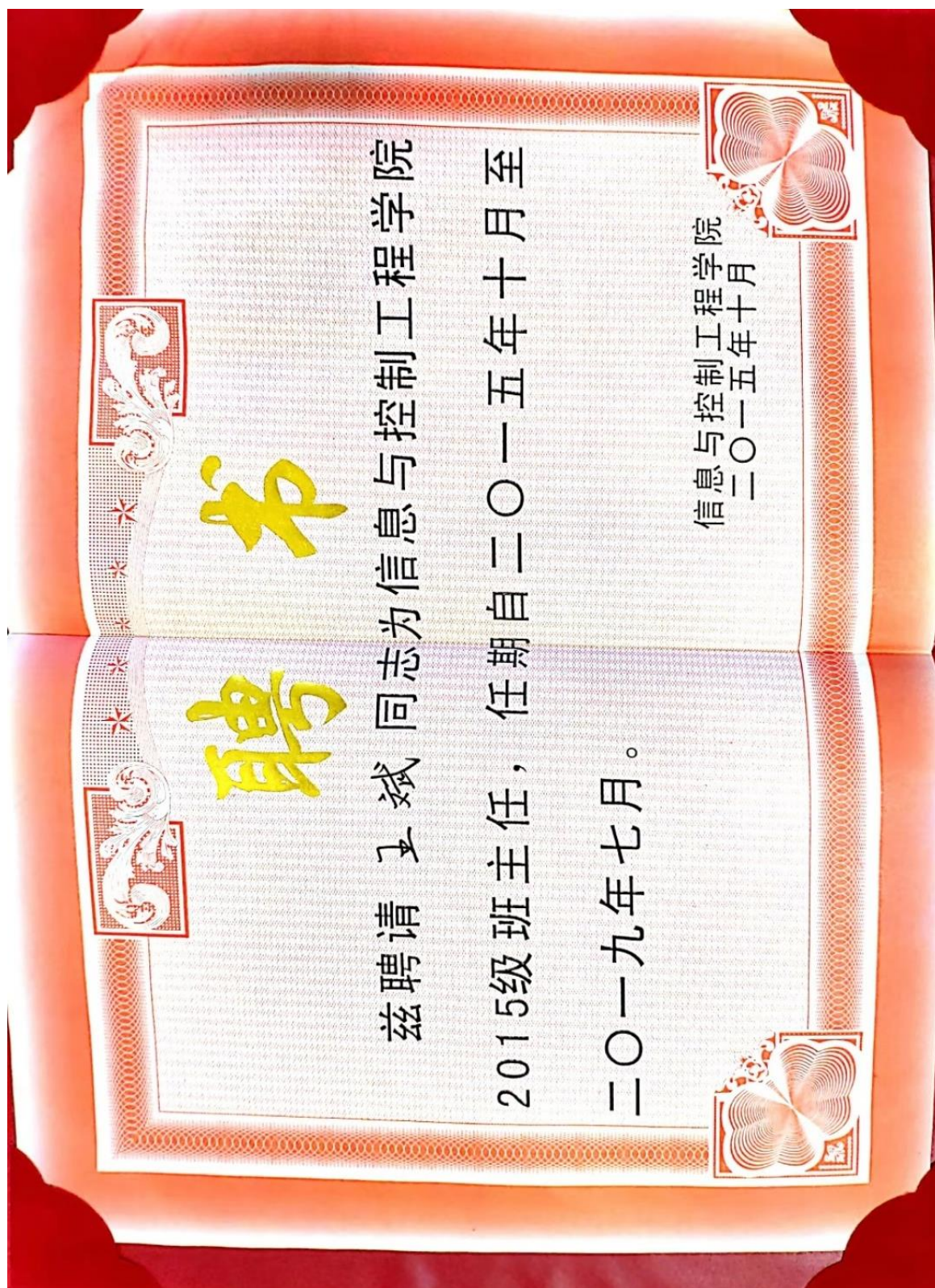


2016年6月10日

山东省教育厅制

3. 班主任、学业导师工作经历

3.1 聘书及聘用证明



控制科学与工程学院
学业导师/班主任任职经历及考核证明

王斌同志与 2015 年 09 月至 2019 年 06 月担任测控专业 1502 班班主任，与 2017 年 12 月参加学院的学业班主任考核，考核结果为优秀。与 2017 年 09 月至今担任测控专业 1702 班学业导师，与 2019 年 12 月参加学院的学业导师考核，考核结果为合格。与 2017 年 09 月至今担任自动化专业 1703 班学业导师，与 2019 年 12 月参加学院的学业导师考核，考核结果为合格。

特此证明！



中国石油大学 党委学生工作部 学 生 工 作 处

学工〔2017〕14 号

关于公布 2016—2017 学年 “十佳百优” 班主任名单的通知

各有关单位：

2016—2017 学年，我校广大教职员工坚持贯彻学校《关于进一步加强和改进学生工作队伍建设的实施意见》（中石大东党〔2011〕29 号），牢固树立“关爱学生、尊重学者、崇尚学术”的价值追求，立德树人，爱岗敬业，积极从事班主任工作，在培养学生科学研究意识、拓展学生创新实践能力、指导学生学业职业规划、促进学生全面健康发展等方面发挥了重要作用，得到了广大学生的认可和欢迎，涌现了一批思想素质好、业务水平高、奉献精神强的先进典型。

经学院（部）推荐、学校评选，杨国权等 10 人被评为 2016-2017 学年“十佳班主任”。经学院评选推荐、学校审核，丁修建等 100 人被评为 2016-2017 学年“优秀班主任”。为表彰

—1—

先进，树立榜样，现将名单（附后）予以公布。

希望全体“十佳百优”班主任珍惜荣誉，再接再厉，充分发挥模范带头作用，为学校事业发展和学生成长成才做出更大贡献。希望广大教职员工向“十佳百优”班主任学习，把思想政治工作贯穿教育教学全过程，实现全员育人、全程育人、全方位育人，培育一流人才，助力学校一流学科建设。

党委学生工作部（处）

2017年12月4日

附件

2016—2017 学年“十佳百优”班主任名单

十佳班主任（10 人）

地球科学与技术学院： 杨国权
石油工程学院： 孟红霞
化学工程学院： 曲 燕
机电工程学院： 殷晓康
信息与控制工程学院： 张丽霞
储运与建筑工程学院： 张克舫
计算机与通信工程学院： 何旭莉
经济管理学院： 王菊娥
理学院： 周小岩
文学院： 孙玉超

优秀班主任（100 人）

地球科学与技术学院（10 人）：

丁修建 樊彦国 国景星 孟凡超 宋冬梅 谭宝海 王 健
张福明 张 凯 宗兆云

石油工程学院（9 人）：

陈付真 樊泽霞 李昌良 刘玉泉 齐 宁 杨永飞 姚传进
张 伟 张黎明

化学工程学院（16 人）：

丁 雪 于英民 刘兆增 孙治谦 宋春敏 巩志强 张玉财

徐书根 李 传 李大伟 章大海 薄守石 赫佩军 赵青山
陈 坤 夏 薇

机电工程学院（13人）：

赵 严 孔得朋 朱红卫 王彦富 邹宇鹏 刘秀全 李 伟
李 安 黄万群 韩 涛 李学达 马 宁 崔运静

信息与控制工程学院（9人）：

刘希臣 张 旭 董超群 姜向远 张冬至 赵仁德 华陈权
王 斌 刘伟锋

储运与建筑工程学院（11人）：

周明芳 孙广宇 宋 明 张 伟 张 能 张雪松 徐会金
徐春雯 李 欣 王鸿膺 高 伟

计算机与通信工程学院（7人）：

刘培刚 卢晓轩 叶端南 王 勃 王雷全 邵明文 李 永

经济管理学院（7人）：

刘丙泉 刘 慧 张 涛 李 延 王 娟 齐建民 陈月璇

理学院（12人）：

付殿岭 刘学锋 刘超卓 卢玉坤 张 健 李 明 李 静
王创业 贾玉磊 赵春娥 邵红梅 陈艳丽

文学院（5人）：

朱 珊 伊 强 林 超 杨 军 张 楠

体育教学部（1人）：

马大刚

党委学生工作部（处）

2017年12月4日印发

4. 收录证明及全文

4.1 论文收录证明

中国石油大学查收查引

报告编号: 202000095

论文检索报告

被检索人单位: 中国石油大学(华东)

被检索人: 王斌

检索数据库: SCIE (SCI)

检索结果: 收录 2 篇。

特此证明, 详见附件。

注:

1. 该报告检索论文均由被检索人提交并得到被检索人确认。
2. 不排除姓名相同、姓名拼写相同的情况。

中国石油大学(华东)图书馆

2020 年 1 月 6 日

报告编号: 202000095

附件1

1

A Borehole Fluid Saturation Evaluation Method Using Unidirectional Monopole UWB Antenna

作者: Wang, B(Wang, Bin);Li, K(Li, Kang);Kong, FM(Kong, Fan-Min);Zhao, J(Zhao, Jia);Gao, Y(Gao, Yang);

来源出版物: IEEE GEOSCIENCE AND REMOTE SENSING LETTERS 卷: 12 期: 2 页码范围: 429-433 出版年: 2015

通讯作者地址: Wang, B (reprint author), Shandong Univ, Sch Informat Sci & Engn, Jinan 250100, Peoples R China.

地址: 1. [Wang, Bin]Shandong Univ, Sch Informat Sci & Engn, Jinan 250100, Peoples R China.

2. [Li, Kang]Shandong Univ, Sch Informat Sci & Engn, Jinan 250100, Peoples R China.

3. [Kong, Fan-Min]Shandong Univ, Sch Informat Sci & Engn, Jinan 250100, Peoples R China.

4. [Zhao, Jia]Shandong Univ, Sch Informat Sci & Engn, Jinan 250100, Peoples R China.

5. [Gao, Yang]Shandong Univ, Sch Informat Sci & Engn, Jinan 250100, Peoples R China.

IDS 号: AT5ND

在“Web of Science”核心合集中的被引频次: 0

在中的被引频次: 0 (他引0次, 自引0次)

ISSN: 1545-598X

入藏号: WOS:000344988700007

影响因子: 2.228000

中科院一级学科: 工程技术 一级学科分区: 3区; 二级学科: ENGINEERING, ELECTRICAL & ELECTRONIC工程: 电子与电气 二级学科分区: 3区

中科院一级学科: 工程技术 一级学科分区: 3区; 二级学科: GEOCHEMISTRY & GEOPHYSICS地球化学与地球物理 二级学科分区: 4区

中科院一级学科: 工程技术 一级学科分区: 3区; 二级学科: IMAGING SCIENCE & PHOTOGRAPHIC TECHNOLOGY成像科学与照相技术 二级学科分区: 3区

中科院一级学科: 工程技术 一级学科分区: 3区; 二级学科: REMOTE SENSING遥感 二级学科分区: 3区

2

A dielectric logging tool with insulated collar for formation fluid detection around borehole

作者: Wang, B(Wang, Bin);Li, K(Li, Kang);Kong, FM(Kong, Fan-Min);Zhao, J(Zhao, Jia);

来源出版物: JOURNAL OF APPLIED GEOPHYSICS 卷: 119 页码范围: 16-24 出版年:

2015

通讯作者地址: Li, K (reprint author), Shandong Univ, Sch Informat Sci & Engn, 27 Shanda South Road, Jinan 250100, Shandong, Peoples R China.

地址: 1. [Wang, Bin]Shandong Univ, Sch Informat Sci & Engn, Jinan 250100, Shandong, Peoples R China.

2. [Li, Kang]Shandong Univ, Sch Informat Sci & Engn, Jinan 250100, Shandong, Peoples R China.

3. [Kong, Fan-Min]Shandong Univ, Sch Informat Sci & Engn, Jinan 250100, Shandong, Peoples R China.

4. [Zhao, Jia]Shandong Univ, Sch Informat Sci & Engn, Jinan 250100, Shandong, Peoples R China.

IDS 号: CL8LN

在“Web of Science”核心合集中的被引频次: 2

在中的被引频次: 0 (他引0次, 自引0次)

ISSN: 0926-9851

入藏号: WOS:000357226300002

影响因子: 1.355000

中科院一级学科: 地学

一级学科分区: 4区; 二级学科: GEOSCIENCES,

MULTIDISCIPLINARY地球科学综合 二级学科分区: 4区

中科院一级学科: 地学

一级学科分区: 4区; 二级学科: MINING & MINERAL

PROCESSING矿业与矿物加工 二级学科分区: 3区

报告编号: 202000095

报告编号：202000392

论文检索报告

被检索人单位：中国石油大学（华东）

被检索人：王斌

检索数据库：SCIE（SCI）

检索结果： 收录 1 篇。SCIE 中总引 0 次，他
引 0 次。

特此证明，详见附件。

注：

1. 该报告检索论文均由被检索人提交并得到被检索人确认。
2. 不排除姓名相同、姓名拼写相同的情况。

中国石油大学（华东）图书馆

2020 年 3 月 4 日

报告编号：202000392

附件1

1

Study on the Formation and Disassociation Process of Hydrate in Porous Media by Permittivity Dispersion Measurement

作者：Wang, B(Wang, Bin);Zhang, ZH(Zhang, Zhonghao);Xing, LC(Xing, Lanchang);

来源出版物：IEEE ACCESS 卷：7 页码范围：175362-175376 出版年：2019

通讯作者地址：Wang, B (reprint author), China Univ Petr East China, Coll Control Sci & Engn, Qingdao 266580, Peoples R China.

地址：1. [Wang, Bin]China Univ Petr East China, Coll Control Sci & Engn, Qingdao 266580, Peoples R China.

2. [Zhang, Zhonghao]China Univ Petr East China, Coll Control Sci & Engn, Qingdao 266580, Peoples R China.

3. [Xing, Lanchang]China Univ Petr East China, Coll Control Sci & Engn, Qingdao 266580, Peoples R China.

IDS 号：KF7DI

在“Web of Science”核心合集中的被引频次：0

在SCIE中的被引频次：0（他引0次，自引0次）

ISSN：2169-3536

入藏号：WOS:000509399500015

影响因子：4.098000

中科院一级学科：工程技术

一级学科分区：2区；二级学科：COMPUTER SCIENCE, INFORMATION SYSTEMS计算机：信息系统 二级学科分区：2区

中科院一级学科：工程技术 一级学科分区：2区；二级学科：ENGINEERING, ELECTRICAL & ELECTRONIC工程：电子与电气 二级学科分区：3区

中科院一级学科：工程技术 一级学科分区：2区；二级学科：TELECOMMUNICATIONS电信学 二级学科分区：3区

报告编号：202000392

报告编号：202000119

论文检索报告

被检索人单位：中国石油大学（华东）

被检索人：王斌

检索数据库：EI（EI）

检索结果： 收录 1 篇。

特此证明，详见附件。

注：

1. 该报告检索论文均由被检索人提交并得到被检索人确认。
2. 不排除姓名相同、姓名拼写相同的情况。

中国石油大学（华东）图书馆

2020 年 1 月 6 日



报告编号: 202000119

附件1

1

Accession number:20181605018098

Title:Numerical study on complex resistivity measurement of porous media containing gas hydrate

Authors:Wang, Bin ; Xing, Lanchang

Author affiliation:College of Information and Control Engineering, China University of Petroleum (East China), Qingdao, China

Source title:2017 Progress In Electromagnetics Research Symposium - Fall, PIERS - FALL 2017 Volume:2017-November 2017 Pages:993-998

报告编号: 202000119



4.2 论文全文

[1] Wang, Bin, Zhonghao Zhang, and Lanchang Xing. "Study on the Formation and Disassociation Process of Hydrate in Porous Media by Permittivity Dispersion Measurement." *IEEE Access* 7 (2019): 175362-175376. (SCI T2)

IEEE Access
Multidisciplinary | Rapid Review | Open Access Journal

Received November 19, 2019, accepted November 30, 2019, date of publication December 4, 2019,
date of current version December 18, 2019.

Digital Object Identifier 10.1109/ACCESS.2019.2957534

Study on the Formation and Disassociation Process of Hydrate in Porous Media by Permittivity Dispersion Measurement

BIN WANG¹, ZHONGHAO ZHANG¹, AND LANCHANG XING¹, (Member, IEEE)

College of Control Science and Engineering, China University of Petroleum (East China), Qingdao 266580, China

Corresponding author: Bin Wang (wangbin2015@upc.edu.cn)

This work was supported in part by the National Natural Science Foundation of China under Grant 51306212 and Grant 41704124, in part by the Fundamental Research Funds for the Central Universities under Grant 16CX05021A, Grant 18CX02112A, and Grant 18CX02176A, in part by the Shandong Provincial Natural Science Foundation under Grant ZR2019MEE095 and Grant ZR2017BEE026, and in part by the Shandong Province Key Research and Development Plan, under Grant 2018GGX101020.

ABSTRACT To develop a more efficient and environmentally friendly exploitation and production method of gas hydrate, a better understanding of the formation and disassociation process mechanism of gas hydrate in porous media is indispensable. The permittivity spectra of gas hydrate differs from water, oil, ice and gas, and thus measurement of its permittivity properties is a potential approach to detect hydrate existence and content. In this study, THF (tetrahydrofuran) was used as the hydrate former. The permittivity dispersion of hydrate in quartz sand was measured with open-ended coaxial method in the processes of formation and disassociation at a wide radio frequency band from 1MHz to 3GHz. From the dielectric measurements, the hydrate concentration in the porous media was identified with dispersion properties, and the characteristic of the permittivity response upon the hydrate formation and dissociation were also provided. Moreover, by applying dielectric mixing models, the fractions of the solution and hydrate could be estimated. These results implied that the permittivity dispersion could be an effective monitor for the formation and disassociation of the hydrate, and hydrate content could be evaluated in real time with complex permittivity spectra.

INDEX TERMS Complex permittivity, dielectric measurement, dielectric dispersion, gas hydrate, open-end coaxial line, porous media.

I. INTRODUCTION

Clathrate hydrates are crystalline solid compounds consisting of hydrogen-bonded water molecules forming a lattice of polyhedral cages that trap gas molecules [1], [2]. Methane hydrate is abundant in many locations such as sediments and permafrost regions [3]. It was reported that the disassociation of the gas hydrate in reservoir exploitation was caused by depressurization as well as a temperature increase, and hence the dissociation procedure of many kinds of hydrate crystals has been studied and modeled based on data with various experimental methods [4]–[10]. Mechanisms of the formation and dissociation of hydrate crystals in porous media are important to establish efficient techniques for natural gas hydrate exploitation from the sea bottom sediment and tundra in order to avoid geohazards [1], [11], [12]. On the other hand, to develop reliable technology for preventing internal hydrate-plug formation in stored and transported natural gas,

it is meaningful to study the formation process of hydrate crystals [13], [14]. For the formation of gas hydrates in emulsions gives rise to a change in the bulk permittivity, the dielectric spectroscopy obtained with open-end probe was found to be a potential technique for the detection of gas hydrates in emulsified systems [15], [16], e.g. to determine the thickness of the hydrate layer (THF and methane-ethane mixture as the hydrate former) deposited on pipeline walls [17] and to monitor hydrate formation in oil-dominated systems [18]. The influence of pressure on the mechanical and electromagnetic properties of gas hydrate was studied, and it was found that the permittivity is a good indicator of the hydrate phase transition [5], [19]–[24]. The dielectric logging tool working at 1.1GHz was used in a hydrate reservoir of Alaska, and the dielectric logs provided similar trends as other logging method such as sonic and induction, with much finer vertical resolution. Practical logging results demonstrated the usefulness of dielectric logging tools for accurately quantifying in-situ gas hydrate saturation [25], [26]. Permittivity spectra provide valuable information not obtainable from

The associate editor coordinating the review of this manuscript and approving it for publication was Abhishek K. Jha¹.

single-frequency measurements, however, to the best of our knowledge, there is still little study of the permittivity dispersion of the hydrate contained in porous media reported in the literature.

Open-ended coaxial probes have been used to study permittivity dispersion properties of hydrate deposits in Water/Oil emulsions and metal pipe [18]. By measuring a broad frequency range, the hydrate agglomeration and deposition can be detected by permittivity spectra [27]. While THF is a Structure II, not Structure I (like methane), hydrate-former, it offers important advantages for laboratory studies, e.g. stability under more obtainable pressure and temperature, and complete miscibility in water that guarantees good control on the amount of hydrate formed in sediment samples. For THF hydrate obtains analogical electrical and acoustic properties to methane hydrate, THF has been used as the hydrate former to research hydrate's physical properties and interaction with the porous media in many published studies [5]–[7], [28]. In addition, laboratory dielectric spectroscopy measurements of liquids, semisolids and biological materials (e.g. muscles and tubers) in a wide microwave frequency range are presented in recent years, and new measurement methods for determination of complex permittivity have been developed [29]–[33]. Complex permittivity as function of many factors e.g. water content, temperature, salinity and pressure are tending to be studied in broader frequency ranges [34], [35]. The open-ended coaxial probe is very attractive due to its applicability to nondestructive measurements of complex permittivity in a wide microwave frequency range, which can cover the dispersive frequencies of both hydrate and liquid solution simultaneously (1MHz–13.6GHz) [27]. However, concerning the existing studies on dielectric properties of gas hydrate [5]–[7], there was still no research on formation and disassociation process of hydrate in porous media with dielectric spectroscopy.

In this study, permittivity properties of THF hydrate's formation and disassociation processes in both its pure state and quartz sand were studied using open-ended coaxial probes, and an evaluation method based on the permittivity dispersion of the hydrate fraction in porous media was studied. The results demonstrated that dispersion characteristics of complex permittivity spectra on broadband can indicate the existence of the THF hydrate and THF solution together. Furthermore, there are evident differences in the permittivity under 100MHz between the ice and hydrate [36]–[39], which showed that the permittivity dispersion could be used as a potential technique in approaching in-situ hydrate saturation in tundra reservoirs. By applying proper mixing laws, fractions of each component can be precisely evaluated at any period of the experiments.

II. EXPERIMENTAL METHODOLOGY

A. PERMITTIVITY DISPERSION

The permittivity spectrum measuring the dielectric constant and loss factor of materials is always dispersive in the frequency domain, and it is a complex value normally related to

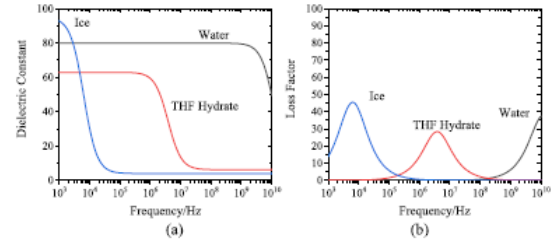


FIGURE 1. Real part (a) and imaginary part (b) of the complex permittivity of ice (blue), the THF hydrate (red), and water (black).

other physical properties [40], defined as:

$$\varepsilon^* = \varepsilon' - j\varepsilon'' \quad (1)$$

where ε^* is the complex relative permittivity, and the real part ε' and imaginary part ε'' refer to the dielectric constant and loss factor, respectively. When an alternating electromagnetic field is applied to the material, several polarization phenomena such as the Maxwell-Wagner effect, displacement of the electronic cloud of atoms, and orientation of polar molecules contribute to the dispersion of the permittivity. The dielectric constant can be interpreted as the net polarization of opposing the applied EM field, and the loss factor is related to the transformation of EM energy to joule heat and polarization loss. Typical complex permittivity spectra of the THF hydrate, ice, and liquid water from 1 kHz to 10 GHz are illustrated in Fig. 1 [41], [42].

The permittivity spectroscopy of THF hydrates, ice, and liquid water can be numerically described as a Cole-Cole model [43].

$$\varepsilon(\omega) = \varepsilon' - j\varepsilon'' = \varepsilon_\infty + \frac{\varepsilon_s - \varepsilon_\infty}{1 + (j\omega\tau)^{1-\alpha}} - j\frac{\sigma}{\omega\varepsilon_0} \quad (2)$$

where $\varepsilon(\omega)$ is the dispersive complex permittivity, ε_s and ε_∞ represent the dielectric constant at static and infinity frequency, respectively, ω is the radian frequency, α is an index parameter less than 1, τ is the relaxation time in sec, and σ is the conductivity

As shown schematically in Fig 1, the prominent dispersion of liquid water's permittivity spectrum caused by the molecular polarization can be observed above 1GHz, while ice and clathrate hydrates are characterized by a wide region of the dielectric dispersion and absorption below 10MHz. For clathrate hydrates, the dispersion depends not only on the relaxation of water but also on the nature of the engaged guest molecules, and may considerably vary with guest molecules [37], [42], [44]. Thus, the hydrate has distinct dispersion characters from both the ice and liquid solution, and consequently, the hydrate formation and disassociation can be monitored by the permittivity spectrum measurement.

B. EXPERIMENT DESIGN

This research was conducted using an instrument as sketched in Fig 2. A plugged glass reactor containing porous media and the THF solution was placed in a program

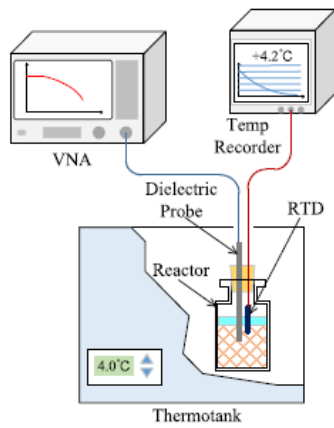


FIGURE 2. Schematics of the experimental equipment. The control accuracy of the thermostat was $\pm 0.5^\circ\text{C}$ and the precision of the temperature recorder with the RTD was $\pm 0.15^\circ\text{C}$. The glass reactor was sealed by a plug preventing volatilization of the solution. The slim-type dielectric probe and the conductor wire for the RTD pierced through the plug to penetrate into the media.

controlled thermostat. To form or dissociate the hydrate, the reactor was cooled to -12°C or warmed to room temperature with an automatic program control. A slim-type open-ended coaxial probe (from Keysight, outer conductor's diameter of 2.2mm, inner conductor's diameter of 0.53mm, insulation layer between the two conductor is Teflon) was connected to a VNA (Vector Network Analyzer from Keysight, model: 5061B) with a 50 Ohm phase-stable cable penetrating into the measured media inside the reactor, and the complex permittivity was acquired with N1500A software installed on the VNA. The measurements were obtained after a calibration by measuring three known reflection coefficients (25°C deionized water, air and a short kit were selected as calibration standards). The dispersive permittivity was recorded every minute in a frequency range from 1MHz to 3GHz with the logarithmic coordinate among the whole experimental procession. A Pt100 resistance temperature detector (RTD) mounted in the reactor was used to monitor the temperature of the media and record the temperature variations in real-time.

The THF (>99.9%) and water were mixed at a mass ratio of 1: 4.25 as a hydrate former ($\sigma = 0.05\text{S/m}$) that did not remain after the hydrate was formed. Six experiments were carried out, and the porous matrix, initial/ target temperature, and solution fraction are summarized in Table 1. Quartz sand with two particle sizes was prepared as the porous media in experiments 3-6, and the THF solution was supersaturated in order to guarantee that no gas was in the pore spaces. The pure THF hydrate formation and dissociation processes were conducted in experiment 1 and 2 without quartz sand, respectively.

The target temperature of the thermostat was set to -12°C in experiments 1, 3, and 4. The motivation for this was to shorten the formation time and increase the conversion rate of the hydrate. During the cooling period, the temperature of the

TABLE 1. Configuration details in the experiments.

Experiment Number	Porous matrix and particle size	Initial temperature / $^\circ\text{C}$	Target temperature / $^\circ\text{C}$	Solution fraction
Experiment 1	None	26	-12	100%
Experiment 2	None	-12	20	100%
Experiment 3	Quartz sand 0.45mm-0.9mm	24	-12	60%
Experiment 4	Quartz sand 0.18mm-0.28mm	25	-12	60%
Experiment 5	Quartz sand 0.45mm-0.9mm	-12	18	60%
Experiment 6	Quartz sand 0.18mm-0.28mm	-12	18	60%

bathing atmosphere inside the tank was always $3-4^\circ\text{C}$ lower than mixture inside the reactor because of the heat capacity lag. These mixtures were cooled to a supercooling condition, and then hydrate nucleation was triggered by the colder dielectric probe (it acted as a heat conductor through the plug, so the temperature of the probe was between the temperature inside and outside the reactor). Formation started with the temperature suddenly jumping to 4.4°C , and was kept for several hours until the temperature gradually dropped to a lower temperature [22]. The dissociation of the hydrates was triggered by setting the target temperature of the thermostat to room temperature in experiment 2, 5 and 6. Experiment 1 and 4 are terminated before reaching the target temperature because the temperature and permittivity indicated that the formation/ dissociation was completed.

III. RESULTS AND DISCUSSION

This section is divided into five parts. First, the dielectric properties of pure THF hydrate will be studied (experiments 1 and 2) in A. Then the effect of the porous media on the hydrate formation and dissociation (experiments 3-6) will be investigated in B and C. The dielectric constant and loss factor at some typical frequency points are illustrated as a function of time, and the effect of the temperature and permittivity on the formation and dissociation processes are concluded. Then, in part D, the volumetric fraction is estimated by the dielectric mixing law, and a fitted spectrum is presented and compared with experimental results. Based on the experimental results, the ambiguity and deviations will be analyzed in last part, E, and furthermore the peculiarity and advantages of permittivity measurements for the hydrate evaluation in the porous media will be stated.

A. DIELECTRIC PROPERTIES OF THE PURE THF HYDRATE

To better study the THF hydrate deposit in porous media, experiment 1 and 2 were conducted to measure the complex

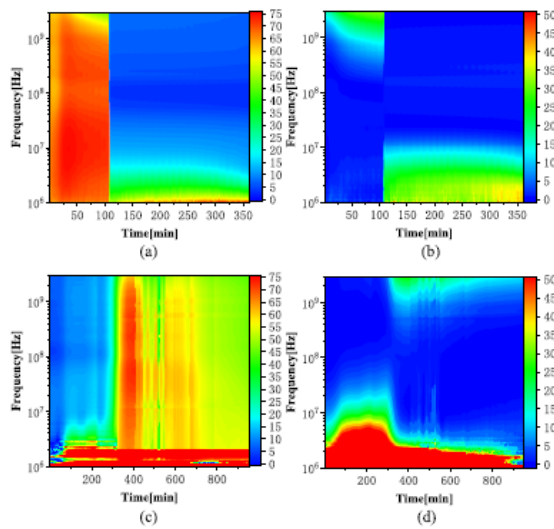


FIGURE 3. Evolution of the complex permittivity spectra as a function of time: (a) effect of the dielectric constant upon the formation process of the pure THF hydrate in experiment 1 (b) effect of the loss factor upon the formation process of the pure THF hydrate in experiment 1 (c) effect of the dielectric constant upon the dissociation process of the pure THF hydrate in experiment 2 (d) effect of the loss factor upon the dissociation process of the pure THF hydrate in experiment 2.

permittivity spectrum during pure THF hydrate formation and dissociation as a control group. Complex permittivity spectra varying with time among the two experiments are illustrated as contour maps in Fig 3.

It can be observed from the contour maps that the characteristic dispersions of the THF solution and THF hydrate were located at a frequency range over 1GHz and below 100MHz, respectively. The dispersion of the liquid solution is mainly due to the molecular polarization of water [46]. It makes the dielectric constant large among the whole spectrum, and the loss factor obtains a resonance peak with its center at dozens of GHz (see the range before the 107th min in experiment 1 and after the 250th min in experiment 2). Orientation of restrained water and THF molecules inside the clathrate hydrate contribute to the dispersion peak below 100MHz, so the spectrum's large amplitude below 100MHz could potentially act as the indicator of the hydrate's appearance (see the range after the 107th min in experiment 1 and before the 250th min in experiment 2). Similar spectroscopy properties e.g. dispersion frequencies and their temperature drift of THF hydrate and THF/water solution have been found in the results of formation experiments of pure THF hydrate layers [27].

To evaluate the experimental process more clearly, the complex permittivity at some frequency points (2.5MHz, 3.5MHz, 10MHz, 300MHz, 1GHz and 3GHz are selected as typical frequencies) are presented with recorded temperature in Fig 4. According to the results of experiment 1, both the dielectric constant and loss factor sharply dropped above 20MHz at the 107th min, while a steep

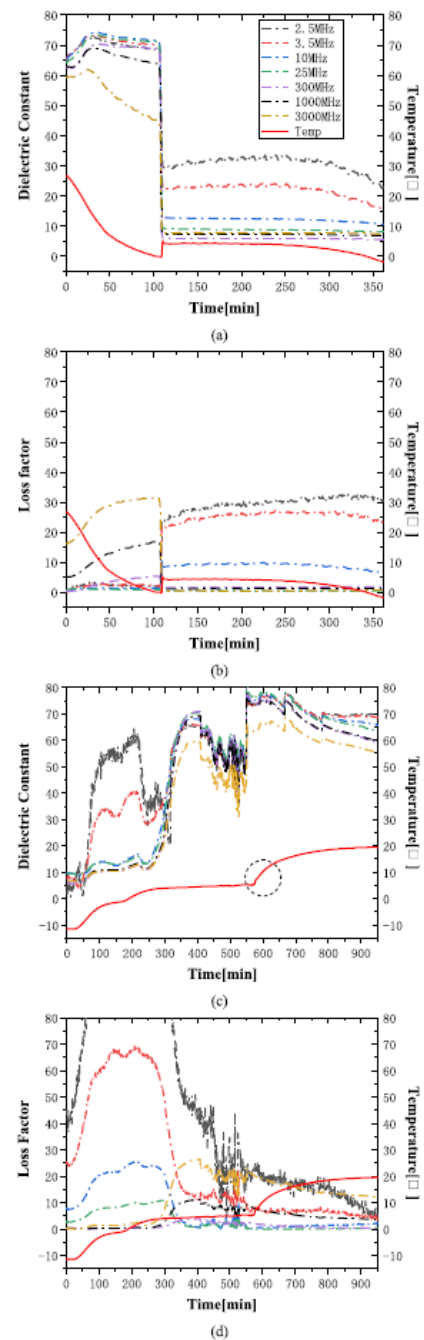


FIGURE 4. Complex permittivity at 2.5MHz, 3.5MHz, 10MHz, 300MHz, 1GHz, and 3GHz and temperature as a function of time. The complex permittivity is plotted with dot dash lines and temperature with solid lines, and the legend that applies to the four subfigures is presented in (a). (a) the effect of the dielectric constant upon the formation process in experiment 1 (b) the effect of the loss factor upon the formation process in experiment 1 (c) the effect of the dielectric constant upon the dissociation process in experiment 2 (d) the effect of the loss factor upon the dissociation process in experiment 2.

temperature rise was observed. For a frequency below 20MHz, peaks appeared with increasing amplitude as the frequency decreased both in the dielectric constant and loss factor. Because the formation of hydrate is exothermic, the temperature jump to 4.4°C vertically at the 107th min indicates that the hydrate has formed in front of the probe's open-end. Compared with the flat and smooth spectrum during the hydrate formation, complex permittivity was observed drastically varying with time during the dissociation process in Fig 3 (c), (d) and Fig 4 (c), (d) before the 550th min.

Considering temperature and complex permittivity synthetically, a stepped change was found at the onset of the formation, while during the dissociation process, the permittivity spectrum fluctuated in a narrow range and the temperature curve was smoother. We drew the conclusion that the dissociation process of the pure THF hydrate is critically slower than its formation, and thus the distribution of the solution and hydrate could be time-varying and more heterogeneous. In addition, as presented in Fig 4(c) and (d), the permittivity's amplitudes were abnormally higher than the THF hydrate's low frequency dispersion at 2.5MHz and 3.5MHz from the 0th min to the 300th min. Random noise was found around the lower limit of the frequency band in both experiment. Later, in the time range from the 400th min to the 570th min, the complex permittivity drastically fluctuated until the temperature broke through the 4.4°C 'platform', which indicates the dissociation process finished. Moreover, it can be observed that both the dielectric constant and loss factor of the THF solution rose as the temperature declined before the 107th min during the formation (experiment 1) and after the 570th min during the dissociation (experiment 2). These phenomena may imply mechanisms of multiphase mixture or the measuring method itself, and will be discussed in the last part of this section.

To show the temperature dependence of hydrate's permittivity, the spectrum of the THF hydrate at 2.9°C and -11.2°C fitted with the Cole-Cole model are presented in Fig 5, meanwhile, complex permittivity of THF solution at 4.4°C is taken as comparison. A steep sloop and a peak were observed in the dielectric constant and loss factor of THF hydrate in low frequency range, respectively, and the resonant frequency drifted to a lower band as the temperature decreased. For temperatures around 0°C, the index parameter α of the Cole-Cole model corresponding to THF hydrate has a relatively small value 0.018 and conductivity $\sigma = 0\text{S/m}$ (both insensitivity to temperature). Early measurement of the structure II hydrates suggested that there is approximately a negative correlation between $(\epsilon_0 - \epsilon_\infty)$ and temperature and the high frequency permittivity ϵ_∞ is relatively a statistical value [42]. According to the complex permittivity obtained within experiment 1 and 2, high frequency permittivity was fitted as $\epsilon_\infty = 7$, and the proper static permittivity ϵ_0 as a function of absolute temperature T (in Kelvin) can be calculated as presented in equation (3) [42]. Referring to the study at lower temperature ranges [45], the relationship between relaxation time τ and the absolute temperature T

TABLE 2. Fitted cole-cole parameters of the three complex permittivity samples.

Samples	ϵ_∞	ϵ_0	τ/sec	$\sigma/\text{S/m}$	α
2.9°C Hydrate	7	61	4.87×10^{-8}	0	0.018
-11.2°C Hydrate	7	63.9	8.6×10^{-8}	0	0.018
4.4°C Soution	5.85	67.8	1.65×10^{-11}	3×10^{-4}	0

were concluded as equation (4).

$$\epsilon_0 - \epsilon_\infty = 14900/T \quad (3)$$

$$\log(\tau) = -11.9 + 1265.7/T \quad (4)$$

The complex permittivity of the THF solution has analogous microwave resonant properties with liquid water and its amplitude depends on volumetric ratio of THF [46], [47]. For THF solution, the Cole-Cole model was transformed to Debye type by setting α to 0. Parameters ϵ_0 , ϵ_∞ and τ fitted from the experimental data matches the results in the early study fundamentally [47]. Table 2 showed the fitted Cole-Cole parameters of the three pairs of complex permittivity in Fig 5.

The fitting method in this section will be used in the calculation of component contents with mixing models in section D and E, and the fitted parameters are selected according to the recorded temperature (invariable parameters like α and σ will not be presented in the tables redundantly).

B. PERMITTIVITY DISPERSION UPON THF HYDRATE FORMATION IN POROUS MEDIA

In experiments 3 and 4, quartz sand with a diameter of 0.45mm-0.9mm and 0.18mm-0.28mm was selected as the porous matrix to study the THF hydrate formation process. Supersaturated THF solution with a 60% volumetric fraction was used as the hydrate former in these experiments. The complex permittivity measured during the formation process within the porous media is illustrated as contour maps in Figs 6 and 7 respectively. Similar to experiment 1, before the onset of the hydrate formation, the permittivity dispersion associated with the liquid THF-water solution was observed in the upper frequency range (especially apparent higher than 1GHz). By marking the abrupt change with dashed lines in the four contour maps, the characteristic of the liquid solution disappeared around the 80th min, which was earlier than in experiment 1. The most striking difference between Figs 6 and 7 appeared in the lower frequency range after the formation: in experiment 4, the slope of the permittivity was about 2 times steeper than that in experiment 3 below 100MHz. However, during the decreasing temperature period, the dispersion peak of the dielectric constant and loss factor drifted to a lower frequency in both experiment. A larger particle size weakens the dispersion peak, and it even seemed that the dispersion disappeared in Fig 6(a). Therefore, from the

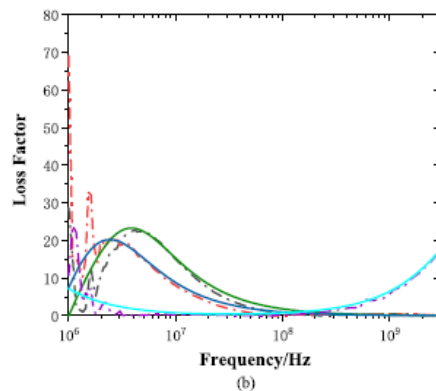
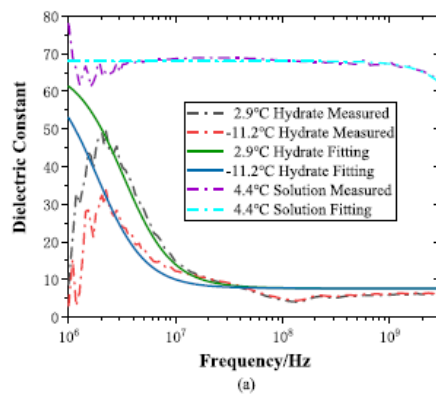


FIGURE 5. Complex permittivity spectra of THF solution and THF hydrate. Solid spectra are measured data, and dot dash spectra are fitted with Cole-Cole model: (a) dielectric constant; (b) loss factor.

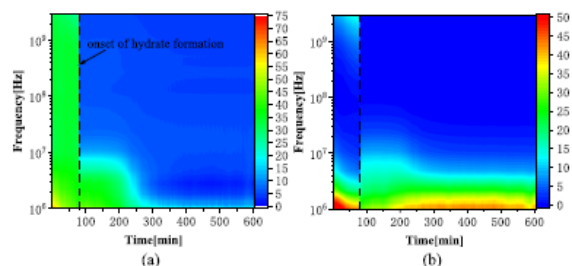


FIGURE 6. Evolution of the complex permittivity spectra as a function of time in experiment 3: (a) effect of the dielectric constant upon the THF hydrate formation process in quartz sand with a particle size of 0.45mm-0.9mm (b) effect of the loss factor upon the THF hydrate formation process in quartz sand with a particle size of 0.45mm-0.9mm.

contour maps, it can be concluded that the addition of porous media accelerates the onset of the formation. Moreover, particle size could influence the dielectric properties during and after the formation.

Four frequencies that were selected to show the permittivity and temperature as a function of time are illustrated in Figs 8 and 9. Accompanying the abrupt permittivity change around the 80th min, the formation process was initiated by a step change of temperature (red solid line) at the same time which was 30 minutes earlier than the process without

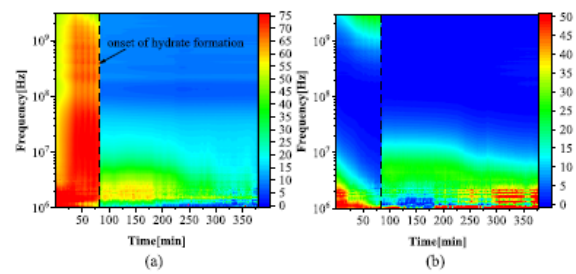


FIGURE 7. Evolution of the complex permittivity spectra as a function of time in experiment 3: (a) effect of the dielectric constant upon the THF hydrate formation process in quartz sand with a particle size of 0.18mm-0.28mm (b) effect of the loss factor upon the THF hydrate formation process in quartz sand with a particle size of 0.18mm-0.28mm.

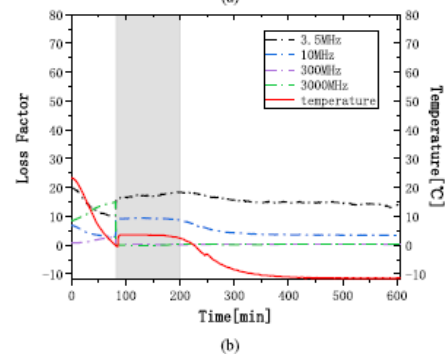
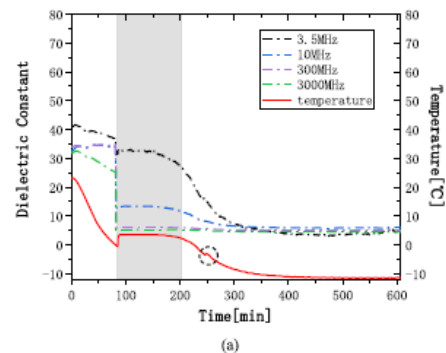


FIGURE 8. Complex permittivity at 3.5MHz, 10MHz, 300MHz, and 3GHz (dot dash line) and measured temperature (solid line) in experiment 3. Quartz sand was selected with a particle size of 0.45mm-0.9mm.

quartz sand (see data of experiment 1 in Fig 4). The dielectric constant and loss factor obtained at the four frequencies in experiments 3 and 4 before the hydrate appeared presented different changing trends. In Fig 8(a), the dielectric constant decreased at 3.5MHz and 3GHz while it remained stable at 10MHz and 300MHz, however, it changed synchronously at all frequencies in Fig 9(a); The loss factor at 3.5MHz and 10MHz decreased with time, and increased at the two higher frequencies in Fig 8(b) and Fig 9(b) in this period. The gray shaded area indicates the phase equilibrium state which signifies the time interval from the onset of the formation to the point where no solution remained inside the reactor. As soon as the formation began, the dielectric constant and loss factor

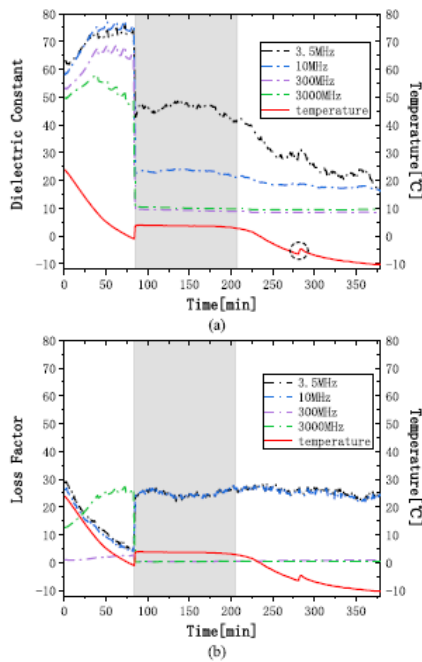


FIGURE 9. Complex permittivity at 3.5MHz, 10MHz, 300MHz, and 3GHz (dot dash line) and measured temperature (solid line) in experiment 4. Quartz sand was selected with a particle size of 0.18mm-0.28mm.

at 300MHz and 3GHz very quickly dropped to 7 and 0, respectively, and then remained steady to the end. The permittivity at 3.5MHz and 10MHz presented hydrate dispersion characteristic peaks which were analogous to experiment 1, while differences can be observed in their amplitude. In the gray shaded zone, the permittivity remained constant as the temperature stayed on the “platform” of phase equilibrium of the hydrate. In addition, in experiments 3 and 4, the time duration of the equilibrium state was fundamentally the same. As all the fluid converted to the hydrate, the permittivity at low frequencies dropped with the temperature. When the target temperature was achieved, all the parameters tended to be stable.

Because the detection depth of the open-ended probe is limited in several millimeters, evolution of the permittivity kept in step with the temperature measured adjacent to the probe end. With molecular polarization of water enhancement at lower temperatures, the permittivity of the THF solution increased at the higher frequency range, and at the same time, the water molecule’s dispersion peak drifted to a lower frequency. Thus, changes of permittivity at 300MHz and 3GHz in Figs 8 and 9, were mainly affected by the temperature sensitivity of liquid water’s dispersion before the hydrate formation started.

To show how permittivity measurements with open-ended probes can be used to monitor the hydrate formation in porous media, 10MHz was used as an example. In experiment 3, the dielectric constant and loss factor jumped to about

13 and 10 at the 80th min (formation began). As the formation continued (gray shaded area), the dielectric constant and loss factor remained unchanged until the formation was completed. Finally, along with the decrease temperature, these two factors kept gradually dropping to about 3 (200th–400th min). Contrastively with the permittivity at 10MHz of experiment 4, the dielectric constant was 23, 22, and 16, and the loss factor was 22, 21, and 19 at the 80th min, the 200th min and the 400th min, respectively. Based on the premise that the THF solution was prepared with the same fraction, and temperature curves showed a fundamentally analogous evaluation trend in the two experiments, only the one curve of the permittivity obtained at 10MHz could indicate differences of the two formation processes. Also, more details such as particle size and regional deposits of hydrate can be revealed from the permittivity spectrum on broad band.

Moreover, after the hydrate formation had finished, a small temperature vibration was marked with a dashed circle at the 250th min in Fig 8 and the 270th min in Fig 9. There was no simultaneous change of permittivity, so this could not be attributed to hydrate agglomerating. Inevitably there is a little water evaporation during the experiment, and as the slight temperature spring-back is located below the freezing point, it is probably due to the condensation of water vapor which is also an exothermic process.

C. PERMITTIVITY DISPERSION UPON THE THF HYDRATE DISSOCIATION IN POROUS MEDIA

In this part, the complex permittivity upon the dissociation of the THF hydrate in porous media was measured in experiments 5 and 6, and presented in Table 1. The solution proportions and porous media were the same as experiments 3 and 4, respectively. As shown in contour maps of Fig 10, with a quartz sand size of 0.45mm-0.9mm, the characteristic of the water solution dominated the permittivity spectrum after the 150th min, the dielectric constant became larger than 30 in the whole frequency range, and the loss factor rose over 1GHz. On the basis of the counter maps, it seems that the dissociation process lasted for merely 25mins in experiment 5 (between the vertical dashed lines and dotted line in Fig 10), which is a bit shorter than the pure THF hydrate, and the onset of melting was about 125mins earlier (see the spectrum in Fig 3, the dissociation began at the 250th min and was completed at the 420th min of experiment 2).

Experiment 6 was performed under the same temperature conditions, and the permittivity obtained with a quartz sand size of 0.18mm-0.28mm is shown in Fig 11. The dielectric constant began to rise at the 200th min (marked with a vertical dashed line) and the loss factor followed the same trend. The hydrate started melting at around the 200th min in experiment 6, which is much later than in experiment 5. However, it was a bit earlier than the pure THF hydrate melting process. Moreover, the loss factor presented in Fig 11(b) signified the dissociation process extremely clearly. The characteristic dispersion of the hydrate in the frequency range below 100MHz

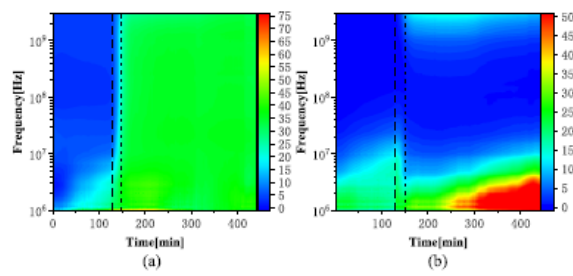


FIGURE 10. Evolution of the complex permittivity spectra as a function of time in experiment 5: (a) effect of the dielectric constant upon the THF hydrate dissociation process in quartz sand with a particle size of 0.45mm-0.9mm (b) effect of the loss factor upon the THF hydrate dissociation process in quartz sand with a particle size of 0.45mm-0.9mm.

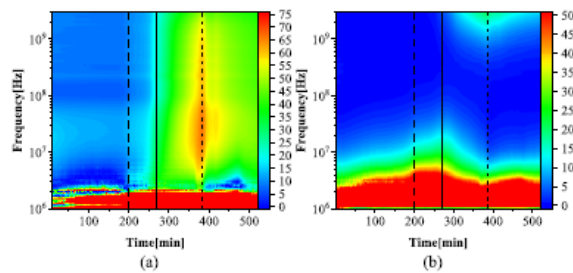


FIGURE 11. Evolution of the complex permittivity spectra as a function of time in experiment 6: (a) effect of the dielectric constant upon the THF hydrate dissociation process in quartz sand with a particle size of 0.18mm-0.28mm (b) effect of the loss factor upon the THF hydrate dissociation process in quartz sand with a particle size of 0.18mm-0.28mm.

gradually drifted to a higher frequency until the 270th min (marked with a vertical solid line), and then it returned to the initial level of the experiment. A slope emerged near to the upper frequency limit after the 240th min, and the strongest amplitude was observed around the 380th min (marked with a vertical dotted line), and coincidentally the low frequency “peak” had its lowest trough and then slightly rose after the 380th min until the end of the experiment.

Taking the temperature into consideration, “peaks” that reemerged after the 150th min and the 380th min in Fig 10(b) and Fig 11(b) were not induced by the polarization of water or THF molecules inside the hydrate. This is because there was no obvious increase in the dielectric constant, and the temperature (see Fig 12 and 13) was higher than the phase equilibrium point after this time. We drew the conclusion that no THF hydrate remained inside the reactor after the 150th min in experiment 5 and the 380th min in experiment 6. In addition, particle size made the dispersion properties different during the whole experiment. The corresponding evolution of the permittivity at typical frequencies is illustrated with temperature in Figs 12 and 13.

In order to prepare the dissociation experiments, the thermostatic tank was cooled to -12°C to make sure all the solution was completely consumed. After several hours' temperature maintenance to prevent uncontrolled hydrate melting occurring, the target temperature was set to 18°C ,

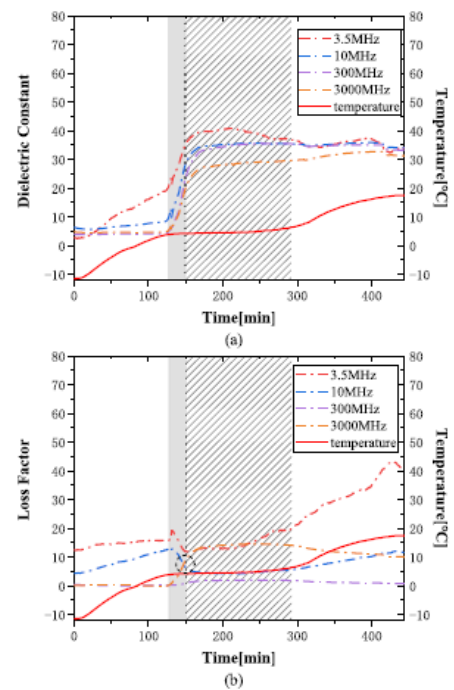


FIGURE 12. Complex permittivity at 3.5MHz, 10MHz, 300MHz, and 3GHz (dot dash line) and measured temperature (solid line) in experiment 5. Quartz sand was selected with a particle size of 0.45mm-0.9mm.

and the dissociation experiment began. During this procedure, a stepped temperature increase can be clearly observed in Figs 12 and 13. Initially, the temperature rose to 4.4°C at the 125th min and the 210th min in experiments 5 and 6, respectively, and then the temperature was held at 4.4°C for about 145min and 160min, respectively, which was much shorter than the dissociation process of the pure THF (320min, see Fig 4 (c) and (d)). Reviewing the result of experiment 2, the temperature broke through the 4.4°C platform with a steep rising edge at 570min (marked with a dashed circle in Fig 4), which was different from experiments 5 and 6 (the temperature more gently rose after the hydrate dissociation). Concerning the permittivity in Figs 12 and 13, more details of the phase transformation during the hydrate dissociation surrounding the probes' open-end are illustrated more definitely. Rising slopes were observed in all dielectric constant curves within the phase equilibrium platform (125min-150min in Fig 12(a) and 240min-380min in Fig 13(a)), while simultaneously the loss factor of 3.5MHz and 10MHz fell to the lowest value in the whole range at the end of the gray shaded zone in Figs 12(b) and 13(b); Moreover, there was an intersection point of the loss factor at 10MHz and 300MHz located around 145/320 min in experiments 5 and 6, which is marked with a dashed circle in Figs 12(b) and 13 (b). The permittivity change coincided with the phase equilibrium temperature in experiment 6. On the contrary, another interesting feature in the permittivity/ temperature plot was found in experiment 5 in which the permittivity slopes did not

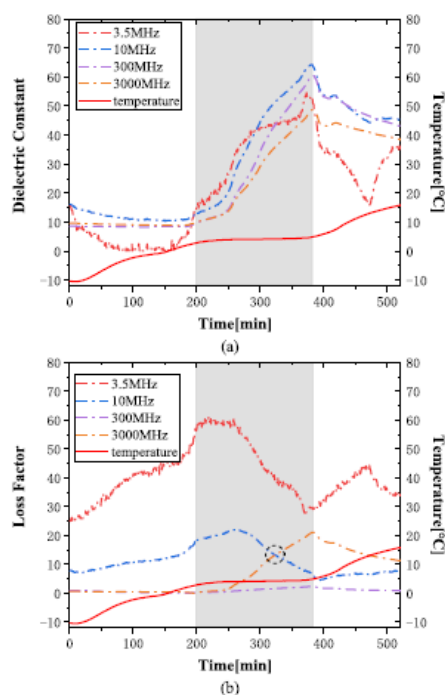


FIGURE 13. Complex permittivity at 3.5MHz, 10MHz, 300MHz, and 3GHz (dot dash line) and measured temperature (solid line) in experiment 6. Quartz sand was selected with a particle size of 0.18mm-0.28mm.

match the temperature evaluation, and as presented in Fig 12, the duration time of the phase equilibrium temperature far exceeded the permittivity change period. This indicated the hydrate melting near the probe (excess part is marked as striped shaded area in Fig 12). A similar discrepancy was also found in Fig 4, where the slopes of the permittivity occurred at the incipient stage of the phase equilibrium platform both for the pure THF hydrate and with 0.45-0.9mm quartz sand.

In this study, the permittivity information only represents the phase transition several millimeters around the probe's terminal, and hydrate melting speed detected in this small area may be significantly different from the rest of the space inside the reactor. Nevertheless, according to the equilibrium temperature duration, the total dissociation time in the two experiment was almost the same (145mins in experiment 5 and 160mins in experiment 6, only a 15mins difference). As the striped shaded area shows in Fig 12, the permittivity at all four frequencies tended to be stable following the previous gray shaded area at the phase equilibrium temperature of about 4.4°C.

D. QUANTITATIVE ESTIMATION OF THE HYDRATE PROPORTION

Estimation of the component content from the permittivity data can be robust when a proper mixing model is available [5], [7], [16], [43], [48]–[50]. In this study, CRIM (Complex Refractive Index Method) – a volume type mixing law that was feasible in previous researches on the hydrate

fraction was selected to fit the measured permittivity [7].

$$\sqrt{\epsilon_m^*} = A\sqrt{\epsilon_{sand}^*} + B\sqrt{\epsilon_{solution}^*} + C\sqrt{\epsilon_{hydrate}^*} \quad (5)$$

where ϵ_m^* is the whole mixture's complex permittivity, and ϵ_{sand}^* , $\epsilon_{solution}^*$, and $\epsilon_{hydrate}^*$ are the complex permittivity of pure quartz sand, the THF solution, and the THF hydrate, respectively. Parameters A , B , and C are the volume fractions of pure quartz sand, the THF solution, and the THF hydrate, respectively [51]. Furthermore, under the assumption that the pore space within the matrix must be filled either with liquid or hydrate, the sum of A , B , and C should always be 100%. Quartz sand has a dielectric constant of 3.8 and a negligibly low loss factor both of which are insensitive to temperature and frequency [52]. The $\epsilon_{solution}^*$ and $\epsilon_{hydrate}^*$ can be calculated with the Cole-Cole model, and corresponding parameters as function of temperature were discussed above. In the following calculation, $\epsilon_{solution}^*$ and $\epsilon_{hydrate}^*$ were selected corresponding to temperatures from results of section 3.1. The permittivity at four time nodes are presented in Fig 14 for experiments 3 and 4. Considering that the majority of the hydrate formation took a very short time as shown in section 3.2, only the complex permittivity before and after the complete hydrate formation are presented. As shown in Fig 14 (a) and (b), the four spectra correspond to the complex permittivity at the 14th min (black dot dash line) and 46th min (red dot dash line) before hydrate formation, and the 228th min (blue dot dash line) and the 305th min (green dot dash line) after the hydrate formation of experiment 3, and the four measured spectra at the 13th min (black dot dash line) and the 45th min (red dot dash line) before the hydrate formation, and the 240th min (blue dot dash line) the 275th min (green dot dash line) after the hydrate formation of experiment 4. The measured curve became increasingly noisy with decreasing frequency, because of the sensitivity of the reflection index used for the permittivity reversion. Equation 5 was used for the hydrate fraction estimation, and the fitted permittivity is illustrated as a solid line in Fig 14.

In the permittivity spectra obtained before the hydrate formation, two dielectric dispersions occurred. The dispersion over 1GHz was due to the molecular polarization of water, and the interfacial polarization resulted in the dispersion peak below 100MHz. After the hydrate formation, only the dielectric dispersion of the THF hydrate was observed. Furthermore, as revealed from Fig 14, the dispersion properties of both the liquid solution and hydrates varied with the temperature. The THF dispersion frequency drifted to a lower band as the temperature decreased (see the 228th and 305th min in Fig 14(a) and (b), and the 240th and 275th min in Fig 14(c) and (d)). The water dispersion also moved to a lower frequency, and a slight decline was observed in the dielectric constant as the temperature decreased before the hydrate formation (see the 14th and 46th min in Fig 14(a) and (b), and the 13th and 45th min in Fig 14(c) and (d)). These variation tendencies quantitatively matched experimental results

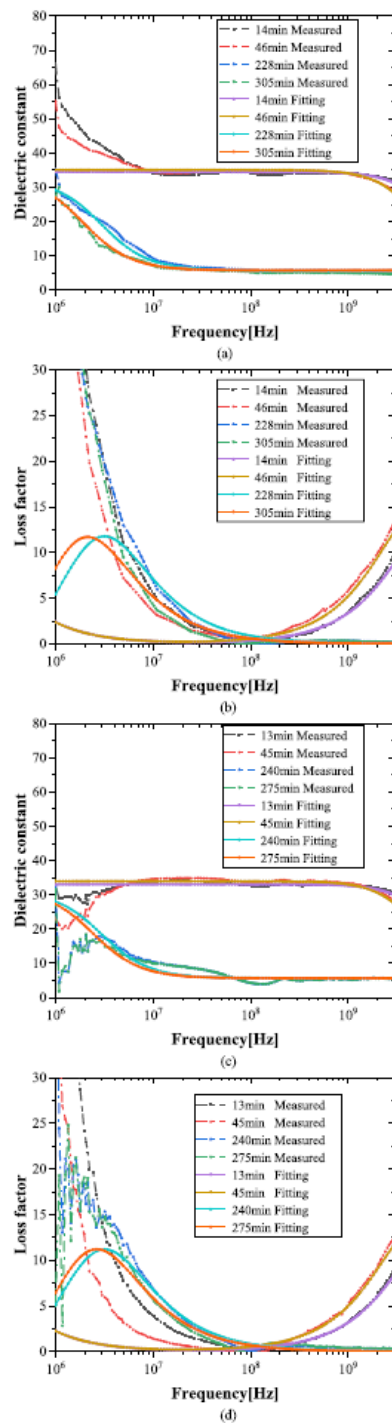


FIGURE 14. The dash dot spectra are the complex permittivity obtained with open-ended probes during experiments 3 and 4. The solid spectra were fitted to the permittivity with Cole-Cole and CRIM models. (a) The dielectric constant with a quartz sand particle size of 0.45mm-0.9mm (b) The loss factor with a quartz sand particle size of 0.45mm-0.9mm (c) The dielectric constant with a quartz sand particle size of 0.18mm-0.28mm (d) The loss factor with a quartz sand particle size of 0.18mm-0.28mm.

in previous studies, and the precise volumetric content can be determined with further calculation.

By assuming that the THF solution and the THF hydrate are dispersed in a continuous phase inside pores of the matrix (quartz sand of two particle sizes), the volumetric fraction of the THF hydrate, solution and quartz sand can be estimated using equation 5. Correspondingly, Table 3 presents the parameters A, B, and C, and the fitted data of the CRIM and Cole-Cole model were used to obtain the solid spectra in Fig 14. The Cole-Cole parameters depended on temperature, and extraordinarily, parameters of hydrate were calculated with equation 3 and 4 which were derived from the measured data. The estimated solution fractions before hydrate formation had a slight deviation from the average level – 60% given in Table 1, and this deviation was larger in experiment 3 than in experiment 4. Furthermore, a similar phenomenon was also observed after the hydrate formation in the two experiments. Additionally, parameter A slightly decreased after the formation process was completed, for instance, the estimated volumetric fraction of quartz sand changed from 38% at the 46th min to 37.1% at the 228th min in experiment 3.

Since the time duration of the hydrate melting process was much longer than the agglomeration, more details of component change were obtained with the fitting method mentioned above. To determine the phase transition during the dissociation process, the permittivity at six time nodes (two more extra time nodes during the dissociation process were added, the 141th and the 153th min in experiment 5 and the 309th and the 336th min in experiment 6) which are presented in Fig 15 with the corresponding temperatures. The fitted parameters are presented in Table 3. Similar to the quantitative analysis on previous formation experiments, the volumetric fraction of each component was estimated from the measured complex permittivity with the CRIM model. At the beginning, the dispersion peak of the hydrate moved to a higher band as the temperature rose (see the 18th min and the 56th min of experiment 5, and the 22th min and the 130th min of experiment 6), and it was reversed when the temperature fell after the hydrate formation in Fig 14. In Fig 15 (a) and (c), the light blue and brown solid spectra were fitted before the onset of hydrate dissociation, and the dielectric constant over 100MHz was nearly flat without any perceived polarization, and hence no liquid solution is assumed to spread around the probe at this stage. Afterwards, once the temperature reached the THF hydrate's phase equilibrium state, the solid hydrate began to gradually melt. The variation of the whole measured permittivity is illustrated in Figs 12 and 13, as the temperature rose the dielectric constant increased over 100MHz, while at the same time, the amplitude of the THF hydrate's dispersion among the lower band was gradually reduced until it disappeared. Also, components fraction changes during hydrate melting were revealed by analyzing the fitted permittivity spectrum from a single measurement relying on special time nodes. It can be found in Fig 15 that the water's dispersion characteristic first began to emerge in the olive green solid spectrum over 1GHz,

TABLE 3. Parameters fitted to equation (5) during the formation process.

Experiment Number	Sand Particle Size	Temperature /°C	Time /min	A	B	C	ϵ_{H0}	ϵ_{H0}	τ_H/sec	ϵ_{S0}	ϵ_{S0}	τ_S/sec
Experiment 3	0.45-0.9mm	19.2	14	37.9%	0%	62.1%	None	None	None	5.85	66.67	1.15 e-11
Experiment 3	0.45-0.9mm	6.6	46	38%	0%	62%	None	None	None	5.85	67.63	1.58 e-11
Experiment 3	0.45-0.9mm	-1.1	228	37.1%	62.9%	0%	7	61.8	5.69 e-8	None	None	None
Experiment 3	0.45-0.9mm	-9	305	37.2%	62.8%	0%	7	63.44	7.84 e-8	None	None	None
Experiment 4	0.18-0.28mm	19	13	39.9%	0%	60.1%	None	None	None	5.85	66.68	1.15 e-11
Experiment 4	0.18-0.28mm	6.6	45	39.7%	0%	60.3%	None	None	None	5.85	67.63	1.58 e-11
Experiment 4	0.18-0.28mm	-1.1	240	39.1%	60.9%	0%	7	61.8	5.69 e-8	None	None	None
Experiment 4	0.18-0.28mm	-6	275	39.1%	60.9%	0%	7	62.81	6.91 e-8	None	None	None

which was obtained during the initial stage of the dissociation process. Then as the hydrate melted, the dielectric constant continued to rise in the high frequency range. The orange solid spectrum was fitted from the data obtained at a later stage of the dissociation, and the water's dispersion became more conspicuous than in the olive green spectrum. The dark blue solid spectrum had the largest numerical value of the permittivity in the high frequency range and the most prominent dispersion of water corresponded to the state where no hydrate remained. The flat dielectric constant curves at a lower frequency and at temperatures higher than 4.4°C indicated that no hydrate deposit remained inside the reactor.

More details on the experimental process were revealed from the fitted parameters of CRIM. As shown in Table 4, a larger sand particle size caused parameter A to be a bit smaller corresponding to same stages in the two experiments. Before the onset of the dissociation, the hydrate fraction slightly rose with increasing temperature in both experiments. For the phase equilibrium period, first, the estimated quartz sand fraction drastically declined (from 36.9% to 22% in experiment 5 and from 39.1% to 26.5% in experiment 6), and then slightly increased, while the hydrate stock continued to be reduced and the solution accumulated during the whole equilibrium period. After the dissociation was completed, parameter A recovered to the level before hydrate start melting, and was even a little larger than this level. As the results showed in the previous sections, the dissociation was a relatively time-consuming process with the temperature condition stable at 4.4 °C, so the components that changed during the dissociation process cannot be estimated by only with the recorded temperature.

As discussed above, by applying the Cole-Cole and CRIM models to the permittivity, an estimation of each component's proportion can be achieved. Although there was a small deviation below 100MHz, the fitted spectra were fundamentally consistent with the experimental data. Taking the recorded temperature into consideration, a detailed analysis was made

on the evolution process of the apparent hydrate's formation and dissociation.

E. ANALYSIS AND DISCUSSION

1) ERROR ANALYSIS

From results in Table 3 and 4, it can be found that the discrepancy between the estimated fractions varied among the whole experimentation process, and the relative deviation of parameter A (calculated by taking the prepared volumetric fraction of quartz sand 40% as standard) is smaller than 7.75% except during the phase equilibrium period in experiment 5 and 6. Inhomogeneous distribution of the measured media likely results in the nonzero deviation of the estimated volumetric fractions. Moreover, the abnormally big discrepancy could be found in parameter A during the dissociation period in experiment 5 and 6 (e.g. relative deviation of parameter A at 141th min in experiment 5 reaches 45%), because the fluid stream generated by the hydrate melting disrupt the distribution of the fluid and solid seriously. Until no hydrate left, distribution tended to be more stable and homogeneous, and the volumetric fractions estimated with CRIM came back to the values around the standard level (e.g. the relative deviation of parameter A decreased to 0.25% at 504th min in experiment 6).

For all the measured data exhibited above, errors were found in the spectrum below 10MHz, which was due to the increasing uncertainty around the lower frequency limit of the open-ended coaxial method [27]. The uncertainty at low frequencies is mainly attributed to the low sensitivity in the reflection coefficient for permittivity changes at the open-end of the probe. Also, in the frequency range below 100MHz, dispersive peaks with amplitudes that are bigger than the hydrates' were observed in the period before the onset of the formation or after the dissociation was completed. As these periods were all out of the platform of the phase equilibrium state, it can be affirmed that the dispersive peaks must be related to factors other than the hydrate's dispersion.

TABLE 4. Parameters fitted to equation (5) during the dissociation process.

Experiment Number	Sand Particle Size	Temperature /°C	Time /min	A	B	C	ϵ_{H0}	ϵ_{H0}	τ_H /sec	ϵ_{S0}	ϵ_{S0}	τ_S /sec
Experiment 5	0.45-0.9mm	-10	18	37.1%	62.9%	0%	7	63.65	8.18×10^{-8}	None	None	None
Experiment 5	0.45-0.9mm	-3	56	36.9%	63.1%	0%	7	62.18	6.13×10^{-8}	None	None	None
Experiment 5	0.45-0.9mm	4.2	141	22%	53.1%	24.9%	7	60.75	4.63×10^{-8}	5.85	67.8	1.65×10^{-11}
Experiment 5	0.45-0.9mm	4.3	153	27%	22.4%	50.6%	7	60.73	4.62×10^{-8}	5.85	67.8	1.65×10^{-11}
Experiment 5	0.45-0.9mm	6.6	297	37.1%	0%	62.9%	None	None	None	5.85	67.63	1.58×10^{-11}
Experiment 5	0.45-0.9mm	17.3	427	37.9%	0%	62.4%	None	None	None	5.85	66.81	1.22×10^{-11}
Experiment 6	0.18-0.28mm	-10	22	39.3%	60.7%	0%	7	63.65	8.18×10^{-8}	None	None	None
Experiment 6	0.18-0.28mm	-1.1	130	39.1%	60.9%	0%	7	61.8	5.69×10^{-8}	None	None	None
Experiment 6	0.18-0.28mm	4.3	309	26.5%	24.4%	49.1%	7	60.73	4.62×10^{-8}	5.85	67.8	1.65×10^{-11}
Experiment 6	0.18-0.28mm	4.4	336	28.7%	16.7%	54.6%	7	60.71	4.6×10^{-8}	5.85	67.8	1.65×10^{-11}
Experiment 6	0.18-0.28mm	13	472	39.8%	0%	60.2%	None	None	None	5.85	67.1	1.39×10^{-11}
Experiment 6	0.18-0.28mm	15	504	39.9%	0%	60.1%	None	None	None	5.85	67	1.31×10^{-11}

The Maxwell-Wagner effect could be the most probable factor [53], [54]. Although the prepared quartz sand was well elutriated, dissolved mineral ions could increase the conductivity of the solution. On the contrary, the Maxwell-Wagner effect occurs in heterogeneous systems, however no quartz sand was installed in experiments 1 and 2, so dispersion peaks caused by interfacial polarization were not found in Figs 3 and 4.

It must be clarified that in the contour maps of Fig 3, the large amplitude below 2MHz may be due to systematic error and not the interfacial polarization. Moreover, from results in experiments 3-6 with two particle sizes, the characters of interfacial polarization varied with particle size. The experimental data and calculated spectra are presented together in Figs 14 and 15, and the fitted results almost matched the practical curves over the whole band. However, in the same time period mentioned above, serious inconformity was still found between the fitted solid spectra and measured permittivity at the lower band, and in fact, as shown in Figs 14 and 15, low frequency dispersion peaks obtained from experiments were far larger than the fitted ones. Considering the inherent inaccuracy of the open-end coaxial method around the lower frequency limit, it is assumed that there are another two factors causing these deviation: first, the scouring effect accompanying the hydrate dissociation process causes more ions to be dissolved, this discrepancy in Fig 15 is larger than in Fig 14. Second, the CRIM model is based on the weighted volumetric sum of each component's complex refractive index, so it cannot describe the interfacial dispersion caused by fundamental ion transport. To take the Maxwell-Wagner effect into account, Hanai's generalization

of Bruggeman's equation [55] for two-phase mixture is used to fit the permittivity measured before the hydrate formation onset and after dissociation completed as control group (13th min in experiment 3 and 297th min in experiment 5). In this model, the volume fraction ϕ , of the dispersed phase is given as:

$$\phi = 1 - \frac{\epsilon_{\text{disp}}^* - \epsilon_m^*}{\epsilon_{\text{disp}}^* - \epsilon_{\text{cont}}^*} \left(\frac{\epsilon_{\text{cont}}^*}{\epsilon_m^*} \right)^{1/3} \quad (6)$$

where ϵ_{cont}^* is the complex permittivity of the continuous phase, ϵ_{disp}^* is the complex permittivity of the dispersed phase, and ϵ_m^* is the effective complex permittivity of the mixture. As shown in Fig 16, when THF solution and quartz sand acted as continuous phase and dispersed phase respectively, curves fitted with Hanai's formula matched the experimental data much better than with CRIM in frequency range below 100MHz. Therefore, it can be assumed that the Maxwell-Wagner effect is the likely explanation to the dispersive peaks at lower frequencies without hydrate existence. Nevertheless, in consideration of the matching effect at the whole band, a big deviation was found between the fitted parameters of Hanai's formula in Fig 16 (volume fraction of THF solution is 75.5%, and volume fraction of quartz sand is 24.5% at both 13th min and 297th min) and the reference values given in Table 1. As the interfacial polarization was not the emphasis of this study, more suitable fitting models on porous media containing hydrates will be studied and developed in our following work.

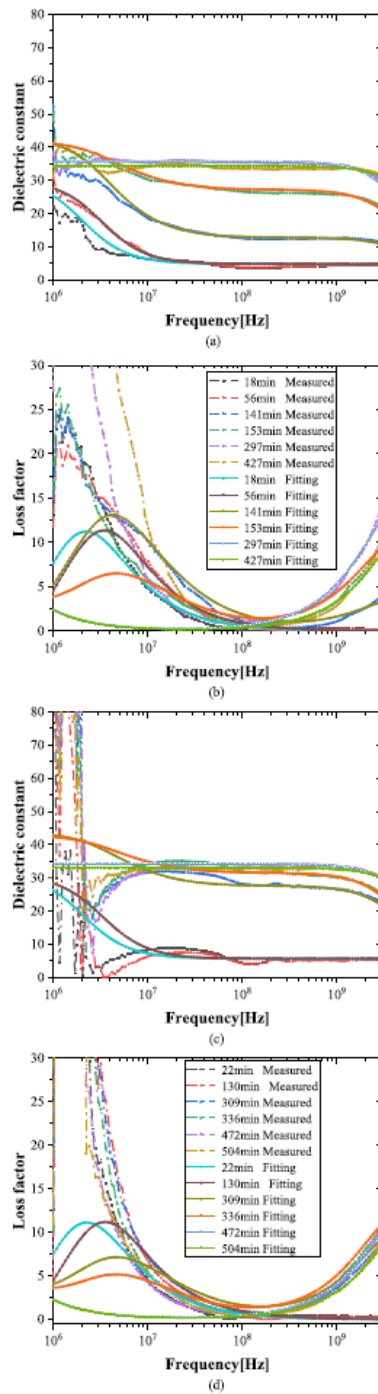


FIGURE 15. The dash dot spectra are the complex permittivity obtained with open-ended probes during experiments 5 and 6. The solid spectra were fitted to measure the permittivity with the Cole-Cole and CRIM models. (a) The dielectric constant with a quartz sand particle size of 0.45mm-0.9mm (b) The loss factor with a quartz sand particle size of 0.45mm-0.9mm (c) The dielectric constant with a quartz sand particle size of 0.18mm-0.28mm (d) The loss factor with a quartz sand particle size of 0.18mm-0.28mm.

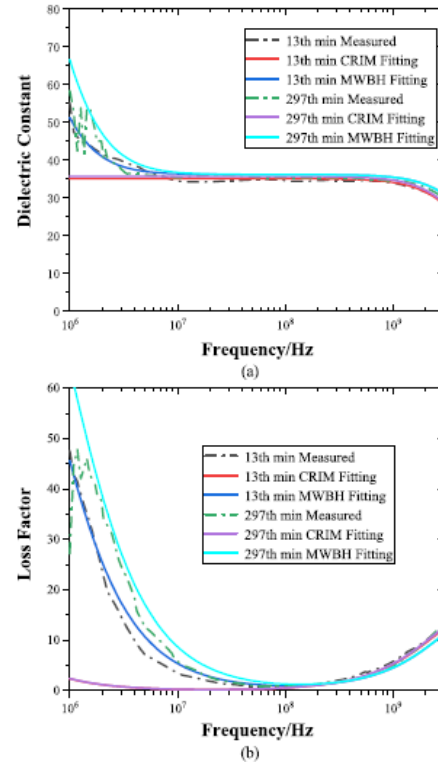


FIGURE 16. The dash dot spectra are the complex permittivity obtained with open-ended probes before formation onset and after dissociation completed in experiments 3 and 5. The solid spectra were fitted to measure the permittivity with the Hanai-Bruggeman and CRIM models. (a) The dielectric constant (b) The loss factor.

2) THE ADVANTAGES OF THE PERMITTIVITY DISPERSION MEASUREMENT

Both the temperature and permittivity can be strict indicators of the hydrate formation and dissociation [1], [7], but these two parameters did not always synchronize in this study. The most conspicuous is that during the dissociation process of the pure THF hydrate and with quartz sand of 0.45mm-0.9mm, the increasing slope of the dielectric constant indicated the accumulation of the liquid solution at the initial segment of the “phase-equilibrium platform”, and the same for time-varying curves of the loss factor. The stable state of the equilibrium temperature was verified to indicate that phase transformation was underway in the whole space of the vessel. In other word, the phase transformation continues until the equilibrium platform breaks up. In contrast, the detection range of the open-end coaxial probe, which was stated above, approximately equals the diameter of the coaxial line, and thus the complex permittivity in only several millimeters around the probe could be precisely recorded. As a result, the deposit information of the hydrate at a particular point inside the porous media can be revealed from the dispersion properties of the complex permittivity measured with the open-end coaxial method. Practically, considering

the inhomogeneous media inside the reactor and gradient temperature on its boundary, it is possible that phase transformation process varies with position inside the reactor. Taking the results of Fig 12 as an example, the phase transformation among the permittivity measurement range was completed in the gray shaded area, and permittivity remained almost stable in the strip shaded area. As mentioned in 3.1, the permittivity of both the hydrate and the solution depends on temperature, and thus without phase transformation there would not be obvious changes in the permittivity unless the temperature changes. We can draw the conclusion that for an estimation of the hydrate in porous media at a particular point, the equilibrium temperature is necessary for phase transformation of the hydrate but it is not sufficient, while from previous analysis, the complex permittivity is definitely a coincidental indicator of the hydrate formation and dissociation.

IV. CONCLUSION

In order to develop a method to evaluate the hydrate content in porous media, the THF hydrate's formation and dissociation processes in quartz sand were monitored using permittivity measurements with the open-ended coaxial method. First, the permittivity of the pure THF hydrate was recorded as the control group, and the complex permittivity of the pure THF solution and the THF hydrate at different temperatures were tested with the Cole-Cole model and corresponding parameters varying with temperature were also calculated. Then the temperature and the complex permittivity were studied during the hydrate agglomeration and melting in quartz sand with different particle sizes. Compared with the temperature, more details were revealed both by analyzing how the permittivity varies as a function of time, and from a single permittivity spectrum at some specified time node. Results showed that the characteristic dispersion peak could be used to determine the accumulation of the hydrate, and a rising of the permittivity at low frequency indicated the formation of the hydrate, while decline at high frequency indicated a consumption of the solution liquid, and vice versa. Finally, by applying CRIM to fit the experimental data, the volumetric fraction of each component was quantitatively estimated. In conclusion, a method to monitor the existence of hydrate and evaluate its content in porous media is established with the measurement of permittivity dispersion in this study. Analysis of results presented here showed significant potential of the permittivity and its dispersion for evaluating of hydrate deposits in a porous matrix. To accurately estimate the proportion of each component in real time, further investigation still need to be carried out, and more appropriate mixing models will be established in the next research.

ACKNOWLEDGMENT

Thanks to Dr. E. C. Mignot, Shandong University, for linguistic advice.

REFERENCES

- [1] E. D. Sloan, Jr., and C. A. Koh, *Clathrate Hydrates of Natural Gases*. Boca Raton, FL, USA: CRC Press, 2007.
- [2] P. Englezos, "Clathrate hydrates," *Ind. Eng. Chem. Res.*, vol. 32, no. 7, pp. 1251–1274, 1993.
- [3] A. V. Milkov, "Global estimates of hydrate-bound gas in marine sediments: How much is really out there?" *Earth-Sci. Rev.*, vol. 66, no. 3, pp. 183–197, 2004.
- [4] M. Helgerud, J. Dvorkin, A. Nur, A. Sakai, and T. Collett, "Elastic-wave velocity in marine sediments with gas hydrates: Effective medium modeling," *Geophys. Res. Lett.*, vol. 26, no. 13, pp. 2021–2024, 1999.
- [5] J. Y. Lee, J. C. Santamarina, and C. Ruppel, "Mechanical and electromagnetic properties of northern Gulf of Mexico sediments with and without THF hydrates," *Mar. Petroleum Geol.*, vol. 25, no. 9, pp. 884–895, 2008.
- [6] J. Y. Lee, T. S. Yun, J. C. Santamarina, and C. Ruppel, "Observations related to tetrahydrofuran and methane hydrates for laboratory studies of hydrate-bearing sediments," *Geochem. Geophys. Geosyst.*, vol. 8, no. 6, 2007, Art. no. Q06003.
- [7] J. Lee, J. C. Santamarina, and C. Ruppel, "Parametric study of the physical properties of hydrate-bearing sand, silt, and clay sediments: 1. Electromagnetic properties," *J. Geophys. Res., Solid Earth*, vol. 115, no. B11, 2010, Art. no. B11104.
- [8] N. Kumar, N. B. Chowdhury, and J. G. Beltran, "A 3-in-1 approach to evaluate gas hydrate inhibitors," *Energies*, vol. 12, no. 15, p. 2921, 2019.
- [9] S. Almenningen, P. Fotland, and G. Ersland, "Magnetic resonance imaging of methane hydrate formation and dissociation in sandstone with dual water saturation," *Energies*, vol. 12, no. 17, p. 3231, 2019.
- [10] K. Xue, L. Yang, J. Zhao, Y. Li, Y. Song, and S. Yao, "The study of flow characteristics during the decomposition process in hydrate-bearing porous media using magnetic resonance imaging," *Energies*, vol. 12, no. 9, p. 1736, 2019.
- [11] Y. Song, L. Yang, J. Zhao, W. Liu, M. Yang, Y. Li, Y. Liu, and Q. Li, "The status of natural gas hydrate research in China: A review," *Renew. Sustain. Energy Rev.*, vol. 31, no. 2, pp. 778–791, 2014.
- [12] S. Pinkert, "Dilation behavior of gas-saturated methane-hydrate bearing sand," *Energies*, vol. 12, no. 15, p. 2937, 2019.
- [13] K. Folgerø, K. Haukalid, J. Kocbach, and A. S. Peterson, "Combined thickness and permittivity measurement of thin layers with open-ended coaxial probes," *Sensors*, vol. 19, no. 8, p. 1765, 2019.
- [14] J. Chen, K.-L. Yan, G.-J. Chen, C.-Y. Sun, B. Liu, N. Ren, D.-J. Shen, M. Niu, Y.-N. Lv, N. Li, and A. K. Sum, "Insights into the formation mechanism of hydrate plugging in pipelines," *Chem. Eng. Sci.*, vol. 122, pp. 284–290, Jan. 2015.
- [15] T. Jakobsen, J. Sjöblom, and P. Ruoff, "Kinetics of gas hydrate formation in w/o-emulsions the model system trichlorofluoromethane/water/non-ionic surfactant studied by means of dielectric spectroscopy," *Colloids Surf. A, Physicochem. Eng. Aspects*, vol. 112, no. 1, pp. 73–84, 1996.
- [16] T. Jakobsen and K. Folgerø, "Dielectric measurements of gas hydrate formation in water-in-oil emulsions using open-ended coaxial probes," *Meas. Sci. Technol.*, vol. 8, no. 9, p. 1006, 1997.
- [17] J. H. Sa, B. R. Lee, X. Zhang, K. Folgerø, K. Haukalid, J. Kocbach, K. J. Kinnari, X. Li, K. Askvik, and A. K. Sum, "Hydrate management in deadlegs: Detection of hydrate deposition using permittivity probe," *Energy Fuel*, vol. 32, no. 2, pp. 1693–1702, 2018.
- [18] K. Haukalid, K. Folgerø, T. Barth, and S. L. Fjermestad, "Hydrate formation in water-in-crude oil emulsions studied by broad-band permittivity measurements," *Energy Fuel*, vol. 31, no. 4, pp. 3793–3803, 2017.
- [19] H. Masayuki, N. Yukio, Y. Norimasa, and E. Toshiro, "Basic research on the mechanical behavior of methane hydrate-sediments mixture," *Soils Found.*, vol. 45, no. 1, pp. 75–85, 2005.
- [20] A. Masui, K. Miyazaki, H. Haneda, Y. Ogata, and K. Aoki, "Mechanical characteristics of natural and artificial gas hydrate bearing sediments," in *Proc. 6th Int. Conf. Gas Hydrates*, 2008, pp. 6–10.
- [21] T. S. Yun, J. C. Santamarina, and C. Ruppel, "Mechanical properties of sand, silt, and clay containing tetrahydrofuran hydrate," *J. Geophys. Res., Solid Earth*, vol. 112, no. B4, 2007, Art. no. B04106.
- [22] Y.-H. Li, Y.-C. Song, F. Yu, W.-G. Liu, and J.-F. Zhao, "Experimental study on mechanical properties of gas hydrate-bearing sediments using kaolin clay," *China Ocean Eng.*, vol. 25, no. 1, p. 113, 2011.
- [23] M. Hyodo, Y. Li, J. Yoneda, Y. Nakata, N. Yoshimoto, A. Nishimura, and Y. Song, "Mechanical behavior of gas-saturated methane hydrate-bearing sediments," *J. Geophys. Res., Solid Earth*, vol. 118, no. 10, pp. 5185–5194, 2013.
- [24] J.-Y. Lee, "Hydrate-bearing sediments: Formation and geophysical properties," Ph.D. dissertation, Georgia Inst. Technol., Atlanta, GA, USA, 2007.

- [25] U. Majumdar, A. E. Cook, M. Scharenberg, A. Burchwell, S. Ismail, M. Frye, and W. Shedd, "Semi-quantitative gas hydrate assessment from petroleum industry well logs in the northern Gulf of Mexico," *Mar. Petroleum Geol.*, vol. 85, pp. 233–241, Aug. 2017.
- [26] Y. Sun, D. Goldberg, T. Collett, and R. Hunter, "High-resolution well-log derived dielectric properties of gas-hydrate-bearing sediments, Mount Elbert Gas Hydrate Stratigraphic Test Well, Alaska North Slope," *Mar. Petroleum Geol.*, vol. 28, no. 2, pp. 450–459, 2011.
- [27] K. Haukalid and K. J. Folgerø, "Broad-band permittivity measurements of formation of gas hydrate layers using open-ended coaxial probes," *Energy Fuel*, vol. 30, no. 9, pp. 7196–7205, 2016.
- [28] J. Santamarina, F. Francisca, T. Yun, J. Lee, A. Martin, and C. Ruppel, "Mechanical, thermal, and electrical properties of hydrate-bearing sediments," in *Proc. AAPG Hedberg Conf. Gas Hydrates: Energy Resource Potential Assoc. Geol. Hazards*, Vancouver, BC, Canada, 2004, pp. 1–4.
- [29] R. Pérez-Aparicio, D. Cottinet, C. Crauste-Thibierge, L. Vanel, P. Sotta, J.-Y. Delannoy, D. R. Long, and S. Ciliberto, "Dielectric spectroscopy of a stretched polymer glass: heterogeneous dynamics and plasticity," *Macromolecules*, vol. 49, no. 10, pp. 3889–3898, 2016.
- [30] S. A. Komarov, A. S. Komarov, D. G. Barber, M. J. L. Lemes, and S. Rysgaard, "Open-ended coaxial probe technique for dielectric spectroscopy of artificially grown sea ice," *IEEE Trans. Geosci. Remote Sens.*, vol. 54, no. 8, pp. 4941–4951, Aug. 2016.
- [31] M. V. Traffano-Schiffo, M. Castro-Giraldez, V. Herrero, R. J. Colom, and P. J. Fito, "Development of a non-destructive detection system of deep pectoral myopathy in poultry by dielectric spectroscopy," *J. Food Eng.*, vol. 237, pp. 137–145, Nov. 2018.
- [32] G. G. B. Nielsen, A. Kjør, P. L. Kløsgen, P. L. Hansen, A. C. Simonsen, and B. Jørgensen, "Dielectric spectroscopy for evaluating dry matter content of potato tubers," *J. Food Eng.*, vol. 189, pp. 9–16, Nov. 2016.
- [33] A. K. Jha and M. J. Akhtar, "A generalized rectangular cavity approach for determination of complex permittivity of materials," *IEEE Trans. Instrum. Meas.*, vol. 63, no. 11, pp. 2632–2641, Nov. 2014.
- [34] K. Takeya, R. Takahashi, T. Fukui, S. R. Tripathi, and K. Kawase, "Terahertz characterization of propane hydrate," *Jpn. J. Appl. Phys.*, vol. 58, no. 3, 2019, Art. no. 032003.
- [35] D. Kawakami and H. Tabata, "THz-TDS measurements of hydration state of bio related materials and data analysis by machine learning," in *Proc. 43rd Int. Conf. Infr., Millim., THz. Waves (IRMMW-THz)*, Sep. 2018, p. 1.
- [36] M. Tyagi and S. S. N. Murthy, "Dielectric relaxation in ice and ice clathrates and its connection to the low-temperature phase transition induced by alkali hydroxides as dopants," *J. Phys. Chem. A*, vol. 106, no. 20, pp. 5072–5080, 2002.
- [37] W. S. Brey, Jr., and H. P. Williams, "Dielectric properties of ice and water clathrates," *J. Phys. Chem.*, vol. 72, no. 1, pp. 49–52, 1968.
- [38] D. Davidson and J. Ripmester, "Clathrate ices—Recent results," *J. Glaciol.*, vol. 21, no. 85, pp. 33–49, 1978.
- [39] S. Evans, "Dielectric properties of ice and snow—A review," *J. Glaciol.*, vol. 5, no. 42, pp. 773–792, 1965.
- [40] A. K. Jonscher, "The 'universal' dielectric response," in *Proc. Conf. Elect. Insul. Dielectr. Phenomena*, vol. 267, 2002, pp. 673–679.
- [41] F. Franks, *Water A Comprehensive Treatise: Aqueous Solutions of Amphiphiles and Macromolecules*, vol. 4. New York, NY, USA: Plenum Press, 1975.
- [42] S. R. Gough, R. E. Hawkins, B. Morris, and D. W. Davidson, "Dielectric properties of some clathrate hydrates of structure II," *Can. J. Chem.*, vol. 77, no. 25, pp. 2969–2976, 1973.
- [43] K. Asami, "Characterization of heterogeneous systems by dielectric spectroscopy," *Prog. Polym. Sci.*, vol. 27, no. 8, pp. 1617–1659, 2002.
- [44] B. Morris and D. W. Davidson, "A clathrate hydrate of cyclobutane: Dielectric relaxation of the host and guest molecules," *Can. J. Chem.*, vol. 49, no. 49, pp. 1243–1251, 1971.
- [45] R. E. Hawkins and D. W. Davidson, "Dielectric relaxation in the clathrate hydrates of some cyclic ethers," *J. Phys. Chem.*, vol. 70, no. 6, pp. 1889–1894, 1966.
- [46] F. E. Critchfield, J. A. Gibson Jr, and J. L. Hall, "Dielectric constant and refractive index from 20 to 35° and density at 25° for the system tetrahydrofuran–water," *J. Amer. Chem. Soc.*, vol. 75, no. 23, pp. 6044–6045, 1953.
- [47] A. C. Kumbharkhane, S. N. Helambe, M. P. Lokhande, S. Doraiswamy, and S. C. Mehrotra, "Structural study of aqueous solutions of tetrahydrofuran and acetone mixtures using dielectric relaxation technique," *Pramana*, vol. 46, no. 2, pp. 91–98, 1996.
- [48] K. Haukalid and K. Folgerø, "Dielectric mixture models for hydrate formation and agglomeration," in *Proc. 12th Int. Conf. Electromagn. Wave Interact. Water Moist Substances (ISEMA)*, Jun. 2018, pp. 1–9.
- [49] A. H. Sihvola and J. A. Kong, "Effective permittivity of dielectric mixtures," *IEEE Trans. Geosci. Remote Sens.*, vol. GRS-26, no. 4, pp. 420–429, Jul. 1988.
- [50] Y. Chen and D. Or, "Geometrical factors and interfacial processes affecting complex dielectric permittivity of partially saturated porous media," *Water Resour. Res.*, vol. 42, no. 6, 2006, Art. no. W06423.
- [51] V. L. Mironov, M. C. Dobson, V. H. Kaupp, S. A. Komarov, and V. N. Kleshchenko, "Generalized refractive mixing dielectric model for moist soils," *IEEE Trans. Geosci. Remote Sens.*, vol. 42, no. 4, pp. 773–785, Apr. 2004.
- [52] C. Matzler, "Microwave permittivity of dry sand," *IEEE Trans. Geosci. Remote Sens.*, vol. 36, no. 1, pp. 317–319, Jan. 1998.
- [53] O. A. L. de Lima and M. M. Sharma, "A generalized Maxwell-Wagner theory for membrane polarization in shaly sands," *Geophysics*, vol. 57, no. 3, pp. 431–440, 1992.
- [54] Y. Chen and D. Or, "Effects of Maxwell-Wagner polarization on soil complex dielectric permittivity under variable temperature and electrical conductivity," *Water Resour. Res.*, vol. 42, no. 6, 2006, Art. no. W06424.
- [55] T. Hanai, "Theory of the dielectric dispersion due to the interfacial polarization and its application to emulsions," *Kolloid-Zeitschrift*, vol. 171, no. 1, pp. 23–31, 1960.



BIN WANG received the B.S. degree in applied physics from Qingdao University, in 2010, and the Ph.D. degree in radio physics from Shandong University, China, in 2015.

From 2015 to 2017, he was a Lecturer with the China University of Petroleum (East China). Since 2018, he has been an Associate Professor. His research interests include detection technology and automatic device, permittivity measurement, dielectric logging method, measurement of gas hydrate, and numerical simulation method of electromagnetic.



ZHONGHAO ZHANG received the B.S. degree in building electrical and intelligent engineering from the School of Information and Electrical Engineering, Shandong Jianzhu University, in 2017. He is currently pursuing the M.S. degree with the College of Control Science and Engineering, China University of Petroleum (East China), Qingdao, China.

From 2017 to 2019, he was a graduate student with the China University of Petroleum (East China). His research interests include detection technology and automatic device.



LANCHANG XING (M'17) received the B.S. degree in automation and the M.S. degree in control science and engineering from the China University of Petroleum (East China), in 2005 and 2008, respectively, and the Ph.D. degree in process system engineering from Cranfield University, U.K., in 2012.

From 2012 to 2015, he was a Lecturer with the China University of Petroleum (East China). Since 2016, he has been an Associate Professor. His research interests include detection technology and automatic device, computer measurement and control systems, measurement of gas hydrate and multiphase flow, and multiphysical field coupling numerical simulation method.

• • •

A Borehole Fluid Saturation Evaluation Method Using Unidirectional Monopole UWB Antenna

Bin Wang, Kang Li, *Member, IEEE*, Fan-Min Kong, Jia Zhao, and Yang Gao

Abstract—A method based on a unidirectional monopole ultra-wideband antenna was proposed to evaluate the fluid saturation around borehole. The spectrum span of the excitation signal covered 750 MHz to 2.5 GHz and the slot antenna was optimized to transmit lateral wave more efficiently. The pulsed evaluation method offers more superiority when compared with the electromagnetic propagation tool and dielectric tools based on discrete frequencies. Measurement of complex permittivity in a wide-band spectrum provides more accurate fluid saturation evaluation around the borehole. This method has been proven to operate effectively in a borehole filled with oil-based mud and to launch enough wave energy into the formation directionally. In addition, the proposed scheme is verified by using finite-difference time-domain method, and the simulation results show that this design adapts to evaluation of the fluid saturation and the detection of formation boundary. This scheme may be used as an alternative tool for logging while drilling the imaging application.

Index Terms—Complex permittivity, dielectric tool, fluid saturation, ultrawideband (UWB) antenna.

I. INTRODUCTION

RECENT research on complex permittivity survey has been prompted by an increasing interest in the formation fluid saturation for residual oil and reservoir evaluation. The dielectric measurements are particularly useful in characterizing heavy-oil reservoirs. As early as the 1950s, petrophysicists recognized that the dielectric permittivity of reservoir rock measured in the range of microwave was primarily controlled by the amount and kind of fluid in the pores of the rocks [1], and this way, fluid containment and porosity of formation could be interpreted through measurements of the dielectric permittivity.

The electromagnetic (EM) propagation tool (EPT) was introduced as a supplemental technology for the oil and gas industry in the late 1970s [2]. It operated at a single frequency of 1.1 GHz, and from the measured phase shift and attenuation

of wave traveling through the formation of petrophysical properties, dielectric permittivity and porosity were derived. After the introduction of the EPT, other dielectric tools based on single frequency were developed. Data recorded at different frequencies often yielded different results and comparing the results between wells was often problematic. Those differences can be attributable to the frequency dependence of the dielectric properties of the formation.

The electric properties of formation could be illustrated by complex permittivity, which contains information of both dielectric and conductive properties. Although the complex permittivity of dry samples is constant over a wide range, because several kinds of polarizations exist in fluid saturated formation at microwave range, complex permittivity is frequency dispersive there [1]. Thus, one single frequency point is obviously limited in evaluating the complex permittivity of the formation.

The dielectric scanner tool was developed to provide dispersive complex permittivity of formation at four discrete frequencies in a range from 20 MHz to 1 GHz [3]. Porosity and fluid saturation are available using dielectric permittivity and conductivity analysis from the dielectric scanner tool at the four different frequencies. Because of great differences existing between dispersive properties of permittivity at the water-saturated zone and the pay zone, dielectric information provides clear benefits for carbonate reservoir interpretation, shaly sand analysis, and heavy-oil reservoir evaluation [4]. Although the dielectric scanner offers extra information log analysis needs, it could not provide an entire and continuous complex permittivity evaluation in the operation frequency range after all. Moreover, the dipole antennas mounted in the tool could not supply high emission efficiency for every operation frequency. Thus, there are still improvements to evolve dielectric logging tools.

This letter demonstrates a borehole fluid saturation evaluation method based on wideband detection in both time and frequency domains. A unidirectional monopole slot antenna was optimized for the pulse emission with an operating band from 750 MHz to 2.5 GHz, and the antenna performance was tested. The permittivity evaluation system constituted by such antennas and other basic assembly parts was tested in layered formations with different fluid saturations. A numerical simulated study of the system response on both the time domain and frequency domain would confirm the feasibility of the innovative method. Furthermore, the electric field distribution in the borehole was presented for the detection scope discussion. The simulation results were obtained from finite-difference time-domain (FDTD) codes.

Manuscript received September 24, 2013; revised June 21, 2014; accepted June 23, 2014. Date of publication August 22, 2014; date of current version September 18, 2014. This work was supported by the National Basic Program of China (973 Program) under Grant 2009CB930503 and Grant 2009CB930501, by the National Science Foundation of China for Youths under Grant 61205145, and by the Independent Innovation Foundation of Shandong University under Grant 2011GN060.

The authors are with the School of Information Science and Engineering, Shandong University, Jinan 250100, China (e-mail: wb1988t@163.com; kangli@sdu.edu.cn; fanminkong@163.com; zhaojia@sdu.edu.cn; gy10200515shx@163.com).

Color versions of one or more of the figures in this paper are available online at <http://ieeexplore.ieee.org>.

Digital Object Identifier 10.1109/LGRS.2014.2333588

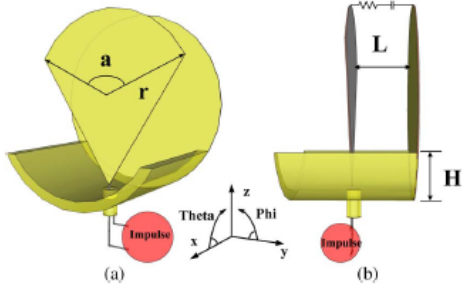


Fig. 1. Diagram of the antenna. (a) Three-dimensional view. (b) Side view.

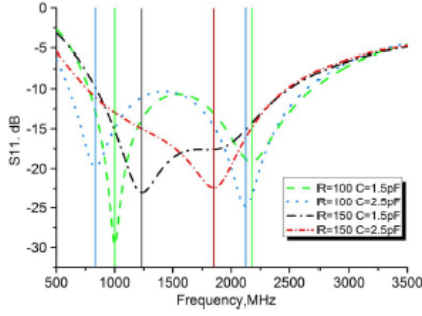


Fig. 2. Simulated S_{11} in broadband with different loadings.

II. ANTENNA OPTIMIZATION

We made improvements on a monopole antenna described in [5] to optimize antenna parameters for the complex permittivity evaluation method. The geometrical parameter and the model shape are shown in Fig. 1. The antenna contains a fan-shaped monopole, thickened cavity, and a parasitic disc. Between the tops of the monopole and the disk, a resistor and a capacitor are mounted, and the antenna was fed by a coaxial line from the bottom. As Fig. 1 shows, the dimension of the antenna is: $r = 20$ mm, $\alpha = 120^\circ$, $L = 12.5$ mm, $H = 10$ mm, with the monopole installed at the middle point of the cavity. The monopole and parasitic disc are made of 0.2-mm-thick copper sheets, whereas the regular cavity is made of a 2-mm-thick copper sheet.

The terminal load was always used to reduce the reflection and ensure the broadband characteristics. The effects of the loaded R and C have been investigated, and the S_{11} in broadband varies with the terminal load. Fig. 2 shows the simulated S_{11} , which was obtained in air with different resistor and capacitor loadings. When the load was $100\ \Omega$ and $1.5\ \text{pF}$ as the previous design [5], around $1.5\ \text{GHz}$, S_{11} is unsatisfactorily small, whereas $1.5\ \text{GHz}$ is very close to the center frequency of the pulse used as the excitation signal. When the resistor was set as $150\ \Omega$, the two resonance frequency points tended to converge to one point located between the previous two. Then, the resonance point shifted to a range between 1.5 and $2\ \text{GHz}$ when the capacitor was raised to $2.5\ \text{pF}$. This way, we obtained the operating band of the optimized antenna covering $750\ \text{MHz}$ to $2.5\ \text{GHz}$, and the resonance point matched the center frequency of the excitation pulse.

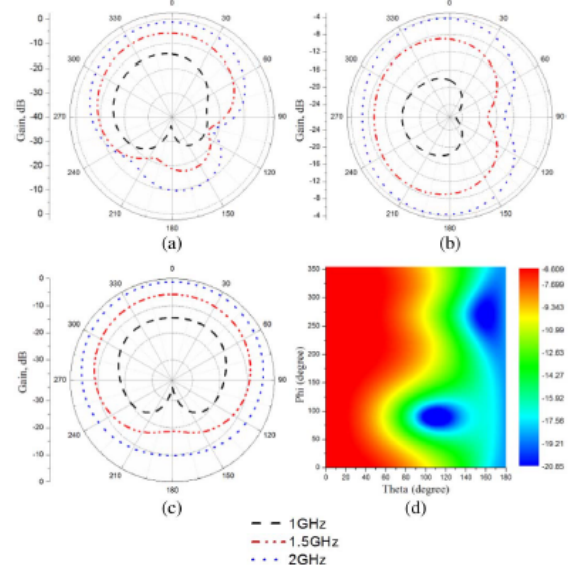


Fig. 3. Radiation pattern of the antenna. (a) xz -plane at 1, 1.5, and 2 GHz. (b) xy -plane at 1, 1.5, and 2 GHz. (c) yz -plane at 1, 1.5, and 2 GHz. (d) Contour map at 1.6 GHz.

The antenna's directivity pattern at broadband when operating in oil-based mud was studied. The simulated directional patterns at 1, 1.5, and 2 GHz were selected as examples shown in Fig. 3. The coordinate axis is same as that shown in Fig. 1 and Φ and Θ of the polar coordinate system in Fig. 3(d) are also shown in Fig. 1. Because the antenna structure is bilateral symmetrical about the xz -plane, the radiation pattern in the yz -plane and xy -plane, which is perpendicular to the xz -plane, as in Fig. 3(b) and (c), is mirror symmetrical and toward the same side of the borehole among the operating frequency bands. In the xz -plane as in Fig. 3(a), the antenna also showed an obvious directivity, and the power front-to-back ratio was bigger than 6:1 among the wideband, whereas structure in xz -plane is unsymmetrical; thus, the radiation pattern was not symmetrical in Fig. 3(a). Fig. 3(d) shows the contour map at 1.6 GHz, which was the center frequency of the impulse, and strong unidirectivity allowed the antenna to have unidirectional detecting ability.

III. RESULTS AND ANALYSIS

Because of the huge difference between matrix and fluid, particularly water permittivities, the dielectric permittivity of a reservoir sample measured in the microwave range is primarily a function of the fluid filling the pores. To be able to deduce the effective permittivity from the volumetric fraction of matrix and pore fluid, many mixing laws have been raised. The generalized refractive mixing dielectric model was proved practical against experimental data over a wide frequency range from 300 kHz to 3 GHz [6]. It could be presented as

$$\sqrt{\epsilon_{\text{for}}} = \begin{cases} \sqrt{\epsilon_d} + (\sqrt{\epsilon_b} - 1)W, & W \leq W_t \\ \sqrt{\epsilon_d} + (\sqrt{\epsilon_b} - 1)W_t + (\sqrt{\epsilon_f} - 1)(W - W_t), & W \geq W_t \end{cases} \quad (1)$$

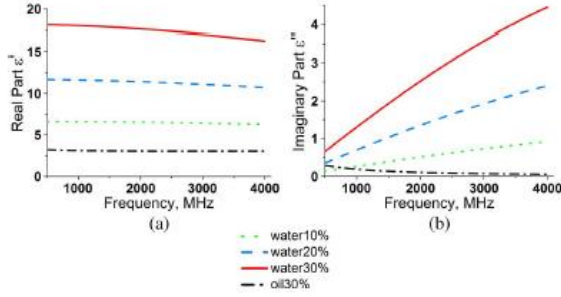


Fig. 4. Complex permittivity of formations with different fluid saturation. (a) Real part ϵ' . (b) Imaginary part ϵ'' .

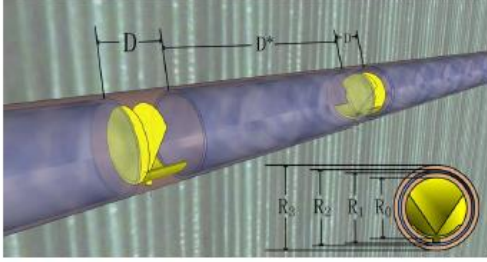


Fig. 5. Schematic and physical dimension of the detecting system.

where $\epsilon_{\text{formation}}$, ϵ_d , ϵ_b , and ϵ_f refer to the complex permittivity of formation, dry matrix, bound fluid, and free fluid, respectively. W and W_t are the saturation and maximum bound fluid fraction. Sand formations with different water/oil saturations were selected as samples in the following numerical simulation, and the corresponding complex permittivities are shown in Fig. 4.

The schematic diagram and physical dimension of the simulating model of this system are shown in Fig. 5. The antennas used in the system are same as that shown in Fig. 1 and their outer diameter $R_0 = 40$ mm. The transmitting and receiving antennas were mounted along the metal drill collar with outer diameter $R_2 = 46$ mm and inner diameter $R_1 = 40$ mm in a single borehole, whose diameter $R_3 = 50$ mm. Two slots with length $D = 45$ mm are set at the center of each antenna for signal emitting, and the distance between the two slots D^* was 230 mm. Oil-based mud is used as drilling mud in practice, whereas the permittivity of the oil-based mud is about 2–3; thus, we here set the borehole as oil-based mud filled with $\epsilon^* = 2 + 0i$ in all the following physical simulation models. The whole simulating area is $2 \text{ m} \times 2 \text{ m} \times 2 \text{ m}$, and the boundary conditions are set as perfect matched layer. Antennas and drilling collar are set perfect dielectric conductor (PEC), and all the materials are homogeneous and isotropic. In practical drilling, borehole fluid would invade into formation depending on pressure, drilling azimuth, and many other factors. The primary intention of this letter is to validate the system's ability of evaluating fluid saturation around the borehole. Thus, for simplification, the invaded zone has not been taken into consideration in the following computing.

A modulated Gaussian pulse was the monocycle impulse of the transmitting antenna. The waveform and the spectrum are plotted in Fig. 6(a) and (b). The peak-to-peak width of the pulse

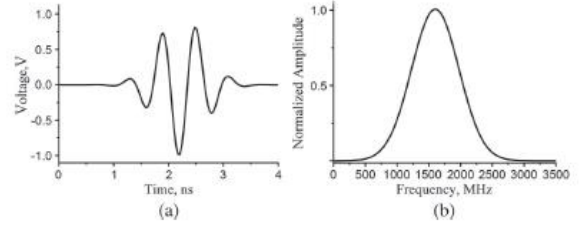


Fig. 6. Source waveform applied to the transmitting antenna. (a) Time-domain waveform. (b) Spectrum of the excitation signal.

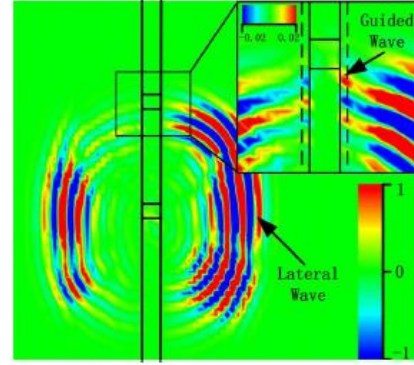


Fig. 7. FDTD simulation shows the wave propagation at 6 ns after the excitation. The borehole contains oil-based mud, and formation is sand with 30% water.

was about 250 ps, and the center frequency was 1.6 GHz. The frequency bandwidth of the impulse covered the sensitive range of the complex permittivity.

As early research on dielectric tools reported, excited energy could be divided into two primary parts: lateral wave across the invaded zone and the guided wave in the borehole [7], [8]. The proportion of the lateral wave, which is the main carrier of formation dielectric properties, depends on transmitter structure and borehole EM properties. Numerical study with FDTD helps one to analyze the wave propagation in the prototype dielectric tool testing [9]. The electric field intensity obtained by FDTD simulation in the model with a formation of 30% water content is presented in Fig. 7. It was obviously the lateral wave directionally propagated into formation as the radiation pattern shows. Meanwhile, the detailed drawing along the borehole shown in the inset of Fig. 7 reduced the color scale by 100 times so that the guided wave, whose intensity was two orders of magnitude weaker than the lateral wave, could be displayed. Guided wave inside the borehole was too weak to be observed in the full-scale drawing, because the most excited energy was transferred to the lateral wave. The refractive index of the oil-based mud is much smaller than that of the formation, and the annular space between the borehole and collar is too narrow to meet guided conditions; moreover, the space between the slot antenna gap and the borehole is only 5 mm, the incident angle of the transmitting wave could hardly excite guide mode. Although the guided wave is formed around the transmitter, it would radiate EM energy into the formation heavily, and its amplitude would decrease gravely.

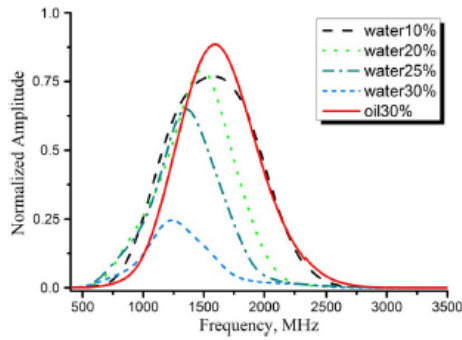


Fig. 8. Response signals obtained from the receiving antenna when the system operated in formations with different fluid saturations.

To explore the system response when operating in different fluid-containing formations, we choose sandy reservoir formations shown in Fig. 4 as typical samples in the simulation. Operating with Gaussian monocycle aforementioned, the signals obtained by the receiving antenna are presented in Fig. 8. The response amplitude became gradually smaller as water saturation increased, and the center frequency of the response spectrum had a redshift. The imaginary part of the water-containing samples' complex permittivity obviously grew in a span larger than 1 GHz. This part represents the dielectric loss; thus, more excited energy is absorbed in the span above the center frequency. On the contrary, the oil-containing formation did not create much shape change of the spectrum when compared with the excitation signal, because the resonance peak of oil is not in this frequency span and the complex permittivity curve is very smooth, and thus, the oil-filled formation's absorption to the wave is generally even and much smaller than that of water formation.

To validate the capability of the system to distinguish a reservoir layer from the surrounding formation, the operation in a layered formation was studied. A sandy formation containing 30% oil with a thickness of 600 mm was surrounded by a formation of 30% water. The borehole vertically passes through the layered formation, and the response signals of the system are presented in Fig. 9. As Fig. 9(a) shows, keeping the porosity and fluid saturation constant, response spectra in water-containing and oil-containing formations have distinct differences: The spectrum of receiving signals has larger amplitude when the system is processing in an oil-filled formation (depth from -300 to 300 mm). Furthermore, the center frequency of the spectrum drifts from 1.6 to 1.3 GHz when the system moves to a water-containing formation from a reservoir formation, and as was previously stated, receiving frequency shapes were decided by pore fluid permittivity. Thus, from the frequency response/depth chart, it is easy to obtain accurate evaluation on the type of the pore fluid and its saturation level. An evaluation deviation of about 50 mm is observed at the boundaries of the two formations. The cause of this deviation will be discussed later.

Water-filled porosity from the earliest EPT was computed following the t_{po} method, which is based on the propagation time of the EM waves as they pass through rock. Formations, however, consist of more than just water. Only t_{po} method was

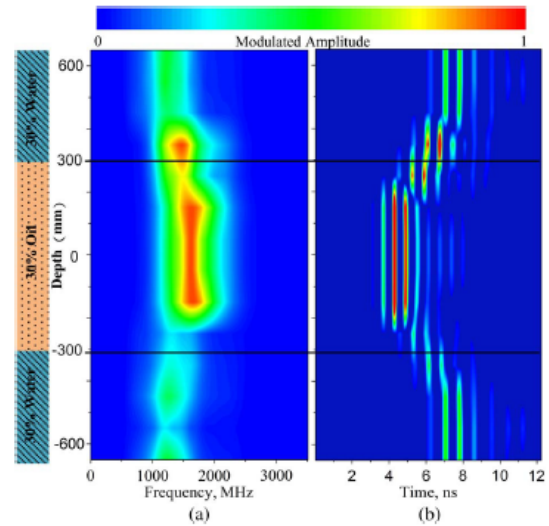


Fig. 9. (a) Frequency response/depth diagram of the evaluation system processing in a layered formation. (b) Pulse strength/depth diagram in the time domain of the evaluation system processing in a layered formation.

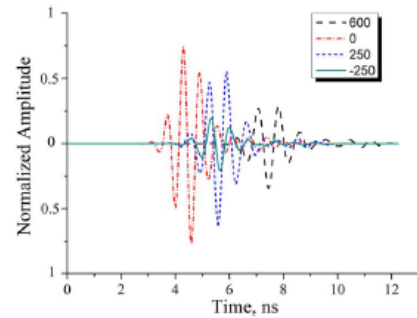


Fig. 10. Normalized waveform of response signals at a depth of 600, 0, 250, and -250 mm.

not adequate for computing fluid saturation, but it could provide complete saturation evaluation with the frequency response previously introduced.

Fig. 9(b) shows that the receiving pulse strength varies with time and the detecting depth. Time counting began from the triggering of the impulse signal in the transmitting antenna. When the depth is in the ranges of 450 – 700 mm and -450 to 700 mm, wave packets were dispersed by water-containing formation, whereas wave packets in pay layer (depth from about $+250$ to -250 mm) kept the shapes constant. It can be thus seen that time-domain record could also illustrate dispersion of formation permittivity. Wave propagation time t_{po} in surrounding layers was about 3 ns larger than that in pay layer. Although there was a relative difference of the pulse strength at the two dividing lines (± 300 mm) similar to the spectrum diagram indicated, t_{po} at the dividing lines symmetrically changed.

Fig. 10 presents a normalized amplitude of waveforms at 0 , 600 , and ± 250 mm to explore the cause of the discrepancy. The wave velocity in homogeneous media is $v_0\sqrt{\epsilon_r\mu_r}$; thus, the propagation time t_{po} in surrounding formations is about 2.4 times longer than that in the reservoir formation. We found that

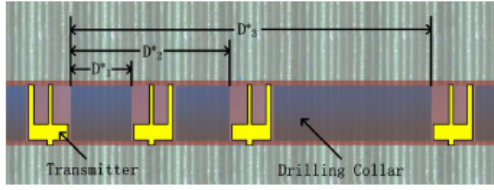


Fig. 11. Structure of multidepth detecting system.

the t_{po} varying tendency was regular at the layer boundaries of ± 250 mm and conformed to the symmetrical formation. Abnormally, the amplitude at -250 mm was even smaller than at 600 mm, whereas the amplitude at the other dividing line 250 mm gradually varied. Thus, we can infer that the abnormality of the pulse strength at boundaries is not caused by a defect of the detecting system but by the reflection at the formation interfaces.

The simulation results shown here demonstrate that the new method provides continuously satisfactory dispersion information of permittivity around the borehole in a fairly broad band. At the same time, pulse/depth image could help to detect layer boundaries, and referential permittivity evaluation could be acquired from t_{po} . Since near borehole is usually complicated due to the drilling-mud invasion, a multispace system is designed, as shown in Fig. 11, for multidepth measurement. The three receivers are mounted facing the transmitter with spaces D_1^* , D_2^* , and D_3^* . The spaces between those antennas can be determined according to specific environment and requirement.

IV. CONCLUSION

The design of a formation saturation evaluation method based on ultrawideband (UWB) pulse propagation in a borehole has been presented in this letter. An optimized monopole antenna has been designed and tested for a proposed UWB pulse from 750 MHz to 2.5 GHz. The results show that the system is effective for directional lateral wave transmitting when operating in oil-based mud-filled borehole. From the response spectrum in the frequency domain, it is able to obtain dielectric

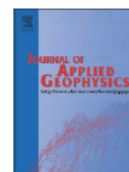
dispersive characteristics in a continuous wideband, which has significant importance to determine fluid saturation in reservoir layers. Furthermore, the pulse response in time domain can be used in the detection of formation boundary and the location of pay layers. Multidepth measurement for complexity of the invasion zone could be realized by installing multireceivers. When compared with the conventional dielectric logging tools, this proposed method can provide a directional dispersive permittivity evaluation in a wideband and increases the evaluation efficiency of real-time formation fluid saturation.

ACKNOWLEDGMENT

The author would like to thank Dr. E. C. Mignot, Shandong University, for linguistic advice.

REFERENCES

- [1] A. R. Von Hippel, *Dielectric Materials and Applications*. Norwood, MA, USA: Artech House, 1954, pp. 36–40.
- [2] R. P. Wharton, R. N. Rau, and D. L. Best, "Electromagnetic propagation logging: Advances in technique and interpretation," presented at the SPE Ann. Tech. Conf. Exhibition, Dallas, TX, USA, 1980, Paper SPE-9267-MS.
- [3] M. Hizem *et al.*, "Dielectric dispersion: A new wireline petrophysical measurement," presented at the SPE Ann. Tech. Conf. Exhibition, Denver, CO, USA, Sep., 2008, Paper SPE-116130-MS.
- [4] J. Little, D. Julander, L. Knauer, J. T. Aultman, and J. L. Hemingway, "Dielectric dispersion measurements in California heavy oil reservoirs," presented at the SPWLA 51st Annual Logging Symp., Perth, WA, Australia, 2010, Paper 2010fe.
- [5] Y.-T. Li *et al.*, "A unidirectional cylindrical conformal monopole antenna designed for impulse radar system," *IEEE Antennas Wireless Propag. Lett.*, vol. 10, pp. 1397–1400, Dec. 2011.
- [6] V. L. Mironov, M. C. Dobson, V. H. Kaupp, S. A. Komarov, and V. N. Kleshchenko, "Generalized refractive mixing dielectric model for moist soils," *IEEE Trans. Geosci. Remote Sens.*, vol. 42, no. 4, pp. 773–785, Apr. 2004.
- [7] J. R. Wait, "General solution for excitation by slotted aperture source in conducting cylinder with concentric layering," *IEEE Trans. Microw. Theory Tech.*, vol. 35, no. 3, pp. 321–325, Mar. 1987.
- [8] W. C. Chew and S. C. Gianzero, "Theoretical investigation of the electromagnetic wave propagation tool," *IEEE Trans. Geosci. Remote Sens.*, vol. GE-19, no. 1, pp. 1–7, Jan. 1981.
- [9] K. J. Ellefsen, J. D. Abraham, D. L. Wright, and A. T. Mazzella, "Numerical study of electromagnetic waves generated by a prototype dielectric logging tool," *Geophysics*, vol. 69, no. 1, pp. 64–77, 2004.



A dielectric logging tool with insulated collar for formation fluid detection around borehole



Bin Wang, Kang Li *, Fan-Min Kong, Jia Zhao

School of Information Science and Engineering, Shandong University, No. 27, Shanda South Road, Jinan, Shandong Province 250100, PR China

ARTICLE INFO

Article history:

Received 14 August 2014

Received in revised form 16 March 2015

Accepted 1 May 2015

Available online 7 May 2015

Keywords:

Surface wave

Metal collar

Dielectric tools

UWB antennas

ABSTRACT

A dielectric tool with insulated collar for analyzing fluid saturation outside a borehole was introduced. The UWB (ultra-wideband) antenna mounted on the tool was optimized to launch a transient pulse. The broadband evaluation method provided more advantages when compared with traditional dielectric tools. The EM (electromagnetic) power distribution outside the borehole was studied, and it was shown that energy was propagated in two modes. Furthermore, the mechanism of the modes was discussed. In order to increase this tool's investigation depth, a novel insulated collar was introduced. In addition, operation in difference formations was discussed and this tool proved to be able to efficiently launch lateral EM waves. Response voltages indicated that the proposed scheme was able to evaluate the fluid saturation of reservoir formations and dielectric dispersion properties. It may be used as an alternative tool for imaging logging applications.

© 2015 Elsevier B.V. All rights reserved.

1. Introduction

Dielectric measurements have been used in different kinds of reservoirs to determine dielectric properties of the zone near boreholes since 1970s. Recent research on complex permittivity surveys was prompted by an increasing interest in the fluid saturation of formations, particularly in residual oil and heavier reservoirs. Since the 1980s electromagnetic propagation tools (EPT) have been added to the standard logging suite to aid in the effort of locating reservoirs and quantifying the fluid saturation (Chew and Gianzero, 1981). EPT operating at a single frequency of 1.1 GHz, and from measured phase shift and attenuation of wave traveling through the formation have determined petro-physical properties including dielectric permittivity and porosity.

After introduction of the EPT, other dielectric tools based on a single frequency and slot antennas were developed. Logging data recorded at different frequencies often yielded different results. Comparing the fluid saturation and porosity output from EPT with other tools was often a problem. Those differences were attributed to the frequency dispersion of the dielectric properties. The concept of complex permittivity was proposed in order to combine materials' dielectric and conductive properties (Von Hippel, 1954). Although the complex permittivity of a dry formation is constant over a wide range, in practice reservoir formations are filled with fluids. Complex permittivity of invaded zone and virgin formation are frequency dispersive because of several polarizations in a fluid saturated formation at the microwave range (Von Hippel, 1954). For the dispersion of dielectric properties, a single frequency method has serious limitation in evaluating the complex

permittivity of the formation. Furthermore, the tool's mandrel design makes it quite easy to limit energy along the metal collar as a non-radiating wave (Wait, 1987), but it seriously decreases the detection depth of EPT, which will be explained in this paper.

The dielectric scanner was developed to quantify complex permittivity at different frequencies (Hizem et al., 2008). Transmitters and receivers are mounted on a pad in contact with the borehole and raw measurement of attenuation and phase shift are obtained at four frequency points between 20 MHz to 1 GHz. Because great differences exist between permittivity dispersion properties of the water saturated zone and the reservoir zone, dielectric information at wide band provides competitive advantages for carbonate reservoir interpretation, shaly sand analysis, and heavy-oil reservoir evaluation (Little et al., 2010). The dielectric scanner offers extra logging information, but it would be better to have a swept frequency dielectric measurement in the broadband. Moreover, dipole antennas mounted in the tool cannot supply efficient high emission for each operating frequency. Thus, there are still possible improvements to be made in the evolution of dielectric logging tools.

This study demonstrates a new logging tool as an improvement to traditional dielectric tools for formation complex permittivity and fluid saturation evaluation. First, the design of the proposed dielectric tool based on UWB antennas is described, and detailed geometrical parameters are presented. A monopole slot antenna was optimized for the pulse emission with an operating band from 750 MHz to 2.5 GHz. Then EM energy distribution around the tool was studied by both numerical simulation and theoretical analysis, and the design of the drilling collar was modified in order to improve the lateral wave launching efficiency. The proposed tool was tested in formations with different fluid saturations, and response voltages were presented and analyzed in both the

* Corresponding author.

E-mail address: kangli@sdu.edu.cn (K. Li).

time domain and frequency domain. The simulation results were obtained from finite-difference time-domain (FDTD) codes.

2. Design of the dielectric tool

UWB monopole antennas as originally described by Li (Li et al., 2011) are used as transmitters and receivers of the proposed dielectric tool. The model shape and size of the monopole antenna are shown in Fig. 1(a): $r = 20$ mm, $\alpha = 120^\circ$, $L = 12.5$ mm, and $H = 10$ mm, with the monopole installed at the middle point of the cavity, a resistor $R = 150 \Omega$ and capacitor $C = 2.5$ pF are loaded between the tops of the monopole, while the disk and the antenna are fed by a coaxial line from the bottom. The load is used to reduce terminal reflection and ensure the broadband characteristics. Simulated S_{11} parameters of the proposed UWB antenna with different terminal loads obtained in air are shown in Fig. 1(b). The increase from 100 to 150 for the loaded resistor has combined the two very sharp resonance points into one. Then, the resonance point shifted to a range between 1.5 and 2 GHz, when the capacitor was raised to 2.5 pF. When the load was set as 150 Ω and 2.5 pF, we obtained a -10 dB operating band covering 750 MHz to 2.5 GHz, and the resonance point matched the center frequency of the excitation pulse.

The tool's geometrical parameters are shown in a lateral view in Fig. 2(a): The transmitter and receiver are mounted along the metal drilling collar, the length of slots opened on the collar for the antennas is $D^*_1 = 45$ mm, the cylindrical part between the two antennas is made of PVC with length $D^*_2 = 230$ mm which is widely used in borehole radar and antennas, and reflecting plates are stuck to the two terminals of the PVC cylinder. The monopole and parasitic disk of the antennas and reflecting plates are made of 0.2 mm thick copper sheets while the cambered cavity is made of a 2 mm thick copper sheet. The 3D schematic diagram of this system is shown in Fig. 2(b) and the size

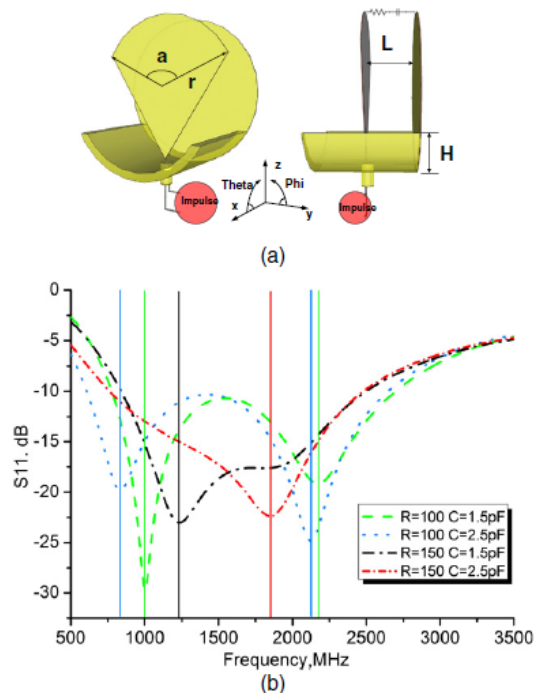


Fig. 1. Diagram and electrical properties of the UWB antenna: (a) 3D plot and physical dimension of the antenna and (b) simulated S_{11} of UWB antenna in broadband with different loadings.

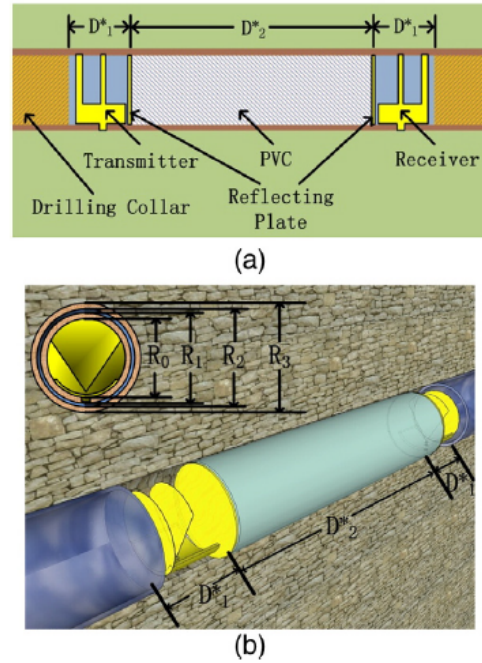


Fig. 2. Diagram of the dielectric tool: (a) lateral view of the dielectric tool and (b) 3D view of the dielectric tool.

of the tool is shown in an axial view in the inset. The outer diameter of the antennas is $R_0 = 40$ mm, and the transmitting and receiving antennas were mounted along the metal drill collar with an outer diameter $R_2 = 46$ mm and inner diameter $R_1 = 40$ mm in a single-borehole whose diameter is $R_3 = 50$ mm. Oil-based mud is used as a borehole fluid in practice. The dielectric properties of the oil-based mud depend on the brine volumetric fraction and weighting material volumetric fraction, and its complex permittivity changes over a wide range (Jannin et al., 2014). In the application of dielectric logging, drilling mud with a smaller loss factor increases the depth of penetration of the tool. Therefore, we set the oil-based mud at $\epsilon^* = 3 + 0.05j$ in all the following calculation models.

The antenna's directivity assembling in the tool was studied at its operation frequency band. The simulated directional patterns at 1, 1.5 and 2 GHz were selected as examples as shown in Fig. 3. The coordinate axis is the same as that shown in Fig. 1(a) and the Phi and Theta of polar coordinate system in Fig. 3(d) are also shown in Fig. 1(a). From patterns in Fig. 3, it can be observed that the proposed antenna launches EM energy unidirectionally towards the receiving antenna, and its directivity remains roughly the same among the broadband. The unsymmetrical reflecting shield shown in Fig. 1(a) was designed to obtain unidirectional radiation. Fig. 3(d) shows the contour map at 1.7 GHz, which was the center frequency of the operation band, and the radiation pattern is bilaterally symmetrical about the xz-plane. Strong unidirectionality allows the antenna to have a good focusing ability.

3. Results and analysis

3.1. Dielectric tool with metal collar

The transmitter and receiver are mounted on the drilling collar, and excitation signals are fed into the transmitter by coaxial line with impedance of 50 Ω . When the pulse reaches the transmitter, it generates EM wave propagating out of the slot antenna. EM energy going through

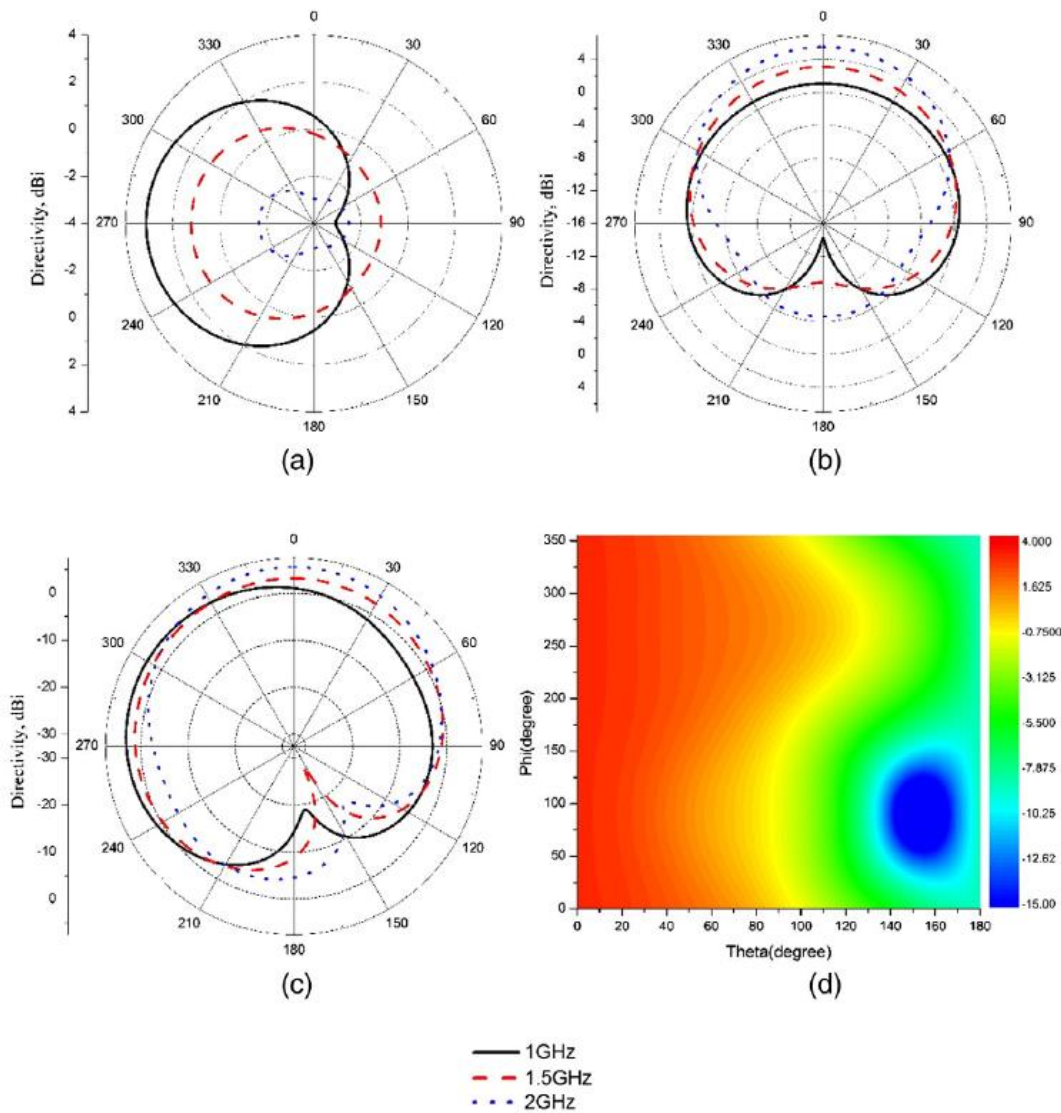


Fig. 3. Radiation pattern of the antenna mounted in the tool: (a) xy-plane at 1, 1.5, and 2 GHz; (b) xz-plane at 1, 1.5, and 2 GHz; (c) yz-plane at 1, 1.5, and 2 GHz; and (d) contour map at 1.7 GHz.

the formation and borehole, and then into the receiver generates the response voltage, which will be transferred and analyzed at the ground surface. Consequently, electric and magnetic properties of the media between the two antennas will significantly influence the final inversion results. Since the main purpose of this tool is to evaluate fluid saturation of the formation outside of the borehole, microwaves should penetrate the bore wall, so that the focus zone is in the media outside of the borehole rather than inside the borehole. Therefore, EM energy distribution around the tool is significant for the tool's performance. In previous designs such as the EPT and dielectric scanner, there are metal drilling collars between the transmitter and receiver. So the electromagnetic field distribution in circumstance of a metal cylinder between the two antennas was first studied.

The FDTD method was implemented to find the EM field around the borehole. The model used for the FDTD simulation is pictured in Fig. 4. Parts of this model are the same as shown in Fig. 2 except for the material of the cylinder between the two antennas. The transmitter and

receiver are connected by a copper drilling collar with an outer diameter $R_2 = 46$ mm and inner diameter $R_1 = 40$ mm rather than a PVC cylinder. This model is used to find the EM energy distribution around

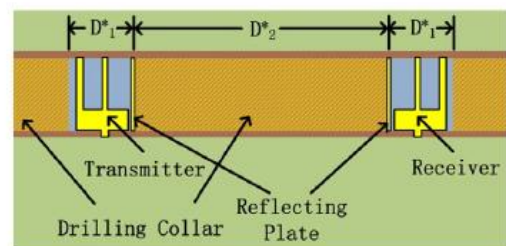


Fig. 4. Model used for the FDTD simulations to find the EM energy distribution around the conventional dielectric tool.

conventional dielectric tools. The whole simulation area was $2\text{ m} \times 2\text{ m} \times 2\text{ m}$, and the boundary conditions were set as a perfect matched layer (PML).

Complex permittivity of fluid saturated formation is a primarily function of the fluid filling the matrix pores. Many mixing laws have been proposed to deduce the effective permittivity from the volumetric fraction of the matrix and pore fluid. The generalized refractive mixing dielectric model (GRMDM) proved to be practical against experimental data over a wide frequency range from 300 kHz to 3 GHz (Mironov et al., 2004). It is presented as:

$$\sqrt{\epsilon_{\text{for}}} = \begin{cases} \sqrt{\epsilon_d} + (\sqrt{\epsilon_b} - 1)W, & W \leq W_t \\ \sqrt{\epsilon_d} + (\sqrt{\epsilon_b} - 1)W_t + (\sqrt{\epsilon_f} - 1)(W - W_t), & W \geq W_t \end{cases} \quad (1)$$

where $\epsilon_{\text{formation}}$, ϵ_d , ϵ_b , and ϵ_f refer to the complex permittivity of the formation, dry matrix, bound fluid, and free fluid, respectively. W and W_t are the saturation and maximum bound fluid fraction. Sand formations with different water/oil saturations were selected as samples in the following numerical simulation, and the corresponding complex permittivities are shown in Fig. 5.

The EM energy that exists around the logging tool can be divided into two parts: the radiating part and non-radiating part (Chew and Gianzero, 1981). Actually, a lateral wave penetrating the bore wall constitutes the radiating part. In order to estimate the dielectric properties of a formation outside the borehole, it is important to efficiently launch a lateral wave (Wait, 1987). Since the lateral wave propagates outside the borehole, this wave attains much information on the dielectric properties of the formation. On the contrary, the non-radiating part is the EM wave which is constrained around the collar and does not laterally propagate inside the formation. In order to optimize the tool design, the non-radiating part of wave should be minimized, so that the energy portion of the lateral wave is maximized. The electric field intensity in the model with the traditional dielectric tool is obtained by the FDTD method. These set of simulations for an oil-based mud filled borehole and sand formations containing four different fluid saturations: 30% water, 20% water, 10% water, and 30% oil were studied. A modulated Gaussian pulse was the monocycle impulse of the transmitting antenna. The waveform and spectrum of the Gaussian pulse are plotted in Fig. 6(a) and (b). The peak-to-peak width of the pulse was about 250 ps, and the center frequency was 1.6 GHz. The frequency bandwidth of the impulse covered the sensitive range of the complex permittivity.

The complex permittivity of the four formations is shown in Fig. 5. The velocity of the plane wave is in inverse proportional to the permittivity of the media. To avoid confusion, the E-field intensities of different models are shown when the wave spreads to the same position. Consequently, the field distributions are presented at different times in Fig. 7. In the four models, there is a high-amplitude wave around the borehole, which is called the non-radiating wave, because the distribution range of this wave is restricted along the borehole, and does not radiate into the formation. The non-radiating wave is confined to the formation adjoining the borehole up to a radial distance of several centimeters, and no obvious attenuation is observed in the direction along the drilling collar. Beyond this area, lateral waves propagate outward from the transmitter, whose velocity equals the velocity of the plane wave in each formation. Of the two parts of the electric field that are apparent in Fig. 7, the major part of energy detected by the receiver is from non-radiating wave. In this way, the detection area of the tool is restricted to the zone very close to the borehole, and thus the traditional dielectric tool's ability to evaluate dielectric properties is critically limited.

3.2. EM energy distribution around the collar

To optimize the dielectric tool design, it is important to increase the efficiency of lateral wave launching, in other words, to eliminate the non-radiating wave. In the water filled borehole, a guided wave propagates along the borehole, and is the main part of the non-radiating wave (Ellefesen et al., 2004). However, in recent applications of dielectric logging, borehole water was replaced by the oil-based mud (Guo and Liu, 2010). Theoretical analysis can help to explain the generation of the non-radiating wave. For theoretical calculation, a simplified model pictured in Fig. 8 is applied; region 1 refers to the copper metal collar with conductivity $\sigma = 6e + 7\text{ S/m}$, region 2 refers to the borehole filled with oil-based mud with permittivity $\epsilon^* = 3 + 0.05j$, and region 3 refers to the formation surrounding the borehole, with its permittivity shown in Fig. 5. The diameters of regions 1 and 2 are $R_2 = 46\text{ mm}$ and $R_3 = 50\text{ mm}$, respectively.

The refractive index of region 2 is much smaller than that of region 3. The thickness of region 2 is only 4 mm, while the wavelength in the operating band as shown in Fig. 6 is between 12 mm and 60 mm. The thickness of region 2 is one order smaller than the wavelength. The wave guide condition cannot be reached in the described model. Even though a guided wave is occasionally excited, it will radiate EM

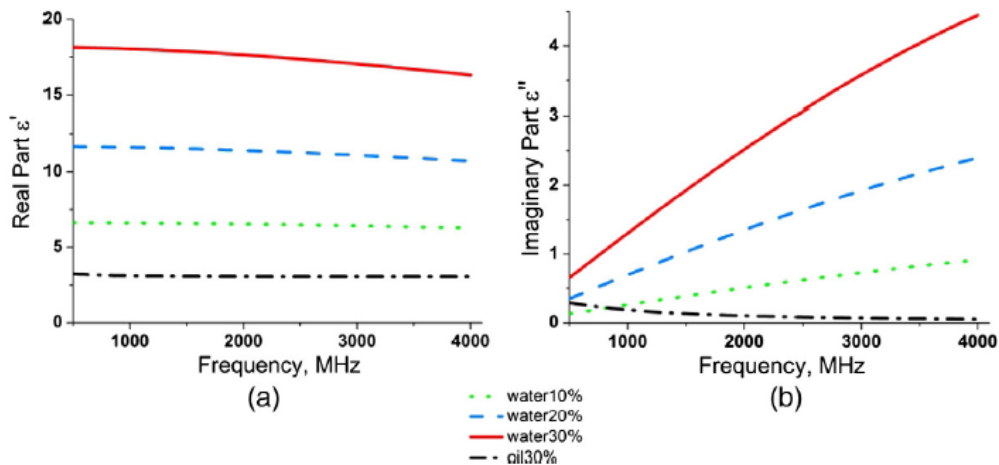


Fig. 5. Complex permittivity of formations with different fluid saturations: (a) Real part ϵ' and (b) imaginary part ϵ'' .

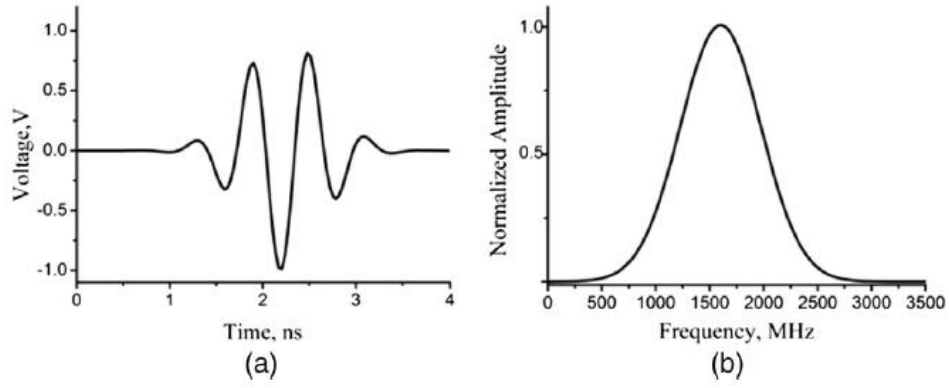


Fig. 6. The source impulse applied to the transmitting antenna: (a) time-domain waveform and (b) spectrum of the excitation signal.

energy into the formation, causing the amplitude of the guided wave to dramatically decrease. So a guided wave can hardly exist in this model.

The collar operating in the formation can be approximated as an infinitely long cylindrical conductor of circular cross-section embedded in an infinite homogeneous dielectric media. The particular solution of this boundary condition describes a radially symmetric transverse magnetic wave traveling along the cylinder (Barlow and Cullen, 1953). The field components of the symmetric wave traveling in the space inside the

conductor can be written in the form (the subscript c refers to the area inside the conductor):

$$\begin{aligned} E_{rc} &= jA \frac{k_z}{k_T} J_1(k_{Tc}r) e^{j(\omega t - k_z z)} \\ E_{zc} &= A J_0(k_{Tc}r) e^{j(\omega t - k_z z)} \\ E_{\varphi c} &= jA \frac{k_c}{k_T \omega \mu_c} J_1(k_{Tc}r) e^{j(\omega t - k_z z)}. \end{aligned} \quad (2)$$

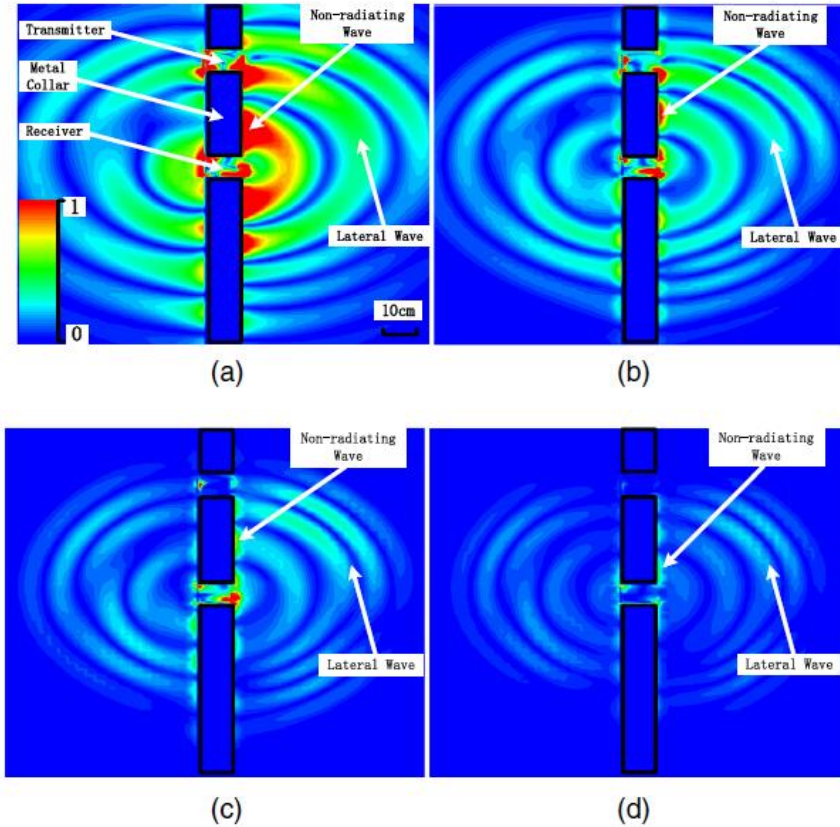


Fig. 7. Normalized electric field intensity in a sandy formation with different fluid saturations when the traditional dielectric tool operates in: (a) 3.4 ns with 30% oil, (b) 3.6 ns with 10% water, (c) 3.8 ns with 20% water, and (d) 4.2 ns with 30% water.

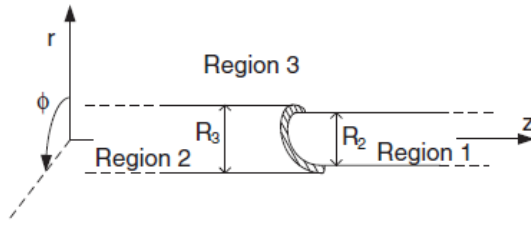


Fig. 8. Model used for theoretical analysis. R_2 and R_3 refer to the diameters of the metal collar and borehole. Regions 1, 2 and 3 refer to the three regions in this model: the metal collar, borehole, and formation.

The field components outside the conductor can be written in the form:

$$\begin{aligned} E_r &= jA \frac{k_z}{k_T} H_1^{(1)}(k_T r) e^{j(\omega t - k_z z)} \\ E_z &= A H_0^{(1)}(k_T r) e^{j(\omega t - k_z z)} \\ E_\phi &= jA \frac{k}{k_T \omega \mu} H_1^{(1)}(k_T r) e^{j(\omega t - k_z z)}. \end{aligned} \quad (3)$$

Fig. 9 shows the field components and defines the coordinate system. J_0 and J_1 are the Bessel functions, while $H_0^{(1)}$ and $H_1^{(1)}$ are the Hankel functions. k_c and k refer to the propagation constant of the plane wave inside and outside the conductor, k_{Tc} and k_T refer to propagation constant in transverse direction inside and outside the conductor, and k_z refers to the propagation constant in the z direction. The relationship between k_c , k , k_{Tc} , k_T and k_z is:

$$k_c^2 = k_{Tc}^2 + k_z^2; \quad k^2 = k_T^2 + k_z^2. \quad (4)$$

The E_z and H_ϕ should be continuous at the surface of the conductor, thus the relation could be obtained:

$$\mu \frac{k_T H_0^{(1)}(k_T R_2)}{k^2 H_1^{(1)}(k_T R_2)} = \mu_c \frac{k_{Tc} J_0(k_{Tc} R_2)}{k_c^2 J_1(k_{Tc} R_2)}. \quad (5)$$

By simultaneously solving Eqs. (4) and (5), k_{Tc} and k_c can be determined and consequently also k_z . However, the operation of Bessel functions is cumbersome and complicated. If the radius of the conductor is large compared with the skin depth, the Bessel functions in Eq. (5)

can be replaced by their asymptotic representations (Goubau, 1950):

$$\begin{aligned} J_0(x) &= \left(\frac{\pi}{2x}\right)^{-\frac{1}{2}} \cos\left(x - \frac{\pi}{4}\right); \\ J_1(x) &= \left(\frac{\pi}{2x}\right)^{-\frac{1}{2}} \cos\left(x - \frac{3\pi}{4}\right); \\ H_0^{(1)}(x) &= \frac{2j}{\pi} \ln(-j0.89x); \\ H_1^{(1)}(x) &= \frac{2j}{\pi}. \end{aligned} \quad (6)$$

Eq. (5) is then simplified to:

$$-\mu \frac{k_T R_2}{k^2} \ln(-j0.89 k_T R_2) = \mu_c \frac{k_{Tc}}{k_c^2} \cot\left(k_{Tc} R_2 - \frac{\pi}{4}\right). \quad (7)$$

Eqs. (4) and (7) were used for numerical evaluation of k_{Tc} , k_c and k_z . Propagation characteristic can be acquired from the propagation constant and we are concerned with the percentage of the power of surface wave which travels inside a depth ρ within the operating frequency bandwidth. The energy outside the area $r > \rho$ is:

$$N_\rho = \text{Re} \left[2\pi \int_\rho^\infty r E_r H_\phi^* dr \right]. \quad (8)$$

The total power of the surface wave is obtained by setting $\rho = R_2$. Ratio p is defined to describe the percentage of energy flow inside a certain depth ρ , and the expression is given as:

$$p = \frac{N_\rho}{N_{\text{total}}} = \frac{\text{Re} \left[2\pi \int_\rho^\infty r E_r H_\phi^* dr \right]}{\text{Re} \left[2\pi \int_{R_2}^\infty r E_r H_\phi^* dr \right]}. \quad (9)$$

Fig. 10 shows the contour map of ratio p in the area outside the metal collar within the operating frequency band. Four formations with different fluid saturations were selected as typical examples and their permittivity is shown in Fig. 5. The half power radius within the operation frequency is indicated by the dashed line in Fig. 10. The half power radius becomes smaller as the media permittivity increases, and in the four models the half power radius varies from 0.55 cm to 1.75 cm. The half power radii at center frequency 1.6 GHz in Fig. 10(a) to (d) are 0.95 cm, 0.8 cm, 0.5 cm, and 1.2 cm, respectively. The EM energy distribution in Fig. 7 shows that there is a non-radiating wave with obviously higher intensity confined in the area close to the collar. From theoretical derivation, we can deduce that the major part of the non-radiating wave exists as a surface wave conjoining the metal collar, which confirms the numerical simulation results.

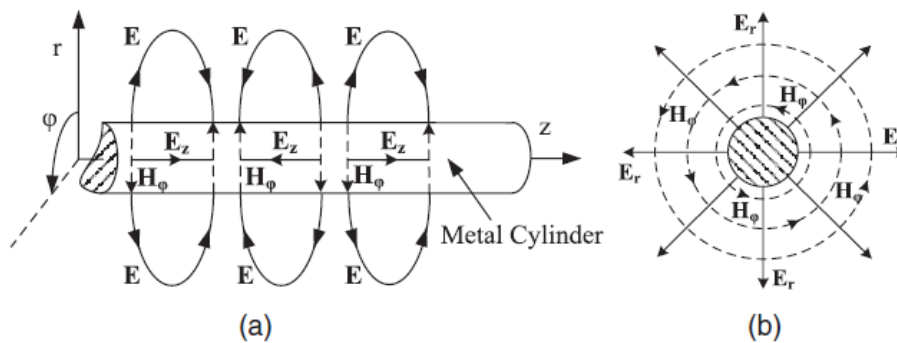


Fig. 9. The field distribution of the surface wave: (a) lateral view and (b) section view.

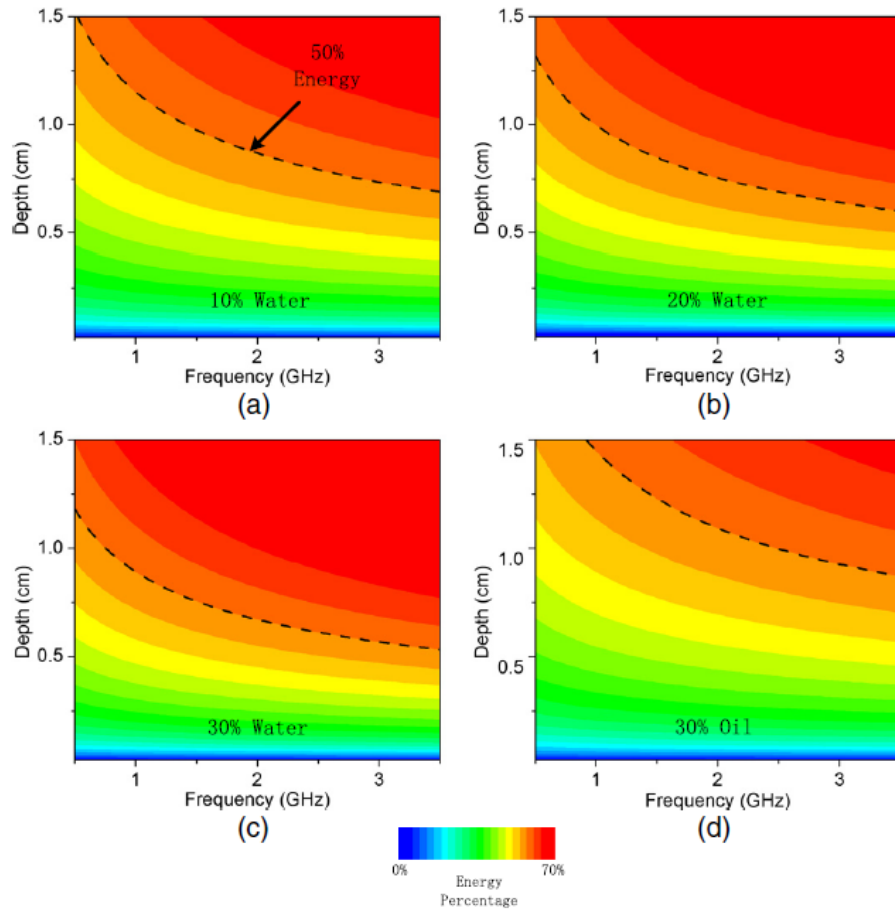


Fig. 10. Contour map of ratio ρ of surface wave: (a) sandy formation with 10% water saturation, (b) sandy formation with 20% water saturation, (c) sandy formation with 30% water saturation, and (d) sandy formation with 30% oil saturation. The color scale of the contour map covers from 0% to 70%.

This implies that about half power of the surface wave is restricted inside a cylindrical region with a radius of approximately 1 cm and a very high proportion of energy launched from the transmitter is propagated as a non-radiating wave. The surface wave causes the EM energy detected by the receiver to carry more electric information of the borehole rather than of the formation outside the borehole, and it critically decreases the detection depth of the dielectric tool.

3.3. Modified dielectric tool with PVC collar

To increase the performance of the tools, improvements are brought into the design. The most direct way to raise the efficiency of launching the lateral wave is to cut down the surface wave along the metal cylinder. For this reason, the metal drilling collar was replaced by a PVC cylinder with radius of R_2 between the two antennas as shown in Fig. 2(a) and (b). The permittivity of PVC is $2.4 + 0j$. E-field intensities around the improved tool obtained by the FDTD method are presented in Fig. 11. The model simulated here is shown in Fig. 2, the whole simulating area is $2\text{ m} \times 2\text{ m} \times 2\text{ m}$, and the boundary conditions are set as a perfect matched layer (PML). Formations with four different saturations and recording times are the same as in Fig. 7.

There is no non-radiating wave with high amplitude observed around the PVC cylinder in Fig. 11, because the structure between the two antennas cannot meet the transmission condition of any surface wave or guided wave. When metal reflecting plates are mounted on the top of the PVC cylinder, there is an EM wave inside the PVC cylinder. The structure of the tool is the same order of magnitudes as the operating wavelength, so the EM wave inside the PVC is due to diffraction, and it was observed that the relative strength of the diffracted wave decreases as the permittivity of the formation increases. In the area between the two antennas, most of the excited energy has been transferred to the lateral wave. Along the metal drilling collar beside the two antennas, there is still a noticeable surface wave in each model, but this part of the non-radiating wave cannot be detected by the receiver. In this way, the energy of the received voltage is mostly transferred from the lateral wave that propagates through the formation, and interference from the non-radiating wave is significantly diminished.

As shown in Fig. 11, propagation characteristics of the lateral wave greatly vary in the formation with different fluid saturations. The wave amplitude is bigger in the sandy formation containing 30% oil which represents the reservoir layer, than in the other three water saturated formations, the amplitude is inversely proportional to the fluid

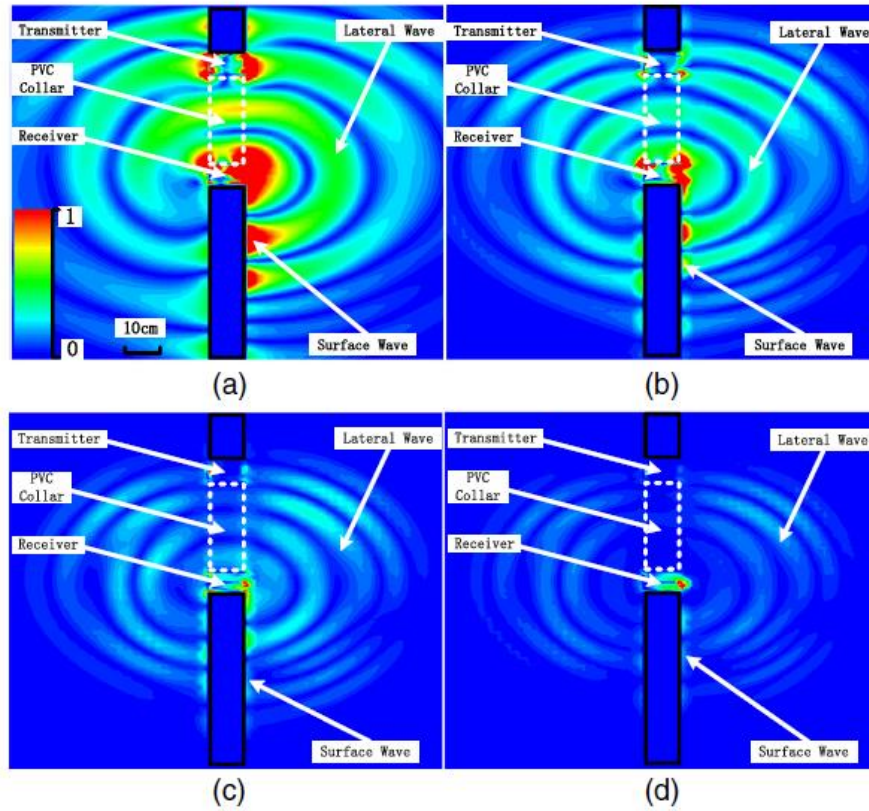


Fig. 11. Normalized electric field in sandy formation with different fluid saturations when the improved dielectric tool operates in: (a) 3.4 ns with 30% oil, (b) 3.6 ns with 10% water, (c) 3.8 ns with 20% water, and (d) 4.2 ns with 30% water.

contained in the water saturated formation, and the propagation velocity of the EM wave decreases from Fig. 11(a) to (d). These differences result from different electric properties of the formations, and certainly affect received voltages.

3.4. Analysis of received voltages

Fig. 12 presents the normalized waveform of received voltages in the four sample formations. Time begins with the triggering of the impulse

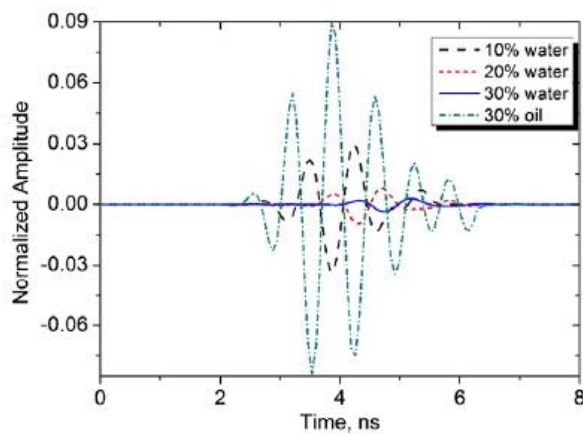


Fig. 12. The response signals in the time domain obtained from the receiver, when the system operates in formations with different fluid saturations.

signal in the transmitting antenna, and the time of the EM wave propagation to the receiver varies with fluid saturation. The phase velocity of a plane wave in homogenous media is $v_0/\sqrt{\epsilon\mu}$, and the propagation time t_{po} is in direct proportion to $\sqrt{\epsilon\mu}$. The permittivity of a formation with 30% oil saturated is the smallest in the four formations, and the EM wave in this media has the shortest t_{po} . Propagation time t_{po} in a water containing formation increases as water saturation increases. As shown in Fig. 5, the imaginary part of complex permittivity becomes bigger as water saturation increases, and the imaginary part of an oil saturated formation is quite close to zero. The imaginary part of complex permittivity represents a dielectric loss, and it can be reflected in the received voltages as shown in Fig. 12. The dielectric loss in the oil containing formation is the smallest, so received voltages have the biggest amplitude, while an obvious attenuation of the amplitude can be found in water containing formations, and the amplitude gradually decreases as the dielectric loss becomes larger.

There is no evident difference between waveforms observed in the time domain in Fig. 12. Several mechanisms related to fluid molecules' polarizability affect dielectric properties of the formation, and in the frequency range from dozens of megahertz to several gigahertz, frequency-related dispersion associated with fluid saturation can be found in the complex permittivity of formations.

Operating with a Gaussian monocycle as shown in Fig. 6, received voltages in the frequency domain are presented in Fig. 13. The center frequency of the impulse signal launched from the transmitter is 1.6 GHz, and the frequency range is between 750 MHz and 2.5 GHz. The oil containing formation possesses frequency independent permittivity, so the frequency range and center of received voltage in the formation with 30% oil is the same as the impulse signal. On the contrary, the imaginary part of the water-containing samples' complex

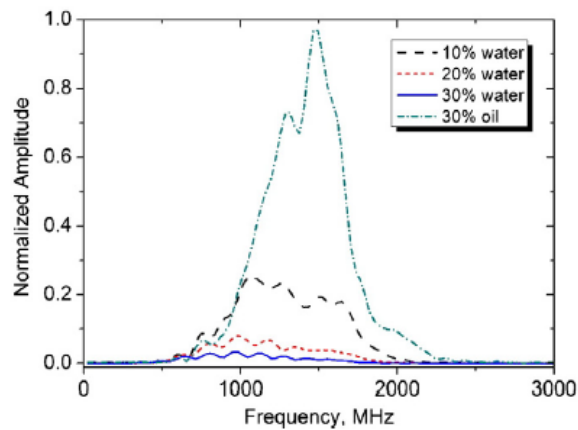


Fig. 13. The response signals in the frequency domain obtained from the receiver, when the system operates in formations with different fluid saturations.

permittivity crucially grew in a span larger than 1 GHz, and thus more excited energy is absorbed in the span above the center frequency. As shown in Fig. 13, the center frequency of received voltage shifts to lower frequency when the water saturation increases, and is the same in the time domain, with a higher water saturation causing a smaller amplitude.

Simulation results in this section demonstrate that the improved dielectric is efficient to launch the lateral wave, and the detection depth is significantly increased. Apparent propagation time t_{po} can help to evaluate the dielectric constant, and at the same time, analysis of the frequency domain provides continuously satisfactory dispersion information of permittivity in a fairly broad band. Studying combinations of received voltages in both the time domain and frequency domain makes it possible to obtain dielectric dispersive characteristics in a continuous wide-band, which has significant importance to determine fluid saturation in reservoir layers.

4. Conclusion

A dielectric logging tool designed for formation fluid saturation operating with UWB pulse propagation was presented in this paper. A monopole antenna was used as the dielectric tool, whose work band covers the frequency band of an operation pulse from 750 MHz to 2.5 GHz. Numerical simulation and theoretical analysis were used to study the EM energy distribution around the tool, which was proved

to depend upon the material of the cylinder between the receiver and transmitter. After emission from the transmitter, a lot of energy propagated along the metal drilling collar as a surface wave, which caused the amplitude of the lateral wave, which carries dielectric information out of the borehole, to decrease. The surface wave was cut off and the lateral wave launching efficiency was evaluated by replacing the cylinder material with PVC. Response voltages in the time domain could clearly evaluate the dielectric constant of the formation. From the response spectrum, dielectric dispersive characteristics in a continuous wide-band which are significant to study formation fluid saturation could be obtained. When compared with the conventional dielectric logging tools, more excited energy was transferred to the lateral wave, and measurement of the complex permittivity in a continuous wideband spectrum provided more accurate fluid saturation evaluation around the borehole.

Acknowledgment

Thanks to Dr. Edward C. Mignot, Shandong University, for linguistic advice.

References

- Barlow, H., Cullen, A., 1953. Surface waves. *Proceedings of the IEE-Part III: Radio and Communication Engineering* 100 pp. 329–341.
- Chew, W.C., Gianzero, S.C., 1981. Theoretical investigation of the electromagnetic wave propagation tool. *IEEE Trans. Geosci. Remote Sens.* 1–7.
- Ellefson, K.J., Abraham, J.D., Wright, D.L., Mazzella, A.T., 2004. Numerical study of electromagnetic waves generated by a prototype dielectric logging tool. *Geophysics* 69, 64–77.
- Goubau, G., 1950. Surface waves and their application to transmission lines. *J. Appl. Phys.* 21, 1119–1128.
- Guo, C., Liu, R.C., 2010. A borehole imaging method using electromagnetic short pulse in oil-based mud. *IEEE Geosci. Remote Sens. Lett.* 7, 856–860.
- Hizem, M., Budan, H., Deville, B., Faivre, O., Mosse, L., Simon, M., 2008. Dielectric dispersion: a new wireline petrophysical measurement. *SPE Annual Technical Conference and Exhibition*.
- Jannin, G., Kefi, S., Legendre, F., 2014. Dielectric properties of nonaqueous drilling fluids from 1 MHz up to 20 GHz. *IEEE Trans. Dielectr. Electr. Insul.* 21, 217–224.
- Li, Y.-T., Yang, X.-L., Li, Z.-B., Wang, L., Yang, H.-C., 2011. A unidirectional cylindrical conformal monopole antenna designed for impulse radar system. *IEEE Antennas Wirel. Propag. Lett.* 10, 1397–1400.
- Little, J., Julander, D., Knauer, L., Aultman, J., Hemingway, J., 2010. Dielectric dispersion measurements in California heavy oil reservoirs. *SPWLA 51st Annual Logging Symposium. Society of Petrophysicists and Well-Log Analysts*.
- Mironov, V.L., Dobson, M.C., Kaupp, V.H., Komarov, S.A., Kleshchenko, V.N., 2004. Generalized refractive mixing dielectric model for moist soils. *IEEE Trans. Geosci. Remote Sens.* 42, 773–785.
- Von Hippel, A.R., 1954. *Dielectric Materials and Applications*. Artech House, New York.
- Wait, J.R., 1987. General solution for excitation by slotted aperture source in conducting cylinder with concentric layering. *IEEE Trans. Microwave Theory Tech.* 35, 321–325.

含天然气水合物多孔介质电参数测量 系统的仿真实验研究

王 斌, 邢兰昌

(中国石油大学(华东)信息与控制工程学院, 山东 青岛 266580)

摘 要: 以天然气水合物在多孔介质中生成、分解过程的科研项目为背景, 将含水合物介质电参数测量系统部分研究内容引入实验教学, 设计了基于有限元数值法的含水合物多孔介质电参数测量仿真实验。基于反应釜及复电阻率测量装置建立数值模型; 采用全波有限元方法对模型中的电磁场进行仿真计算并获得空间电磁分量分布; 通过设置不同尺寸的水合物, 结合仿真结果后处理, 得到不同水合物分布对应的视电学参数。

关键词: 教学实验; 天然气水合物; 电磁仿真

中图分类号: P744.4; TM930 **文献标识码:** A **文章编号:** 1002-4956(2018)08-0139-05

Research on simulation experiment of electrical parameter measurement system for porous media containing natural gas hydrate

Wang Bin, Xing Lanchang

(College of Information and Control Engineering, China University of Petroleum, Qingdao 266580, China)

Abstract: In the background of the scientific research project on the gas hydrate formation and decomposition in porous media, some research content of the electrical parameter measurement system for hydrates medium is introduced to the experimental teaching, and a simulation experiment for electrical parameter measurement of the hydrated porous media based on finite element numerical method is designed. Based on the reaction kettle and complex resistivity measuring device, a numerical model is set up. The simulation calculation on the electromagnetic field in the model by using the full wave finite element method is carried out, and the distribution of space electromagnetic components is obtained. By setting different sizes of hydrates and in combination with simulation results after processing, the apparent parameters corresponding to different hydrate distributions are obtained.

Key words: teaching experiment; natural gas hydrate; electromagnetic simulation

项目驱动教学模式是研究型大学专业课程教学改革的重要内容之一, 紧跟学科前沿的研究是高质量教学的有力保证^[1-2]。在测控技术与仪器专业课程中, 电

法测量占有重要地位, 其内容既与传感器、电磁场等基础理论相关, 又与工程实践密切联系^[3]。近年来, 电法测量快速发展, 出现很多新理论、新技术, 测量系统设计和分析方法也发生了重大变化。让学生参加实际工程实践, 对于培养学生创新能力具有重要作用。

能源储层的探测技术一直是多学科交叉领域的研究热点^[4]。天然气水合物分布广、储量极其丰富, 是一种新型的非常规能源, 其物理性质和勘探方法已成为近年来国际科学界研究的热点。电法测井是评价天然气水合物储量的有效手段^[5-6]。本文依据中国石油大学(华东)测控技术与仪器专业的特色, 以提升学生对本专业的兴趣、扩展学生的学术视野、促进学生主动学习为目标, 将科研项目中的含水合物多孔介质电参数

收稿日期: 2018-02-09

基金项目: 国家自然科学基金项目(41704124); 山东省自然科学基金项目(ZR2017BEE026); 中国石油科技创新基金项目(2018D-5007-0214); 山东省重点研发计划项目(2018GGX101020, 2017GGX40109); 中央高校基本科研业务费专项资金项目(18CX02112A, 16CX05021A); 中国石油大学(华东)教改项目(QN201813, QN201516)

作者简介: 王斌(1988—), 男, 山东潍坊, 博士, 讲师, 研究方向为介电常数检测方法、电磁波介电测井、天然气水合物参数检测技术。

E-mail: wangbin2015@upc.edu.cn

测量系统研究内容引入本科专业课程改革中来,让学生有机会接触实际工程问题和学科前沿,指导学生完成仿真、数据分析等工作,取得了良好的教学效果。

1 含水合物多孔介质电参数测量系统原理

天然气水合物广泛存在于海底沉积物中,含天然气水合物的沉积物电参数特性异于传统油气储层。在实验室中用天然海砂作为多孔介质来模拟海底沉积物,开展水合物在海砂中的生成分解过程研究,同时对含水合物海砂的电参数进行检测,通过数据处理获得电参数变化与海砂中水合物含量之间的关系,为电法测井勘探天然气水合物提供理论依据。

含水合物多孔介质电参数测量系统由高压反应釜、电极传感器、信号调理电路、信号发生器、数据采集器、支架等组成(见图1),反应釜内壁衬绝缘耐腐蚀聚四氟乙烯涂层。通过升压、降温达到天然气水合物生成条件,水合物在反应釜内生成。16个电极传感器分2层安装于反应釜壁,电极与釜内被测物直接接触。当某个电极作为发射电极时,其他15个电极依次工作在接收状态,与发射电极、被测介质构成导电回路。发射电极的交流电压始终恒定,通过测量接收电极处的电流强度,能够直接得到回路的阻抗值。经过后处理得到视电导率和视介电常数^[7-8]。

通过在极低频至高频频段进行各回路的电参数测量,可获得反应釜内水合物的实时分布情况。实验中,电极响应直接决定了得到的电参数,而水合物及其空间分布是影响电极响应的重要因素,故建立电极响应与水合物空间分布的关系成为研究中的必要环节。由于电磁波、声波等均无法穿透金属反应釜壁,因而借助传统成像方法获取水合物空间分布十分困难,且实验中水合物空间分布不可控、实验周期长、成本也较高。因此,开展以计算电磁学为技术手段的仿真实验,是探索电极响应随水合物空间分布变化规律的有效方法。

2 基于有限元的电参数测量仿真

有限元方法是目前电磁数值仿真的常用的方法,且计算结果可靠^[9-10],成熟的商业软件较多。本文中有限元法采用的四面体网格有益于剖分电极、水合物等精细结构,结合高性能计算平台,可对电磁波在非均匀介质中的传播、散射问题进行精确模拟,非常适合含天然气水合物多孔介质电参数测量系统的仿真研究^[11-12]。图2所示为含水合物多孔介质电参数测量系统仿真实验流程图。该仿真实验可以帮助学生认识有限元电磁仿真方法,并利用有限元方法解决电磁场数值问题。



图1 含水合物多孔介质电参数测量系统

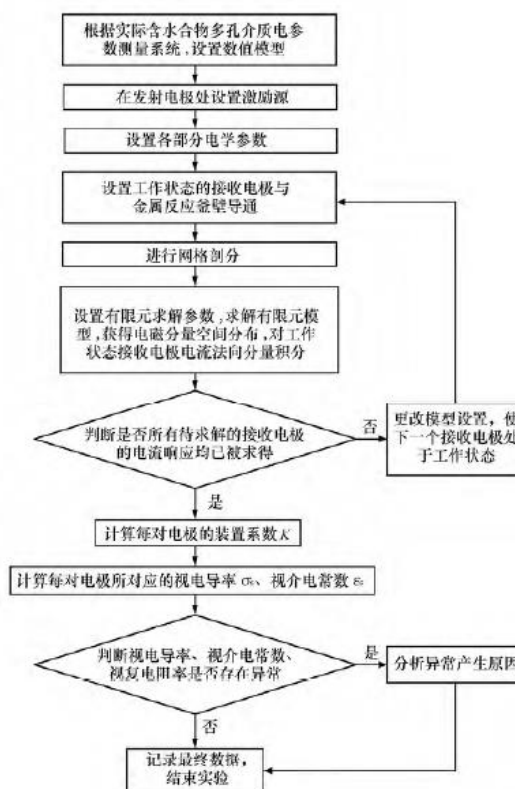


图2 含水合物多孔介质电参数测量系统仿真实验流程图

2.1 电参数测量系统数值模型

含水合物多孔介质电参数测量系统数值模型见图3。16个电极分2层均匀安装于反应釜壁内的绝缘层中,在反应釜壁与发射电极间设置恒定的电压源。电

流通过发射电极注入反应釜内的被测介质中,其余 15 只电极作为接收电极。当接收电极处于工作状态时与反应釜壁导通,此时接收电极和电压源共地,且不超过 1 只接收电极同时处于工作状态。

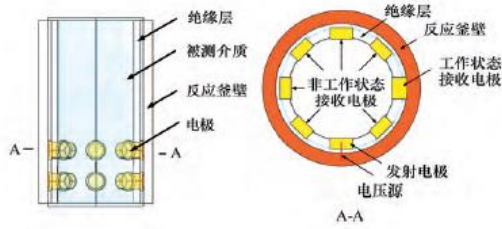


图3 含水合物多孔介质电参数测量系统模型

2.2 仿真模型参数设置

含天然气水合物多孔介质电参数测量系统的仿真,参数设置主要包括:

(1) 模型中的反应釜、电极等金属部件设置为电导率无穷大的完美导体(PEC),以提高仿真效率。

(2) 设置水合物相对介电常数为 3,电阻率无穷大的无耗电介质。

(3) 设置反应釜内孔隙度 30%、含水饱和度 40% 海砂的电参数,由数字岩心实验结合阿奇公式计算得到,电导率为 0.275 5 S/m,相对介电常数为 41^[13]。

(4) 仿真区域外边界为反应釜外壁,背景材料相对介电常数设为 1,空气的电导率 0 S/m。

(5) 激励源为单一频率电压源,电压均方根值设为 100 V,两端分别与发射电极、反应釜壁相连接。

(6) 电磁场被约束在金属反应釜壁内区域,仿真区域外边界设置为电壁。

(7) 为得到足够高的仿真精度和仿真效率,选择二阶四面体网格对测量系统模型进行空间离散;将网格区域划分为反应釜、电极、含水海砂、天然气水合物几部分。因天然气水合物、电极的结构较为复杂,需根据具体尺寸单独加密,其他部分四面体网格边长为仿真最小波长的 1/5。本文中模型的四面体网格数约 70~100 万个,网格质量平均值大于 0.8。

(8) 利用频域全波有限元法进行仿真求解,求解精度设置为 1E-6,依次对 0.01 Hz、0.1 Hz、1 Hz、10 Hz、100 Hz、1 kHz、10 kHz、100 kHz、1 MHz、10 MHz 频率进行求解。

3 仿真结果及分析

由于电极材料设定为电导率无穷大的完美导体,所以在靠近电极处被测介质中的电流方向垂直于电极表面,对工作状态下接收电极与被测介质接触面

处电流垂直分量积分,即为该工作状态电极的电流响应。

3.1 界面对视电学参数的影响分析

在反应釜内天然气水合物的生成过程中,含水海砂与天然气水合物之间有大量界面存在,在反演水合物生成状态时,需要考虑界面对电参数的影响。为研究界面对反演得到视电学参数的影响,首先在测量系统模型基础上分别建立如图 4 所示界面水平和倾斜的被测介质模型。水合物处于界面下方,水平界面位于两层电极中间,倾斜界面与水平夹角 30°,发射电极与含水海砂接触,且倾斜界面关于电压源所在垂直截面对称。

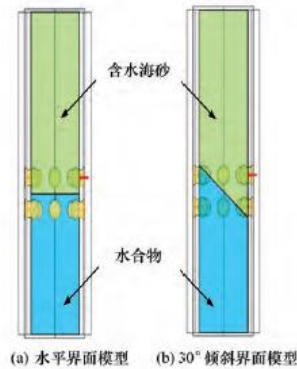


图4 存在水合物与含水海砂界面的模型示意图

完成模型的建立、仿真后,获得各个接收电极工作状态的传导电流响应 I_{cond} 和位移电流响应 I_{displ} ,其中传导电流响应 I_{cond} 与电压同相,位移电流响应 I_{displ} 与电压正交。利用公式(1)、(2)计算各接收电极对应的视电导率及视介电常数^[14]:

$$\sigma_s = \frac{I_{cond}}{K_1 U_{TR}} \quad (1)$$

$$\epsilon_s = \frac{I_{displ}}{\omega K_2 U_{TR}} \quad (2)$$

其中 K_1 、 K_2 为装置系数,可通过理论计算或实验测得, U_{TR} 是 100 V 源电压,计算得到视电导率 σ_s 及视介电常数 ϵ_s 见图 5(由于界面关于电压源所在垂直截面对称,只需列出上层 45°、90°、135°、180°、下层 0°、45°、90°、135°、180° 电极处视电学参数)。可以看出:

(1) 视电导率与模型实际设置具有很好的一致性。当电流回路被水合物完全阻断时,视电导率下降为 0;未被水合物阻断时,视电导率为 0.25~0.3 S/m,与含水多孔介质电导率 0.275 5 S/m 基本相符,且视电导率随回路被水合物阻断程度增加而逐渐减小。

(2) 当频率高于 100 Hz 时,视介电常数主要由空间位移电流决定,数值分布在 10~100 之间,介于水合

物与含水海砂介电常数之间。

(3) 频率低于 100 Hz 时, 视介电常数频散现象非常明显, 且随着频率降低, 视介电常数呈指数升高, 尤

其在频率范围低于 1 Hz 时, 视介电常数异常大, 且受电极位置、界面位置影响显著。

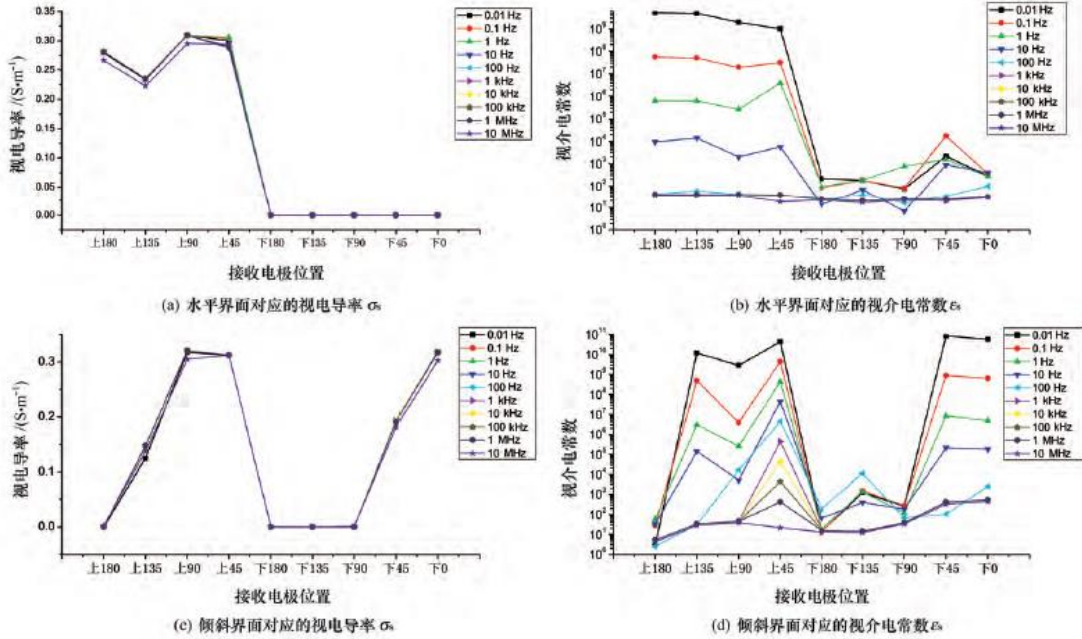


图5 不同界面对应各接收电极处的视电学参数响应

理论上, 固定含水饱和度的多孔介质、纯净天然气水合物等均匀介质的介电常数, 在 100 Hz 以下低频范围内转向极化、电子极化、离子极化对介电常数的影响几乎可以忽略, 故介电常数都应趋于固定值, 而通过介质的电流密度总量 J_{total} 可表示为式(3):

$$J_{total} = (\sigma + i\omega\epsilon)E = J_{cond} + iJ_{displ} \quad (3)$$

σ 、 ϵ 分别为介质的电导率和介电常数, J_{cond} 、 J_{displ} 分别为传导电流密度和位移电流密度。此时位移电流密度 $J_{displ} = \omega \cdot \epsilon \cdot E$ 与角频率 ω 呈正比关系, 接收电极响应电流的位移电流部分 I_{displ} 也应与角频率 ω 呈正比关系。为研究频率低于 1 Hz 时界面周围出现视介电常数异常增高现象的机理, 在孔隙度 30%、含水饱和度 40% 的含水海砂中设置厚度 L 不同的层状水合物, 水合物层中心间隔 $D=5$ mm, 水平分布于含水海砂中 (见图 6)^[7-8]。考察水合物层厚度对下层 180° 处接收电极电流响应、视电导率、视介电常数的影响。

图 7 所示是不同水合物层厚度 (0.5~9.5 mm、均匀的孔隙度 30%、含水饱和度 40% 海砂作为参考), 同相接收电流、正交接收电流、视电导率、视介电常数与频率的关系。

图 7(a) 为同相接收电流强度与频率的关系。当频率高于 100 Hz 低于 1 MHz 时, 传导电流基本不随

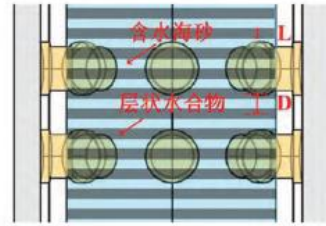


图6 含水海砂中生成层状水合物的数值模型

频率变化; 高于 1 MHz 时存在趋肤效应, 传导电流强度减弱; 低于 10 Hz 时, 4 mm、5 mm、6 mm、7 mm、8 mm、9 mm 厚度的层状水合物对应传导电流强度不随频率变化, 0.5 mm、1 mm、2 mm、3 mm、9.5 mm 厚度层状水合物对应传导电流随频率降低增大显著; 且在 0.5~3 mm 厚度范围内, 同相电流强度随水合物层厚度减小而增强。

图 7(b) 为接收电流强度正交部分与频率的关系。当频率高于 10 kHz 时, 位移电流密度与相对介电常数成正比, 水合物介电常数较含水海砂要低, 故正交电流强度随水合物层厚度增加而减弱; 由于实际介电常数在高于 10 kHz 时变化很小, 故在此范围内, 正交电流强度与频率成正比。当频率在低于 10 kHz 的超低

频范围,随频率降低,正交电流强度逐渐增强,水合物厚度小于 5 mm 时,正交电流随厚度增加而减弱;当厚度达到 6 mm 时,正交电流强度随厚度增加振荡上升。

图 7(c)与图 7(d)分别显示了根据电流强度,利用式(1)和式(2)反演得到的视电导率 σ_s 和视介电常数 ϵ_s 。频率大于 10 Hz 时,视电导率随水合物含量增加而减小;低于 10 Hz 时,随频率的降低,0.5 mm、1 mm、2

mm、3 mm、9.5 mm 厚度的水合物层对应视电导率数值显著增大,且 0.5 mm 水合物层对应视电导率在 0.1 Hz,达到最大,其他直径未见明显异常。高于 10 kHz 时,视介电常数基本不随频率变化,且水合物含量增加视介电常数降低;频率低于 1 kHz 时,视介电常数均随频率降低而增大,不同频率下视介电常数极大值对应水合物层厚度各异。

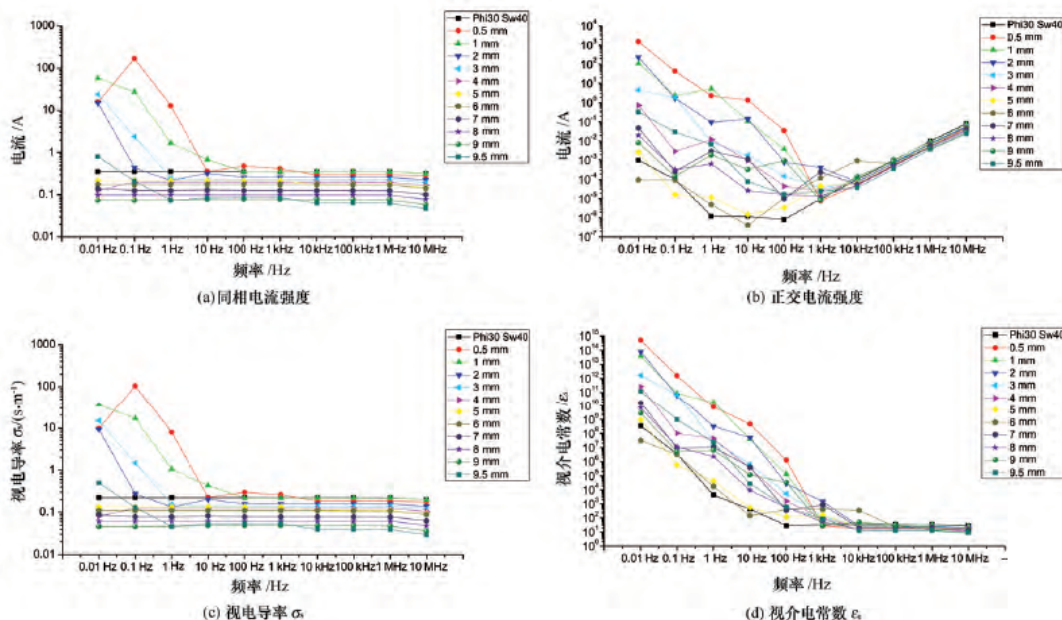


图 7 下层 180°处接收电极的视电学参数随层状分布水合物层厚度的变化

3.2 结果讨论

由图 5(b)和 5(d)仿真实验结果可见,低频视介电常数均出现异常增大,且远远高于真实介电常数(真实介电常数介于含水海砂、水合物的介电常数之间)。当频率低于 10 kHz、容器中为均一含水海砂时,视介电常数也伴随频率降低而升高,推测此时的非真实视介电常数是由金属电极附近载流子定向移动造成电极极化效应引起^[15]。在低于 10 kHz 范围的同一频率下,当有水合物与其他物质之间的界面存在时,较均一含水海砂的视介电常数出现了几个数量级的增大(个别曲线稍小),说明除电极极化效应外,不同水合物分布情况以及含量均会影响低频视介电常数,水合物与含水多孔介质间的界面极化也是视介电常数异常增大的因素之一。

当水合物层厚 0.5 mm 时,0.01 Hz~100 Hz 范围内的视介电常数较含水海砂高 $10^5 \sim 10^7$,推测是由于薄层状水合物为界面极化提供了更大的接触面积和载流子输运空间,在低频范围的传导电流弛豫增强,宏

观表现为更高的视介电常数,而并非真正的转向极化效应造成。

在完成上述建模、仿真实验、数据分析后,引导学生对视介电常数在低频所出现的异常进行讨论。通过指导学生查阅相关文献,对电磁学前沿理论进行探索学习,达到通过科研与教学相结合的方式培养学生实践、创新能力的目的。

4 结语

将含水合物多孔介质电参数测量系统研究内容引入测控技术与仪器专业的实践教学,指导学生完成了基于实验室电学参数测量装置的数值模型建立,进行了反应釜中含水合物海砂的电学测量过程的有限元仿真实验,总结了视电学参数异常的特点,最后提出了一种对实验结果的合理解释。通过一整套具体的科研实验,学生的实践和探索能力显著提高,发挥了科研项目在实践教学中的作用,教学效果很好。同时,本文的

(下转第 156 页)

合的地质实习教学模式:一是在课堂教学中,利用地质实习网络辅助系统将教学内容形象化,尤其是地质现象的三维可视化展示,可以让学生重复观察,了解地质现象的演化过程;二是在实习教学中,教师可以借助地质实习网络辅助系统,更有针对性地安排实习路线和实习内容,强调实习重点,而学生可以利用地质实习野外辅助系统强化野外地质现场实习效果。

该教学软件主要表现出以下 3 方面优点。

(1) 内外结合,丰富了学生的学习方式。在大量收集、整理野外地质教学资料的基础上,对地质现象进行数字化和编辑处理工作,采用三维全景技术、三维建模技术实现了地质实习地理环境及典型地质现象特征的仿真,将课堂教学和实习教学串联起来,使地质实习教学实现了校内、校外的有机结合。

(2) 动静结合,提升了实习的教学效果。学生借助地质实习辅助教学软件,不但可以在电脑终端查看典型地质现象的静态图片、文字说明以及构造运动过程的三维动态演示,而且可以通过手机终端进行 GPS 导航,边走边看、边学,实现了地质实习的动静结合,提升了实习效果。

(3) 虚实结合,实现了理论与实习的统一。数字化、可视化的地质实习辅助教学软件改变了传统实习教学模式单一的问题,将教师理论讲解(虚)和学生野外实习(实)有机结合,实现了理论与实习的统一。

4 结语

地质实习辅助教学软件将 WebGIS、Mobile GIS 技术应用到地质实习教学中,为学生和教师提供了不同客户端下的地质实习仿真环境,形成了虚实结合的

野外地质实习教学模式。该软件的使用提升了学生野外地质实习的趣味性和学习效果,丰富了实习基地的建设模式,较好地弥补了原来地质实习教学的一些不足。该软件作为传统教学方式的辅助手段和重要补充,其他实践性要求较强的地学科课堂教学和实习教学也可借鉴。

参考文献(References)

- [1] 欧佳斌,张新长,郭泰圣.基于移动 GIS 的规划数据应用系统研究[J].测绘通报,2014(12):89-92.
- [2] 姚纪明,刘亚静,王森.地质调查手机移动 GIS 设计与实现[J].测绘科学,2015,40(9):134-137,142.
- [3] 陈晓宁,刘金榜.移动 GIS 版地理国情外业调绘系统的设计与实现[J].地理空间信息,2016,14(6):41-44.
- [4] 张浩,肖海威,喻永平.移动 GIS 在行政区域界线勘测中的应用[J].工程勘察,2017(2):53-56.
- [5] 王崇,林玉标.基于 VR-GIS 的庐山虚拟地理实习基地创设初探[J].宿州学院学报,2008,23(2):137-139.
- [6] 邓春燕.基于 RIA 的全景虚拟野外地质信息系统[D].长春:吉林大学,2010.
- [7] 郭巍,薛林福.虚拟野外地质实习系统(VFGTS):野外地质实践教学平台[J].世界地质,2010,29(3):522-526.
- [8] 李斌,王岩松,秦奋,等.虚拟现实技术在地理野外实习中的应用[J].实验技术与管理,2011,28(8):93-95,106.
- [9] 郝伟,曹代勇,应玺.基于 Virtools 的虚拟地学认识实习系统的实现[J].中国地质教育,2011,20(2):51-54.
- [10] 祝德显.基于 Web 的虚拟野外地质实习系统设计与实现[J].内江科技,2013,34(2):96-97.
- [11] 徐春辉,于国强,张伟,等.基于 Flex 与 ArcGIS Server 的全景地质信息系统的设计与实现[J].辽东学院学报(自然科学版),2012,19(4):268-272.
- [12] 欧佳斌,张新长,郭泰圣.基于移动 GIS 的规划数据应用系统研究[J].测绘通报,2014(12):89-92.
- [13] 姚纪明,刘亚静,王森.地质调查手机移动 GIS 设计与实现[J].测绘科学,2015,40(9):134-137,142.
- [14] 陈晓宁,刘金榜.移动 GIS 版地理国情外业调绘系统的设计与实现[J].地理空间信息,2016,14(6):41-44.
- [15] 张浩,肖海威,喻永平.移动 GIS 在行政区域界线勘测中的应用[J].工程勘察,2017(2):53-56.
- [16] 王崇,林玉标.基于 VR-GIS 的庐山虚拟地理实习基地创设初探[J].宿州学院学报,2008,23(2):137-139.
- [17] 邓春燕.基于 RIA 的全景虚拟野外地质信息系统[D].长春:吉林大学,2010.
- [18] 郭巍,薛林福.虚拟野外地质实习系统(VFGTS):野外地质实践教学平台[J].世界地质,2010,29(3):522-526.
- [19] 李斌,王岩松,秦奋,等.虚拟现实技术在地理野外实习中的应用[J].实验技术与管理,2011,28(8):93-95,106.
- [20] 郝伟,曹代勇,应玺.基于 Virtools 的虚拟地学认识实习系统的实现[J].中国地质教育,2011,20(2):51-54.
- [21] 祝德显.基于 Web 的虚拟野外地质实习系统设计与实现[J].内江科技,2013,34(2):96-97.
- [22] 徐春辉,于国强,张伟,等.基于 Flex 与 ArcGIS Server 的全景地质信息系统的设计与实现[J].辽东学院学报(自然科学版),2012,19(4):268-272.

(上接第 143 页)

研究成果可以为含水合物多孔介质电参数测量提供技术参考,对科研和教学均起到了很好的促进作用。

参考文献(References)

- [1] 许迈进,杨行昌.教学与科研并重:研究型大学和谐发展战略的重要选择[J].中国高教研究,2007(4):49-51.
- [2] 周立亚,龚福忠,兰宇卫,等.构建研究型实验教学法培养学生创新能力[J].实验室研究与探索,2011,30(5):127-129.
- [3] 冯根生,冯婷,杜春荣.基于学科特点的研究型实验教学模式建设[J].实验技术与管理,2012,29(3):239-241.
- [4] 宋延杰.地球物理测井[M].北京:石油工业出版社,2011.
- [5] 王彩程,邢兰昌,陈强,等.含甲烷水合物多孔介质的复电阻率频散特性与模型[J].科学技术与工程,2017,17(18):46-54.
- [6] 宁伏龙,刘力,李实,等.天然气水合物储层测井评价及其影响因素[J].石油学报,2013,34(3):591-606.
- [7] 邢兰昌,刘昌岭,陈强,等.一种多孔介质中气水合物模拟实验测

试系统及测试方法;WO2017050142A1[P].2017.

- [8] 邢兰昌,祁雨,刘昌岭,等.电-声-热多参数联合测试系统开发[J].实验技术与管理,2017,34(11):78-85.
- [9] 倪光正,杨仕友,邱捷,等.工程电磁场数值计算[M].北京:机械工业出版社,2010.
- [10] 徐志锋,吴小平.可控源电磁三维频率域有限元模拟[J].地球物理学报,2010,53(8):1931-1939.
- [11] 徐传进.电磁层析成像关键技术仿真研究[D].天津:天津大学,2010.
- [12] 马平,周晓宁,田沛,等.基于 COMSOL 电容层析成像[J].电测与仪表,2009,46(11):20-23.
- [13] 马龙.天然气水合物储层饱和度参数数值模拟[D].长春:吉林大学,2014.
- [14] 王斌,邢兰昌.含天然气水合物多孔介质阻抗测量装置的仿真和分析方法;201711061908.3[P].2017.
- [15] Isha P B, Talary M S, Caduff A, et al. Electrode polarization in dielectric measurements: a review[J]. Measurement Science & Technology, 2013,24(10):102001-102021.

Numerical Study on Complex Resistivity Measurement of Porous Media Containing Gas Hydrate

Bin Wang and Lanchang Xing

College of Information and Control Engineering
China University of Petroleum (East China), Qingdao, China

Abstract— Natural gas hydrate is potentially a new energy source. Most of the naturally occurring gas hydrate are present in the marine sediments. As the stability of gas hydrate in porous sediments is largely influenced by pressure, temperature and properties of the pore water, it is rather difficult to estimate its concentration. Electrical complex resistivity measurements have been used for estimating the gas hydrate saturation with the aid of Archie's method. However, the various distribution forms of gas hydrate in porous media and existence of interfaces between the hydrate and sediment particles made the imaginary part of conductivity highly sophisticated. Traditional saturation evaluation methods used for oil and water cannot be used for gas hydrate any more.

To elucidate the mechanism of hydrate saturation evaluation by complex resistivity measurement that implemented in the experimental work and to investigate the connections between gas hydrate distribution and electrode responses, simulations on the resistivity measuring equipment and porous media containing gas hydrate were carried out. Numerical models with different distribution forms (such as layer, block and vein) of gas hydrate in a reactor were constructed. The EM field inside the reactor and full current responses of electrodes were calculated by finite element method (FEM). Then the apparent conductivity σ_s and apparent permittivity ε_s were obtained for the inversion of hydrate saturation. The simulation results have shown that: firstly, there are obvious correlations between the gas hydrate distribution forms and electrode responses, from which the distribution forms can be deduced qualitatively; secondly, the current responses to the media containing gas hydrates are very similar to those containing oil at high frequency; thirdly, the imaginary part of current response for the case with gas hydrate in the form of layer, block or vein increase abnormally at extremely low frequency, and it depends on the shape and size of gas hydrate. It is postulated that the current relaxation exists at the interface between the gas hydrate and sediment particles, and it implies that induced polarization occurs in these models.

1. INTRODUCTION

Natural gas hydrates are widely distributed in marine sediment area, and their resource potential is twice the sum of known fossil fuel resources [1]. The gas hydrate related research has grown exponentially in recent years for successful exploration [2]. Geophysical well logging techniques are widely used in gas hydrate detection, therefore, many works have focused on gas hydrate saturation evaluation through electrical, acoustic and seismic methods in porous media [3]. Electrical resistivity survey data are especially sensitive to the gas hydrate content, and complex resistivity measurement has been used for estimating gas hydrate saturation [4]. Existing studies elucidated that there were many mechanisms such as induced polarization in conductive porous media at frequency from 0.01 Hz to 100 Hz [5]. In this way, current responses of the electrodes (complex current responses or described as amplitude attenuation and phase shift) always become counterintuitive when porous media contain gas hydrates.

To illustrate the connection between current responses and gas hydrate distribution, and to provide theoretical support for the synchronous laboratory experiments, numerical simulations on the resistivity measuring equipment and porous media containing gas hydrate were carried out with finite element method (FEM). Firstly, the apparent conductivity σ_s and permittivity ε_s were obtained at the operating frequencies in the experiments, when gas hydrate was synthesized in the porous medium in the reactor. Then the current responses with different gas hydrate distribution forms were investigated at frequency samples from 0.01 Hz to 10 MHz.

2. EQUIPMENT FOR COMPLEX RESISTIVITY MEASUREMENT AND NUMERICAL MODELING

The reactor for porous media containing gas hydrate and the electrodes for complex resistivity measurement are shown in Fig. 1. Electrodes are fixed on the reactor with seal flange and their

head faces contact the measured media in the reactor. The sixteen electrodes with diameter of 25 mm are mounted around the wall of the steel cylinder.



Figure 1: Pictures of the reactor for porous media containing gas hydrate and the electrodes for complex resistivity measurement.

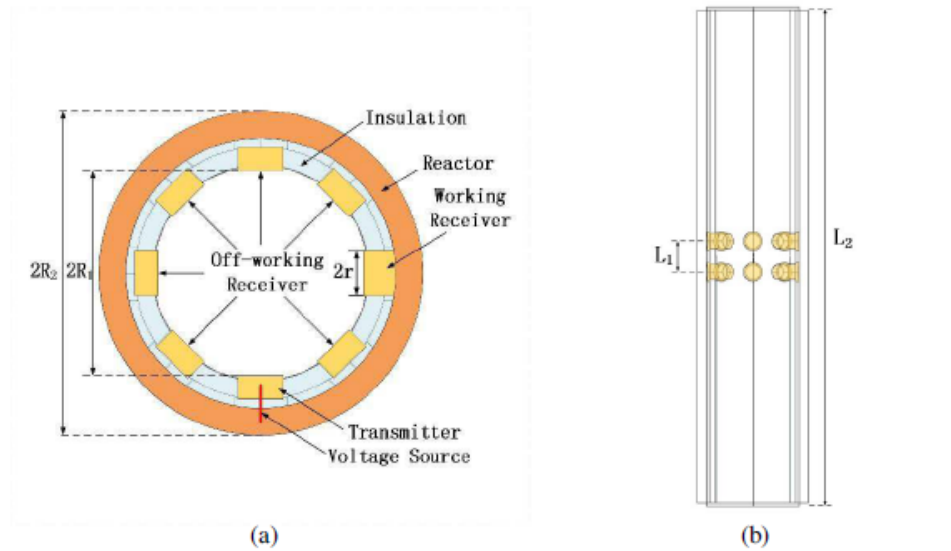


Figure 2: Schematic of the numerical models: (a) top view, (b) side view.

As shown in Fig. 2, the numerical models are built according to the experimental equipment at one-to-one scale. The outer radius of the reactor $R_2 = 90$ mm, and radius of the measured media $R_1 = 60$ mm. The height of the reactor $L_2 = 800$ mm and metallic caps are welded at its top and bottom. Isolation layer with $\epsilon = 2$ and $\sigma = 0$ S/m is mounted between the metal reactor and measured media. Electrodes inset the isolation are separated by 45 degrees horizontally, and the vertical interval between centers of each two electrodes $L_1 = 50$ mm. A voltage source with 100 V connects the transmitter electrode and reactor. The rest fifteen electrodes act as receivers. When one receiver is working, it is electrically connected to the reactor wall, and the other receivers are at off-working state. Fig. 2 shows the example that the electrode at 90 degrees angle to the transmitter acts as the working receiver. All of the metallic parts are set as perfect electrical conductor (PEC). As the EM field is shielded by the metallic reactor, the simulation is a closed region problem, and there is no special operation at the boundaries of calculated region.

3. SIMULATION RESULTS AND ANALYSIS

3.1. Apparent Conductivity and Permittivity with Gas Hydrate Generated

To investigate the variations of the apparent conductivity σ_s and permittivity ε_s during the hydrate synthesis course, two numerical models are built as shown in Fig. 3. Situations with horizontal and inclining interfaces as shown in Figs. 3(a) and (b) are simulated respectively. The transmitter electrode contacts the upside media with porosity $\Phi = 30\%$, water saturation $S_w = 40\%$. The conductivity of the upside media is 0.2755 S/m , and the dielectric permittivity is 41, which are obtained by Archie's Law [6] and GRMDM [7]. Gas hydrate synthesized at the bottom is set to be nonconducting, and the dielectric permittivity is 3.

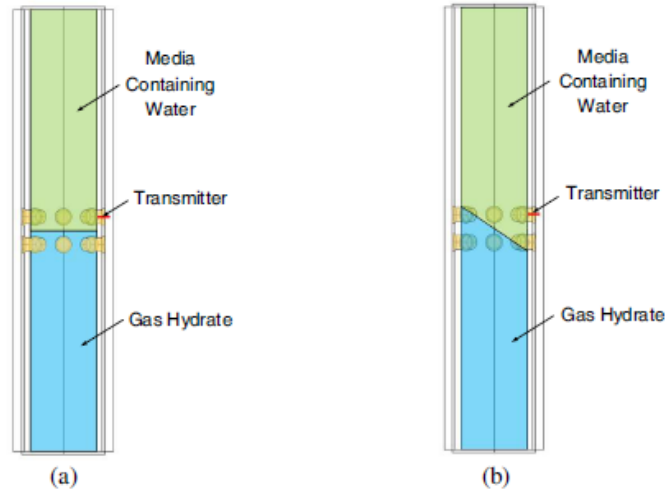


Figure 3: Numerical model with gas hydrate synthesized at the bottom of the reactor: (a) the horizontal interface between the media containing water and gas hydrate; (b) the inclining interface with an angle of 30 degrees to the horizontal between the media containing water and gas hydrate.

The conduction current I_{cond} and displacement I_{displ} current at each receiver electrode are obtained firstly. As shown in Fig. 4, the apparent conductivity σ_s and permittivity ε_s are calculated by using Equations (1) and (2). The voltage source at the transmitter electrode $U_{TR} = 100 \text{ V}$. The electrode coefficients K_1 and K_2 are determined through theoretical and experimental analysis.

$$\sigma_s = \frac{I_{cond}}{K_1 U_{TR}} \quad (1)$$

$$\varepsilon_s = \frac{I_{displ}}{\omega K_2 U_{TR}} \quad (2)$$

The apparent conductivity σ_s do not vary with frequency obviously, and have a tendency of matching the practical conductivity distribution. However, the apparent permittivity shown in Figs. 4(b) and (d) have significant dispersion with frequency below 100 Hz. As the operating frequency decreases, ε_s reaches a large value abnormally. Especially, when the frequency is below 1 Hz, the ε_s is millions time larger than the practical value. It is observed that the phenomenon becomes particularly outstanding, when there is conducting water saturated media between the transmit-receive electrodes. Furthermore, the shape of the gas hydrate has also significant influence on the apparent permittivity.

3.2. Current Responses and Gas Hydrate Distribution Forms

To identify the effects of the gas hydrate distribution, numerical models with three kinds of gas hydrate distribution forms (layer, block and vein) are constructed, and the background material is porous media containing water with porosity $\Phi = 30\%$, water saturation $S_w = 40\%$. The spatial distance between each layer/block/vein is set 10 mm congruously, and the gas hydrate layers and veins are both horizontal. The current responses varying with layer thickness are displayed in Fig. 5; the current responses varying with diameter of blocks are displayed in Fig. 6; the current

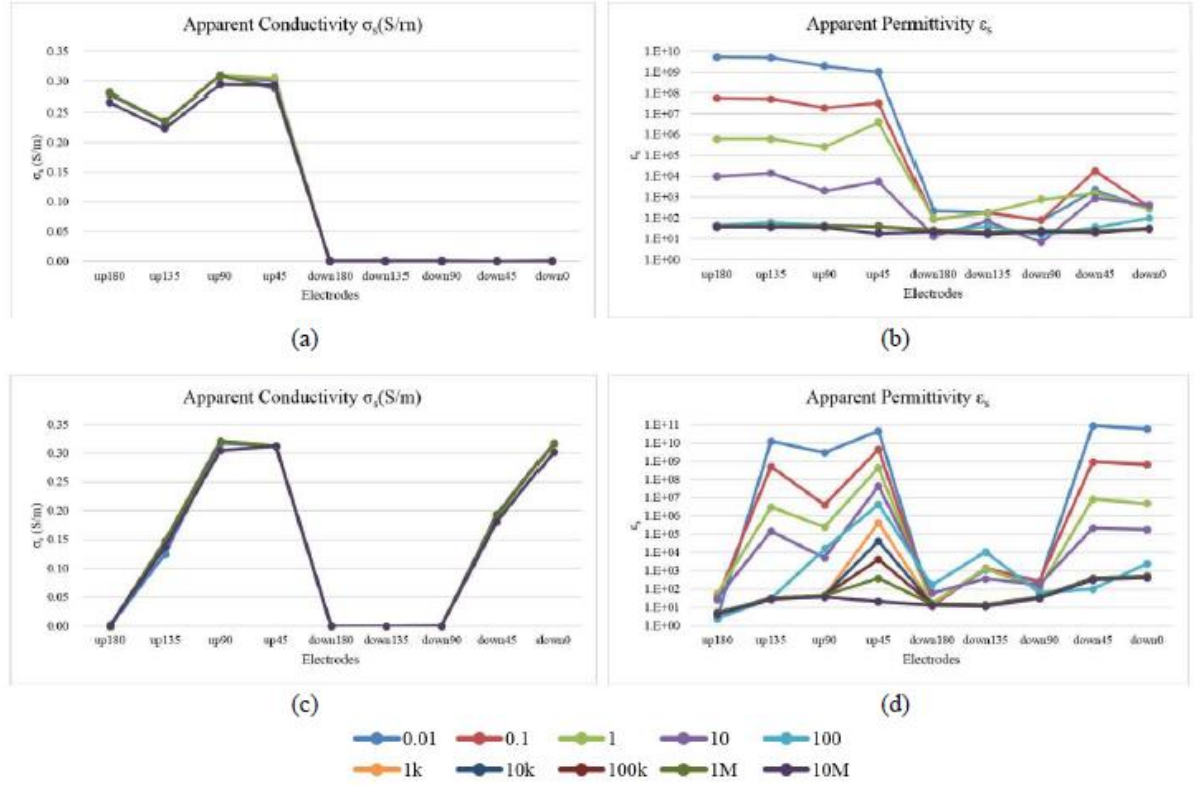


Figure 4: (a) Apparent conductivity σ_s obtained by each electrode pair with horizontal angle of 0° at frequencies from 0.01 Hz to 10 MHz; (b) Apparent permittivity ε_s obtained by each electrode pair with horizontal angle of 0° at frequencies from 0.01 Hz to 10 MHz; (c) Apparent conductivity σ_s obtained by each electrode pair with horizontal angle of 30° at frequencies from 0.01 Hz to 10 MHz; (d) Apparent permittivity ε_s obtained by each electrode pair with horizontal angle of 30° at frequencies from 0.01 Hz to 10 MHz.

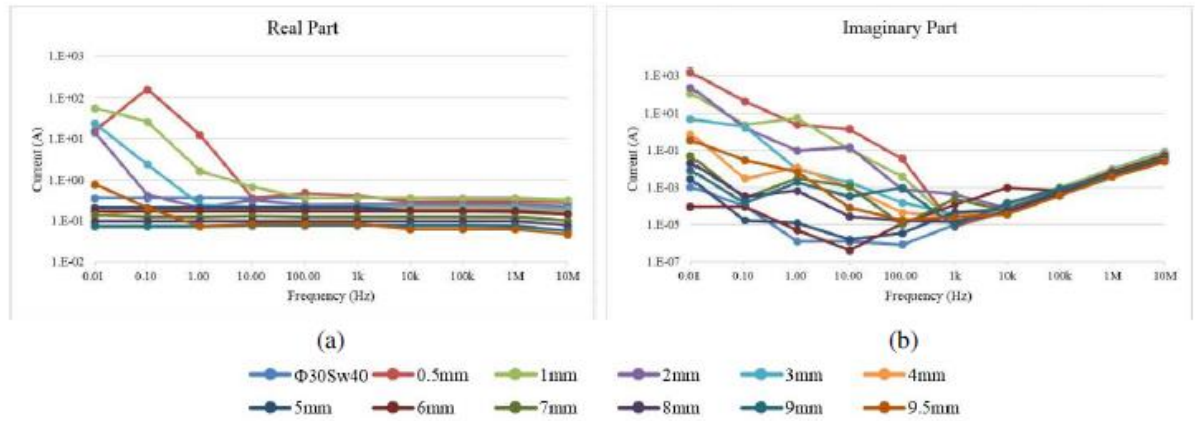


Figure 5: Current strength at the down 180° electrode varying with frequency and thickness of gas hydrate layers: (a) Real part of the current strength; (b) Imaginary part of the current strength.

responses varying with diameter of veins are displayed in Fig. 7. A homogeneous medium with porosity $\Phi = 30\%$, water saturation $S_w = 40\%$ is set to be contrast.

The real part of the current responses decreases with the increase of the gas hydrate content when frequency is higher than 10 Hz. The real part has no obvious correlation with frequency, appealing to common sense. However, it tends to jump or plunge as the frequency decreases below 10 Hz, when the size of gas hydrate reaches a certain specific value. The peak/valley values arise when the layer thickness is 0.5 mm, the block diameter is 5 mm and the vein diameter is 0.1 mm

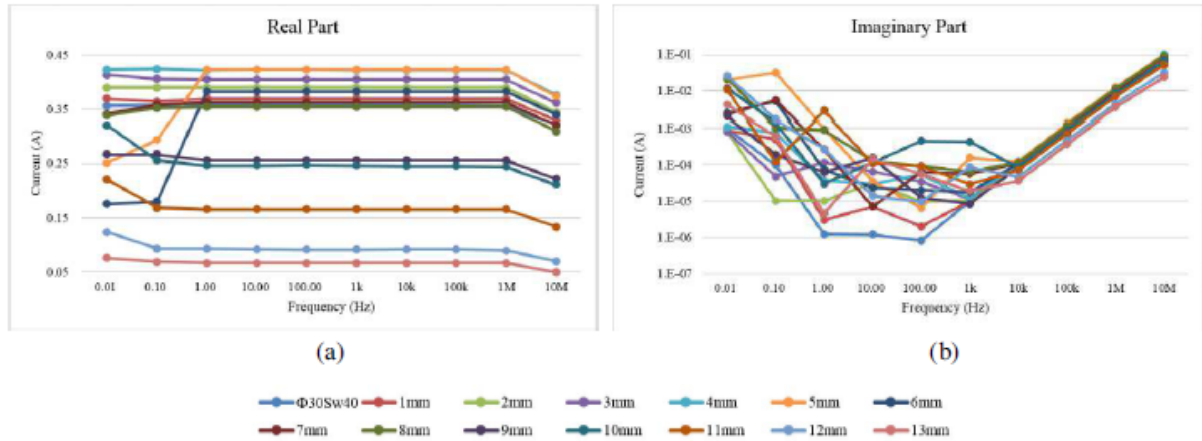


Figure 6: Current strength at the down 180° electrode varying with frequency and diameter of gas hydrate blocks: (a) Real part of the current strength; (b) Imaginary part of the current strength.

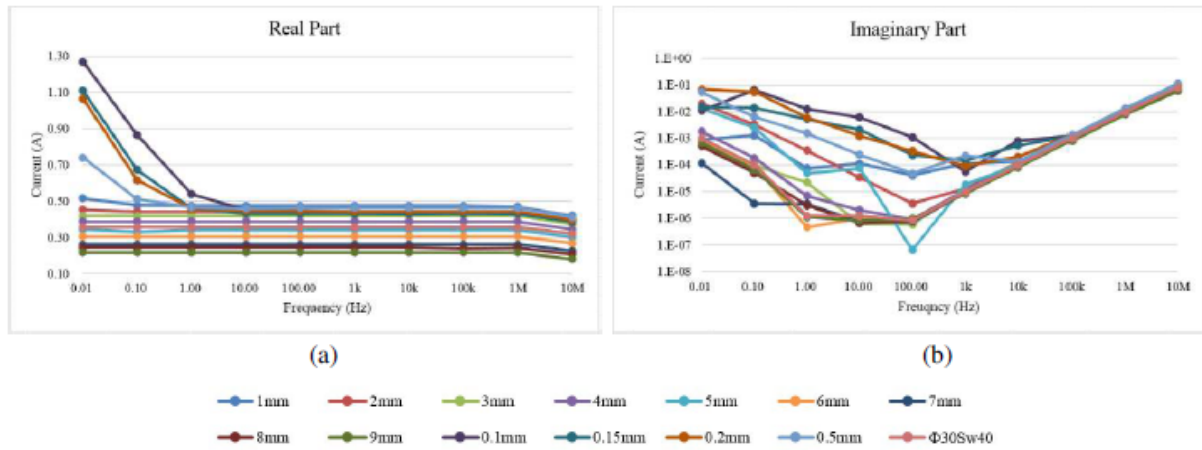


Figure 7: Current strength at the down 180° electrode varying with frequency and diameter of gas hydrate veins: (a) Real part of the current strength; (b) Imaginary part of the current strength.

approximately. Above 10 kHz, the imaginary part of the current strength is proportional to the frequency. As the permittivity of water is obviously higher than the sediment matrix and gas hydrate, the permittivity increases with the water saturation. But the imaginary parts bounce as the frequency decreases in all the three models, and it keeps pace with the corresponding real part. Compared with the homogeneous media containing water, critically large imaginary parts are observed as the gas hydrate layer/block/vein are forming in the reactor. As a result, abnormally large apparent permittivity is inverses.

Obviously, the very large imaginary part of responses at extremely low frequency do not refer to the displacement current, and no evident current density increase is observed in the measured media. The simulation results exhibit that the imaginary parts depends on the shape and size of gas hydrate particles significantly, and there are conspicuous changes of current path. By analogy with complex resistivity logging theory, it is postulated that the current relaxation exists at the interface between the gas hydrate and sediment particles, and it implies that the induced polarization might lead to the abnormally large apparent permittivity at the extremely low frequency.

4. CONCLUSION

To investigate the connections between the gas hydrate distribution and electrode responses, simulations on the complex resistivity measuring equipment and porous media containing gas hydrate were carried out. Firstly, simulations on practical gas hydrate synthesis is performed, the gas hydrate concentration could be deduced from the electrodes clearly. Secondly, models with different gas hydrate distribution forms are calculated, it is proved that the imaginary part of the electrode

responses for the apparent permittivity inversion depends on the shape and size of gas hydrate particles observably. Furthermore, the abnormal increase of the current response is believed caused by the induced polarization effect, and it could be potentially utilized in the evaluation of gas hydrate concentration and recognition of its distribution forms.

ACKNOWLEDGMENT

This work is supported by the National Natural Science Foundation of China (41704124) and Shandong Provincial Natural Science Foundation (ZR2017BEE026), Shandong Provincial Key Technology R&D Program (2017GGX40109), Qingdao Independent Innovation Program (15-9-1-19-jch) and the Fundamental Research Funds for the Central Universities (15CX02120A, 16CX05021A).

REFERENCES

1. Kvenvolden, K. A. and T. D. Lorenson, "The global occurrence of natural gas hydrate. Natural gas hydrates: Occurrence, distribution, and detection," *American Geophysical Union*, 3–18, 2001.
2. Li, X. S., et al., "Investigation into gas production from natural gas hydrate: A review," *Applied Energy*, Vol. 172, 286–322, 2016.
3. Waite, W. F., et al., "Physical properties of hydrate-bearing sediments," *Reviews of Geophysics*, Vol. 47, No. 4, 465–484, 2009.
4. Worthington, P. F., "Petrophysical evaluation of gas-hydrate formations," *Petroleum Geoscience*, Vol. 16, No. 1, 53–66, 2010.
5. Wang, C., L. Xing, et al., "Frequency dispersion characteristics and modeling of complex resistivity of porous medium containing methane hydrate," *Science Technology and Engineering*, Vol. 17, No. 18, 46–54, 2017.
6. Tsallis, C., et al., "Generalized Archie law — Application to petroleum reservoirs," *Physica A Statistical Mechanics & Its Applications*, Vol. 191, Nos. 1–4, 277–283, 1992.
7. Mironov, V. L., et al., "Generalized refractive mixing dielectric model for moist soils," *IEEE Transactions on Geoscience & Remote Sensing*, Vol. 42, No. 4, 773–785, 2004.

[6] 张仲濠,王斌,邢兰昌,等. 基于多路开口同轴探头的介电常数测试系统开发[J]. 科学技术与工程, 2019, 19(32): 205-212. (中文核心)

第19卷 第32期 2019年11月
1671—1815(2019)032-0205-08

科学技术与工程
Science Technology and Engineering

Vol. 19 No. 32 Nov. 2019
© 2019 Sci. Tech. Engrg.

引用格式:张仲濠,王斌,邢兰昌,等. 基于多路开口同轴探头的介电常数测试系统开发[J]. 科学技术与工程, 2019, 19(32): 205-212
Zhang Zhonghao, Wang Bin, Xing Lanchang, et al. Development of permittivity test system with multi-channel based on open-ended coaxial probe[J]. Science Technology and Engineering, 2019, 19(32): 205-212

基于多路开口同轴探头的介电常数测试系统开发

张仲濠 王斌* 邢兰昌 余诗畅 王慧敏
(中国石油大学(华东)信息与控制工程学院,青岛 266580)

摘要 提出并开发了一种基于多路开口同轴探头的介电常数测试系统,利用射频多路开关实现多探头分时工作,获取多路反射系数并对其进行补偿,基于准静态模型反演得到介电常数,首次利用开口同轴探头法实现了介电常数的空间多点测量;然后通过测量已知介电常数的液体,对照液体介电常数理论值进行误差分析,验证了该系统的准确性;最后使用该系统对非均匀含水石英砂进行测量,获得了空间多点的介电常数分布,进一步结合介电混合定律反演得到了空间多点石英砂中水体积分数。结果显示:该系统获得的介电常数反演值与理论值吻合度高,误差分析表明该系统精度优于现有主流的单探头商业测试系统,利用该测试系统可实现对非均匀介质介电常数空间多点分布的精确测量,且测量精度高、可靠性好,扩展了开口同轴探头法在非均匀介质测量中的适用范围,对非均匀介质的微波介电特性研究具有重要科学及工程意义。

关键词 介电常数 空间分布 多点测量 开口同轴探头法

中图分类号 TN98; **文献标志码** A

介电常数^[1]是表征材料电学性能的重要参数之一。常用的介电常数测量方法有平行板电容法、谐振腔法、短路波导法、自由空间法、传输反射法、开口同轴探头法^[2-5]等。相较于其他测量方法,开口同轴探头法样品制备简单、适用频带宽,可在不破坏样品组分的前提下对探头终端开口附近介电常数进行精确测量,是目前广泛应用的一种介电常数测量方法。开口同轴探头法最早由 Stuchly^[6]提出,此后在生物、化工、岩石物理等众多领域得到了广泛应用,针对不同应用特点,该方法得到了持续改进和优化:刘勇等^[3]利用开口同轴探头法对多种混凝土样品的介电常数进行了测量;宋凤珍等^[7]通过搭建同轴探头测试系统,对岩石样品等的介电常数进行测量和误差分析所得数据可靠性较高;Xu等^[8]设计了一种新型椭圆开口同轴探针,通过对甲醇等液体介电常数测量,获得的实验数据与理论数据吻合度较高;Michiyama等^[9]提出了斜切口同轴探针,所测液态有耗材料介电常数与参考数据吻合程度高,为宽

频带下测量有损耗材料的介电常数提供参考;Haukalid等^[10-12]针对管道中水合物厚度检测设计了一种不同的同轴探头,通过介电常数测量,可有效反演薄至1 mm的水合物层厚度,然后将同轴探头安装在管道壁上,实现了对乳液中水合物形成过程的实时监测;Sa等^[13]利用开口同轴探头法对石油/天然气管道中水合物层的介电常数测量,实现了在水饱和和气体环境下对水合物沉积的准确实时监测。然而多孔介质、地质岩心和生物组织等样本的介电常数空间分布具有不均匀性,仅仅获取单一位置介电常数无法全面反映被测介质的介电特性,获取非均匀介质介电常数空间分布对研究其物理性质具有十分重要的意义。

目前开口同轴探头法均使用单一探头对介电常数进行测量,由于该方法要求在测量前必须进行校准^[14],若采用传统的单一探头方式测量不同位置的介电常数,则需要反复移动探头,此时由于探头、稳相线缆的位置发生改变,故每次测量前都需更新校准信息,所以无法实现连续测量,而且探头多次移动极有可能破坏被测介质的原有成分及分布,无法准确获取介电常数的空间分布真实信息。现提出的基于多路开口同轴探头的介电常数测试系统,利用射频多路切换开关实现多探头分时工作方式,在获取多路反射系数的基础上分别对其进行误差补偿,最终反演得到空间中不同位置处的介电常数。

2019年4月22日收到 国家自然科学基金(41704124)、山东省自然科学基金(ZR2017BEE026, ZR2019MEE095)、中国石油科技创新基金(2018D-5007-0214)、山东省重点研发计划(2018GCX101020, 2017GCX40109)和中央高校基本科研业务费专项资金(18CX02112A, 16CX05021A)资助
第一作者简介:张仲濠(1995—),男,汉族,山东济南人,硕士研究生。E-mail: zzzhzh_2008@163.com。

*通信作者简介:王斌(1988—),男,汉族,山东潍坊人,博士,副教授。E-mail: wangbin2015@upc.edu.cn。

1 基于多路开口同轴探头的介电常数测试系统硬件开发

为实现对空间多点介电常数的分时测量,首先开发基于多路开口同轴探头的介电常数测试系统的硬件部分,如图1所示包括反应釜、矢量网络分析仪、上位机、多路温度记录仪、射频多路切换开关、切换开关控制器和开口同轴探头等。

测试过程中被测介质温度的变化对于测量结果有较大的影响,因此可采用恒温水槽进行控温。反应釜内径14 cm、内高12 cm,由聚四氟乙烯制成,置于恒温水槽中。聚四氟乙烯化学性质及宽频介电常数稳定,且损耗低,对于实验测量结果影响基本可以忽略。

矢量网络分析仪 E5061B 的测试频率范围为 5 Hz ~ 3 GHz;射频多路切换开关 87206B 为单刀六掷开关,由动端(端口0)和六路不动端(端口1~6)组成;切换开关控制器基于 ARM 平台开发;多路温度记录仪由六路热电阻温度计组成,热电阻温度计误差为 $\pm 0.15^{\circ}\text{C}$,量程为 $-50 \sim 200^{\circ}\text{C}$;开口同轴探头物理模型如图2所示,长度为 $L=200\text{ mm}$ 、内导体外直径为 $2a=0.51\text{ mm}$ 、外导体内直径为 $2b=1.67\text{ mm}$,内外导体之间由聚四氟乙烯填充。

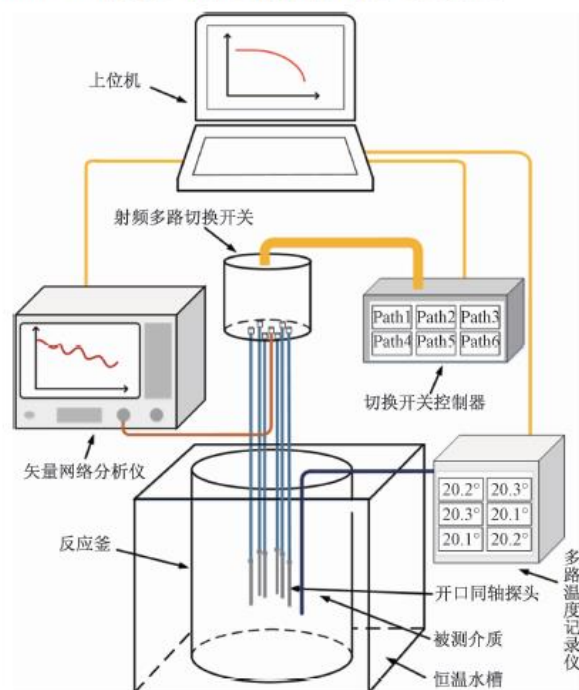


图1 基于多路开口同轴探头的介电常数测试系统硬件组成示意图

Fig.1 Schematic diagram of hardware composition of permittivity test system based on multi-channel open-ended coaxial probe

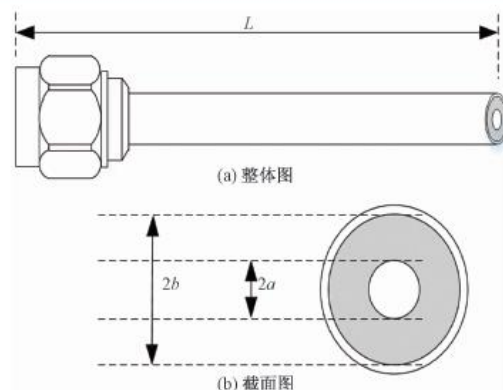


图2 开口同轴探头物理模型

Fig.2 Physical model of open-ended coaxial probe

如图3的实物照片所示,完成基于多路开口同轴探头的介电常数测试系统硬件部分搭建。矢量网络分析仪 E5061B 通过稳相线缆与射频多路切换开关 87206B 的动端相连,87206B 的六路不动端分别通过稳相线缆连接开口同轴探头,探头终端插入反应釜内与被测介质接触实现测量;针对该系统基于 ARM 平台开发了专用的射频多路切换开关控制器,通过排线实现对射频多路切换开关 87206B 的控制及供电;多路温度记录仪通过外接热电阻对被测介质温度进行实时采集记录。上位机通过串口分别与矢量网络分析仪、切换开关控制器和多路温度记录仪相连,通过上位机软件对矢量网络分析仪、切换开关控制器及温度记录仪进行自动控制,同时完成 S 参数、开关通断情况、温度等信息的提取。



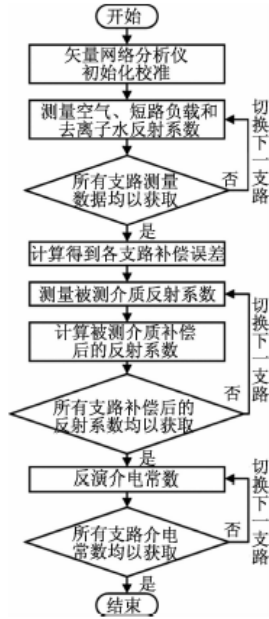
图3 基于多路开口同轴探头的介电常数测试系统硬件部分实物照片

Fig.3 Physical photo of permittivity test system based on multi-channel open-ended coaxial probe

2 基于多路开口同轴探头的介电常数测试系统软件开发

基于多路开口同轴探头的介电常数测试系统的软件部分开发主要包括以下3部分:系统初始校

准、多路数据采集与补偿误差计算、反射系数的修正与介电常数的反演。软件开发的流程示意图如图4所示。



基于多路开口同轴探头的介电常数测试方法的流程图

Fig. 4 Flow chart of permittivity test method based on multi-channel open-ended coaxial probe

2.1 系统初始化校准

首先,将参考面设置在射频多路切换开关端口0处,然后,上位机对矢量网络分析仪发出初始化校

$$\begin{cases} \frac{1 - \Gamma}{1 + \Gamma} = \frac{\sqrt{(\mu_0 \mu_1) / (\varepsilon_0 \varepsilon_1)} c}{\ln(b/a)} \\ c = \int_0^\infty \frac{[J_0(k_c a) - J_0(k_c b)]^2 [1 + 2 \exp(-\sqrt{k_c^2 - \omega^2 \varepsilon_0 \varepsilon_1 \mu_0 \mu_1} d)] \varepsilon_s i \omega \varepsilon_0}{[1 - 2 \exp(-\sqrt{k_c^2 - \omega^2 \varepsilon_0 \varepsilon_1 \mu_0 \mu_1} d)] k_c \sqrt{k_c^2 - \omega^2 \varepsilon_0 \varepsilon_1 \mu_0 \mu_1}} dk_c \end{cases} \quad (2)$$

式(2)中: d 为液体有效厚度,m; Γ 为补偿后的反射系数; k_c 为连续特征值; ε_0 为真空介电常数,F/m; μ_0 为真空磁导率,H/m; ε_1 为同轴探头填充介质的相对介电常数,F/m; μ_1 为同轴探头填充介质的相对磁导率,H/m; ε_s 为测试样品的相对介电常数,F/m; μ_s 为测试样品的相对磁导率,H/m。结合空气、短路负载和去离子水对应的补偿后的反射系数和实际测量的反射系数,构建各支路的补偿方程组,求解出各支路补偿误差 e_d 、 e_r 和 e_s ,得到补偿关系式^[19]:

$$\Gamma_m = e_d + \frac{e_r \Gamma_a}{1 - e_s \Gamma_a} \quad (3)$$

式(3)中: Γ_m 为实际测量的反射系数; Γ_a 为补偿后的反射系数; e_d 为有限方向性误差; e_r 为频率跟踪误差; e_s 为等效源失配误差。

根据上述原理,由上位机向切换开关控制器发

准指令,配合连接开路负载、短路负载、匹配校准件,完成矢量网络分析仪的初始化校准。

2.2 多路数据采集与补偿误差计算

由于初始化校准后的参考面位于与矢量网络分析仪端口直接连接的稳相线缆终端(即射频多路切换开关的端口0处),而实际测量面在同轴探头开口处,同轴探头、稳相线缆和接口均存在插入损耗,所以在利用反射系数反演介电常数前需要对各支路测量的反射系数的误差进行补偿。

空气理论介电常数为1,去离子水的理论介电常数是温度的函数,可通过 Cole-Cole 模型^[15]求得:

$$\varepsilon = \varepsilon_\infty + \frac{\varepsilon_s - \varepsilon_\infty}{1 + (j\omega/\omega_0)^{1-a}} \quad (1)$$

式(1)中: ε_s 为零频介电常数; ε_∞ 为光频介电常数; ω_0 为德拜弛豫角频率, $\text{rad} \cdot \text{s}^{-1}$; a 为 Cole-Cole 因子。表1列举了20、25℃时去离子水的 Cole-Cole 参数^[16]。

表1 去离子水的 Cole-Cole 参数
Table 1 Cole-Cole parameters of deionized water

温度/℃	ε_∞	ε_s	a
20	5.2	80.40	0
25	4.22	78.60	0.013

连接短路负载时补偿后的反射系数 $\Gamma_s = -1$,基于准静态模型^[16-18]反推得到空气和去离子水对应参考面的反射系数(即补偿后的反射系数)为

出指令,接通端口1,同时控制矢量网络分析仪采集端口1所连接探头在空气、短路负载和去离子水中的反射系数并记录去离子水的温度,数据上传完成后,切换射频多路切换开关至下一端口连通,重复数据采集操作直至获取端口1~6所对应的全部反射系数,由上位机存储。结合温度信息,利用式(2)计算空气和去离子水补偿后的反射系数,再利用式(3)构建各端口对应以 e_d 、 e_r 、 e_s 为未知数的方程组。

$$\begin{cases} \Gamma_{am}(i) = e_d(i) + \frac{e_r(i) \Gamma_{aa}}{1 - e_s(i) \Gamma_{aa}} \\ \Gamma_{sm}(i) = e_d(i) + \frac{e_r(i) \Gamma_{sa}}{1 - e_s(i) \Gamma_{sa}}, \quad i = 1, 2, \dots, 6 \\ \Gamma_{wm}(i) = e_d(i) + \frac{e_r(i) \Gamma_{wa}}{1 - e_s(i) \Gamma_{wa}} \end{cases} \quad (4)$$

式(4)中: $\Gamma_{am}(i)$ 、 $\Gamma_{sm}(i)$ 、 $\Gamma_{wm}(i)$ 分别为1~6支路空气、短路负载和去离子水实际测量的反射系数; Γ_{sa} 、 Γ_{ss} 、 Γ_{ws} 分别为空气、短路负载和去离子水补偿后的反射系数。求解式(4)获得各支路对应的 $e_d(i)$ 、 $e_r(i)$ 、 $e_s(i)$ 。

2.3 反射系数的修正与介电常数的反演

将开口同轴探头终端与被测介质接触,利用上位机控制矢量网络分析仪采集端口1反射系数,然后控制射频多路切换开关连通下一支路直至获取各支路的反射系数,结合前步所求得的 $e_d(i)$ 、 $e_r(i)$ 、 $e_s(i)$ 对各支路误差进行补偿,再利用式(3)求得各支路补偿后的反射系数。最终,基于准静态模型式(2),迭代反演得到各支路的介电常数。

3 实验测试及结果分析

为了验证基于多路开口同轴探头的介电常数测试系统的可靠性,利用该系统在恒温条件下对分析纯甲醇、乙醇和乙二醇等三种已知介电常数的液体进行了测量,并对非均匀介质介电常数的空间分布进行了测量,频率范围为300 MHz~3 GHz,设置温度为25℃。

图5和图6分别为甲醇、乙醇和乙二醇所对应的各支路测量和补偿后的反射系数。如图5所示,各支路测量的反射系数在1 GHz以下偏差较小,但偏差随着频率增加而逐渐增大,反射系数在整个频段出现明显波动。如图6所示,各支路补偿后的反

射系数偏差明显变小,且波动基本消失。

图7所示为本测试系统甲醇、乙醇和乙二醇介电常数的反演值(下文称“反演值”)、N1501A开口同轴探头法介电探头套件测量值(下文称“测量值”)及介电常数理论值^[20](下文称“理论值”)。在整个频段上,3种液体反演值实部分布在理论值实部两侧,而测量值实部均大于理论值实部,其中甲醇测量值与理论值偏差较小,乙醇和乙二醇测量值与理论值偏差随频率增加而逐渐增大。3种液体反演值虚部分布在理论值虚部两侧,而测量值虚部与理论值虚部在500 MHz~1.3 GHz范围内相交,低于相交点频率时,测量值与理论值偏差随频率增加而逐渐减小;高于相交点频率时,测量值与理论值偏差随频率增加而逐渐增大。

图8所示为以理论值为基准得到的反演值和测量值的相对误差绝对值,式(5)为其计算公式:

$$|\delta| = \left| \frac{\varepsilon - \varepsilon_0}{\varepsilon_0} \right| \times 100\% \quad (5)$$

式(5)中: $|\delta|$ 为相对误差绝对值, ε_0 为理论值, ε 为反演值或测量值。各支路甲醇反演值实部误差低于5%,虚部误差低于10%;甲醇测量值实部误差低于8%,虚部在频率300 MHz时达到误差最大值15.5%。乙醇反演值实部误差低于8%,虚部误差低于10%;测量值实部在频率2.63 GHz时达到误差最大值16.5%,虚部在频率3 GHz时达到误差最大值13%。乙二醇反演值实部误差低于9%,虚部

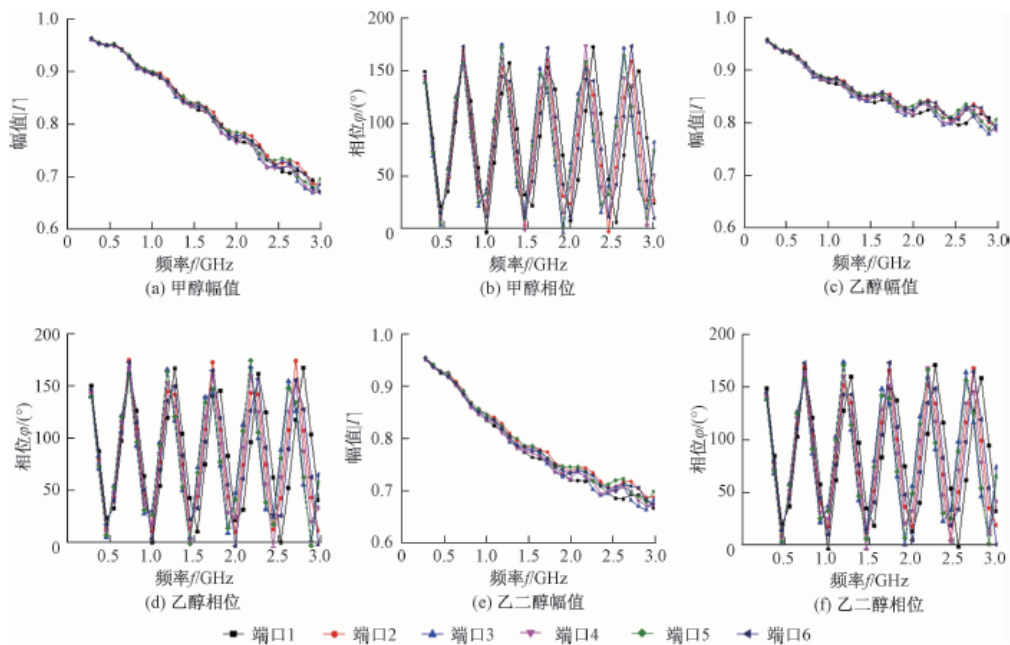


图5 各支路测量的反射系数

Fig. 5 The reflection coefficients measured by each path

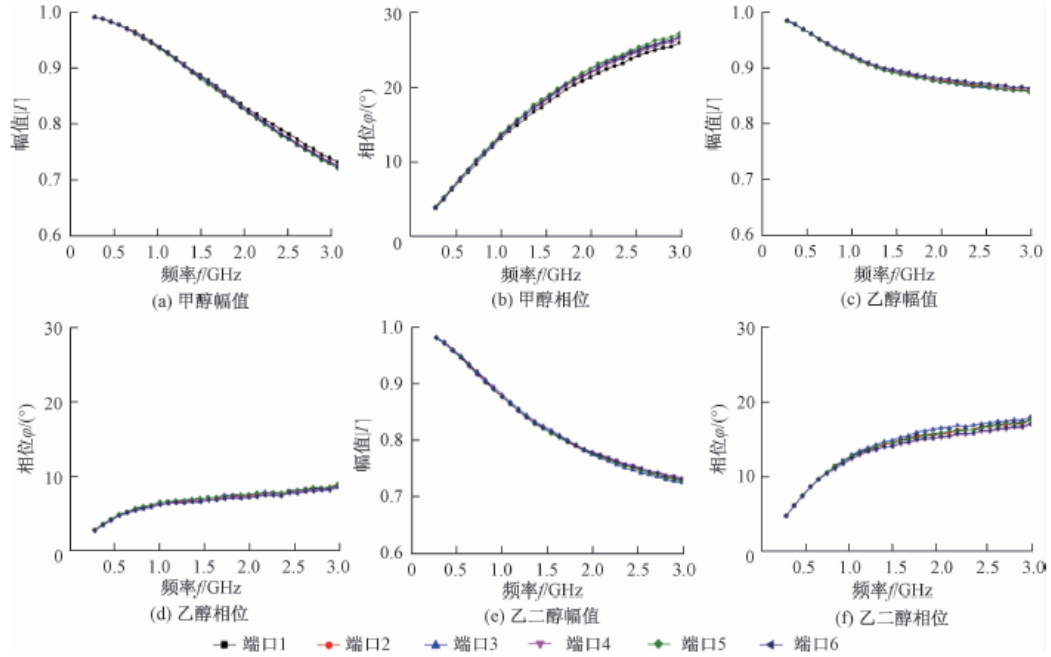


图6 各支路补偿后的反射系数

Fig. 6 The compensated reflection coefficients of each path

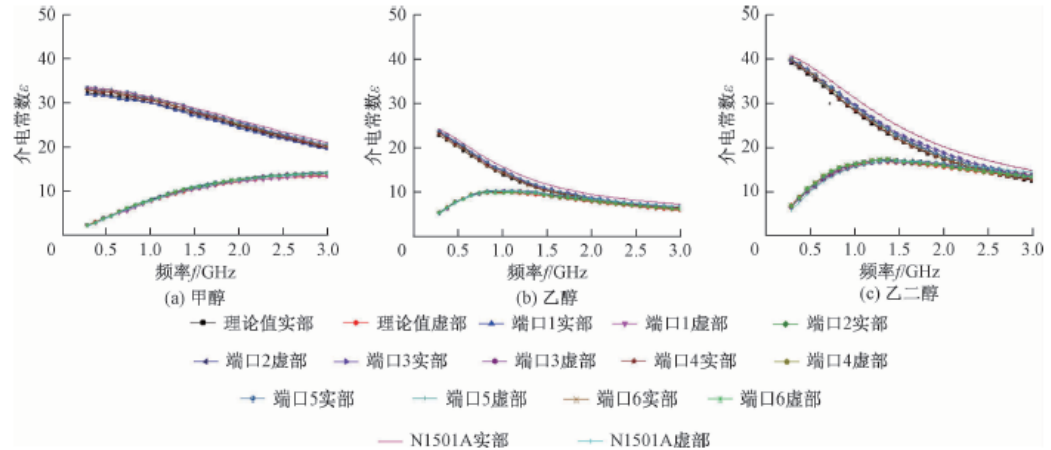


图7 介电常数反演值、测量值和理论值

Fig. 7 The inversed, measured and theoretical permittivity

误差低于10%;测量值实部在频率3 GHz时达到误差最大值18%,虚部在频率300 MHz时达到误差最大值16.5%。本测试系统反演值误差随频率分布均匀,且均低于10%,N1501A测量值实部误差随频率增加而逐渐增大,虚部误差在500 MHz~1.3 GHz范围内达到最小值,低频、高频误差均较大。综合误差分析可知,本测试系统的精度高于现有主流的单探头商业测试系统。

在验证该系统可靠性的基础上,对非均匀介质——含水石英砂进行了如图9所示的介电常数空间分布测量。6个探头在水平方向等间隔插入样本,测得介电常数如图10(a)、图10(b)所示,当观

测点改变时介电常数差异显著,利用不同频率下介电常数[式(6)]——GRMDM介电混合定律^[21]反演得到各个探头附近石英砂中的含水体积分数:

$$\sqrt{\varepsilon_{\text{eff}}^*} = (\sqrt{\varepsilon_f^*} - 1)W + \sqrt{\varepsilon_d^*} \quad (6)$$

式(6)中: $\varepsilon_{\text{eff}}^*$ 为各支路实测介电常数; ε_f^* 为孔隙自由水的介电常数理论值; W 为石英砂中水体积分数; ε_d^* 为干燥石英砂骨架的介电常数,虚部数值可忽略, $\varepsilon_d^* = 2$ 。

如图10(c)所示,各探头在不同频率下反演得到的石英砂中水体积分数一致好,进一步验证了该测试系统对介电常数在空间不同点的测量能力及数据的可靠性。

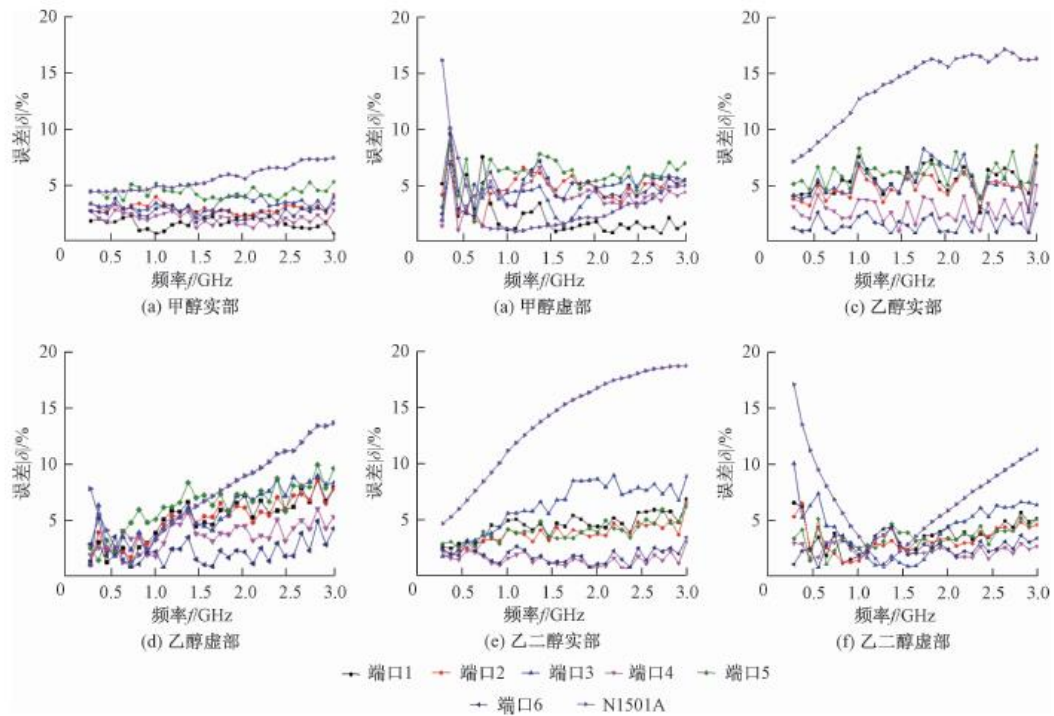


图8 介电常数相对误差的绝对值

Fig. 8 Relative error's absolute value of permittivity

4 结论

提出并开发了一种基于多路开口同轴探头的介电常数测试系统,该系统利用射频切换开关及相应优化反演软件,首次基于开口同轴探头法实现了空间多点介电常数的测量。首先利用该系统对甲醇、乙醇、乙二醇的介电常数进行了测量,获得了6个支路对应3种被测液体的反射系数,基于准静态模型对补偿后的反射系数进行反演,得到各支路的介电常数;然后结合理论值对该系统所得的介电常数及商用开口同轴套件的测量值进行误差对比分析,结果表明本测试系统精度更高,且各支路测量一致性好;最后利用该系统对非均匀介质——含水石英砂

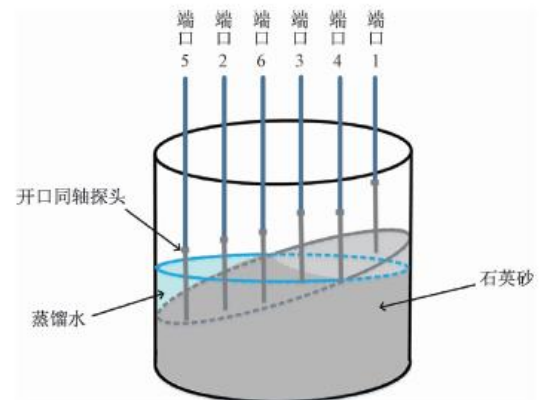


图9 含水石英砂介电常数测量示意图

Fig. 9 Schematic diagram of water-bearing quartz sand measurement

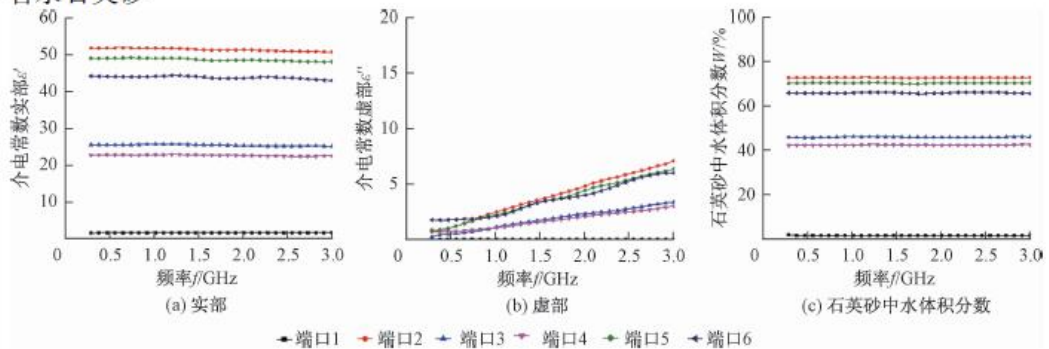


图10 含水石英砂中的介电常数及水体积分数

Fig. 10 Permittivity and water volume fraction in aqueous quartz sand

进行了多点介电常数的测量,并通过介电混合定律反演得到石英砂中水体积分数,进一步验证了该系统的可靠性。该测试系统在保证介电常数高测量精度的基础上实现空间多点检测,对于拓展开口同轴探头法的应用范围及非均匀介质介电常数空间分布的研究均具有重要意义。

参 考 文 献

- 1 武岳山,于利亚. 介电常数的概念研究[J]. 现代电子技术, 2007(2): 177-179,185
Wu Yueshan, Yu Liya. Research on the concept of dielectric constant [J]. Modern Electronic Technology, 2007(2): 177-179,185
- 2 Staebell K F, Misra D. An experimental technique for in vivo permittivity measurement of materials at microwave frequencies[J]. IEEE Transactions on Microwave Theory and Techniques, 1990, 38(3): 337-339
- 3 刘 勇,邹 澎,杨明珊,等. 利用开口同轴探头法测量混凝土块等效电参数[J]. 混凝土, 2012(10): 21-25
Liu Yong, Zou Peng, Yang Mingshan, et al. Measure the equivalent electric parameters of building concrete blocks using open coaxial probe method[J]. Concrete, 2012(10): 21-25
- 4 邓官华,袁马军,蔡林波. MRI 拉莫尔频率范围内人体不同部位大肠癌组织的介电特性[J]. 科学技术与工程, 2018, 18(12): 159-163
Deng Guanhu, Yuan Majun, Cai Linbo. The dielectric properties of human colorectal malignant tissue at larmor frequencies in MRI[J]. Science Technology and Engineering, 2018, 18(12): 159-163
- 5 张 康,武 彤,滕俊恒. 开口同轴探头横电磁波模型法测量液体复介电常数[J]. 电子测量与仪器学报, 2015, 29(7): 945-952
Zhang Kang, Wu Tong, Teng Junheng. Transverse electromagnetic model based open-ended coaxial probe technique for liquid complex dielectric constant measurement[J]. Journal of Electronic Measurement and Instrument, 2015, 29(7): 945-952
- 6 Stuchly M A, Stuchly S S. Coaxial line reflection methods for measuring dielectric properties of biological substances at radio and microwave frequencies: a review[J]. IEEE Transactions on Instrumentation and Measurement, 1980, 29(3): 176-183
- 7 宋凤珍. 岩石电参数测试系统的研究[D]. 成都: 电子科技大学, 2015
Song Fengzhen. Research of the rock electrical parameter testing system[D]. Chengdu: University of Electronic Science and Technology of China, 2015
- 8 Xu Y, Channouchi F M, Bosisio R G. Theoretical and experimental study of measurement of microwave permittivity using open ended elliptical coaxial probes[J]. IEEE Transactions on Microwave Theory and Techniques, 1992, 40(3): 143-150
- 9 Michiyama T, Tanabe E, Nikawa Y. Obliquely cut open ended coaxial probe for obtaining complex permittivity of lossy materials[C]//Asia-Pacific Microwave Conference. Yokohama, Japan: IEEE, 2006, 587-590
- 10 Haukalid K, Folgerø K. Broad-band permittivity measurements of formation of gas hydrate layers using open-ended coaxial probes[J]. Energy and Fuels, 2016, 30(9): 7196-7205
- 11 Haukalid K, Folgerø K, Barth T, et al. Hydrate formation in water-in-crude oil emulsions studied by broad-band permittivity measurements[J]. Energy and Fuels, 2017, 31(4): 3793-3803
- 12 Haukalid K, Folgerø K. Dielectric mixture models for hydrate formation and agglomeration[C]//2018 12th International Conference on Electromagnetic Wave Interaction with Water and Moist Substances. Lublin, Poland: IEEE, 2018: 1-9
- 13 Sa J H, Lee B R, Zhang X, et al. Hydrate management in dead-legs: Detection of hydrate deposition using permittivity probe[J]. Energy and Fuels, 2018, 32(2): 1693-1702
- 14 吴俊军. 开口同轴法测试岩石电性参数的方法研究[D]. 长春: 吉林大学, 2009
Wu Junjun. Open-ended coaxial line method for measuring electrical parameters of rock sample[D]. Changchun: Jilin University, 2009
- 15 Belhadj-Tahar N, Meyer O, Fourier-Lamer A. Broad-band microwave characterization of bilayered materials using a coaxial discontinuity with applications for thin conductive films for microelectronics and material in air-tight cell[J]. IEEE Transactions on Microwave Theory and Techniques, 1997, 45(2): 260-267
- 16 刘 勇. 建筑物等效电参数测试方法的研究[D]. 郑州: 郑州大学, 2012
Liu Yong. The measure method research of equivalent electrical parameters of building[D]. Zhengzhou: Zhengzhou University, 2012
- 17 Nelson S O, Bartley P G. Open-ended coaxial-line permittivity measurements on pulverized materials[J]. IEEE Transactions on Instrumentation and Measurement, 1998, 47(1): 133-137
- 18 亓培培. 射频噪声抑制片评价方法及介电材料介电特性的同轴探头法测量技术研究[D]. 南京: 东南大学, 2016
Qi Peipei. The evaluation method of RF noise suppression sheet and the measurement technique of the dielectric properties of dielectric material by open-coaxial probe method[D]. Nanjing: Southeast University, 2016
- 19 Blackham D V, Pollard R D. An improved technique for permittivity measurements using a coaxial probe[J]. IEEE Transactions on Instrumentation and Measurement, 1997, 46(5): 1093-1099
- 20 Gregory A P, Clarke R N. Tables of the complex permittivity of dielectric reference liquids at frequencies up to 5 GHz[R]. Teddington: National Physical Laboratory, 2001
- 21 王 斌. 宽频介电测井方法的设计与优化[D]. 济南: 山东大学, 2015
Wang Bin. Design and optimizing on dielectric logging with wide frequency band measurement[D]. Jinan: Shandong University, 2015

Development of Permittivity Test System with Multi-channel Based on Open-ended Coaxial Probe

ZHANG Zhong-hao, WANG Bin*, XING Lan-chang, YU Shi-chang, WANG Hui-min


(College of Information and Control Engineering, China University of Petroleum (East China), Qingdao 266580, China)


[**Abstract**] A test system with multi-channel based on open-ended coaxial probe was proposed. The time-dividing operation of the multi-probe was realized by setting a radio frequency multi-way switcher, meanwhile reflection coefficients were compensated, and the permittivity was inversed with quasi-static model. This is the first time to achieve dielectric measurement at multi-point with open-ended coaxial probe. In order to verify the reliability of this test system, several liquids with known permittivity and medium with homogeneous permittivity were measured. Finial, special dielectric distribution information of inhomogeneous sand containing water was obtained by using this system, and water saturation was reversed with dielectric mixing law. Experimental results show that permittivity obtained by the test system match theoretical data precisely. Results from error analysis present that the precision of the system is better than the existing mainstream commercial single probe test system, and it can be used to measure the permittivity of inhomogeneous media accurately. The proposed test system with high precision and reliability expands the application of open-ended coaxial probe method in permittivity measurement of inhomogeneous samples, and it is scientifically and engineeringly significant to dielectric properties study of inhomogeneous media.

[**Key words**] permittivity spatial distribution multi-point measurement open-ended coaxial probe method

5. 专利授权证书

证书号第 2743278 号





发明专利证书

发明名称: 近井眼地层的介电常数频散特性在宽频谱的连续测量方法

发明人: 王斌; 耿艳峰; 华陈权; 邢兰昌; 邱志丹; 郭亮

专利号: ZL 2015 1 0885216.5

专利申请日: 2015 年 12 月 03 日


专利权人: 中国石油大学(华东)

授权公告日: 2017 年 12 月 19 日

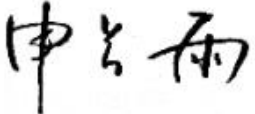
本发明经过本局依照中华人民共和国专利法进行审查, 决定授予专利权, 颁发本证书并在专利登记簿上予以登记。专利权自授权公告之日起生效。


本专利的专利权期限为二十年, 自申请日起算。专利权人应当依照专利法及其实施细则规定缴纳年费。本专利的年费应当在每年 12 月 03 日前缴纳, 未按照规定缴纳年费的, 专利权自应当缴纳年费期满之日起终止。

专利证书记载专利权登记时的法律状况。专利权的转移、质押、无效、终止、恢复和专利权人的姓名或名称、国籍、地址变更等事项记载在专利登记簿上。



局长
申长雨





第 1 页 (共 1 页)

证书号第 3053058 号



发 明 专 利 证 书

发 明 名 称: 含天然气水合物多孔介质阻抗测量装置的仿真和分析方法

发 明 人: 王斌;邢兰昌;刘昌岭;孟庆国;刘乐乐;耿艳峰;华陈权
郭亮

专 利 号: ZL 2017 1 1061908.3

专利申请日: 2017 年 11 月 03 日

专 利 权 人: 中国石油大学(华东)

地 址: 266580 山东省青岛市黄岛区长江西路 66 号

授权公告日: 2018 年 08 月 28 日

授权公告号: CN 107861160 B

本发明经过本局依照中华人民共和国专利法进行审查,决定授予专利权,颁发本证书并在专利登记簿上予以登记。专利权自授权公告之日起生效。

本专利的专利权期限为二十年,自申请日起算。专利权人应当依照专利法及其实施细则规定缴纳年费。本专利的年费应当在每年 11 月 03 日前缴纳。未按照规定缴纳年费的,专利权自应当缴纳年费期满之日起终止。

专利证书记载专利权登记时的法律状况。专利权的转移、质押、无效、终止、恢复和专利权人的姓名或名称、国籍、地址变更等事项记载在专利登记簿上。



局长
申长雨

申长雨



第 1 页 (共 1 页)

6. 项目合同书、任务书

6.1 主持国家自然科学基金（41704124）



项目批准号	41704124
申请代码	D040901
归口管理部门	
依托单位代码	25706108A1489-2710



417041241003105

国家自然科学基金委员会 资助项目计划书

资助类别：青年科学基金项目

亚类说明：

附注说明：

项目名称：天然气水合物储层宽频介电测井响应数值/物理模拟研究

直接费用：24万元 执行年限：2018.01-2020.12

负责人：王斌

通讯地址：山东省青岛市黄岛区长江西路66号

邮政编码：266580 电 话：18562872097

电子邮件：wbl988tt@163.com

依托单位：中国石油大学（华东）

联系人：谭树成 电 话：053286981837

填表日期：2017年08月28日

国家自然科学基金委员会制

Version: 1.003.105



国家自然科学基金委员会资助项目计划书填报说明

- 一、项目负责人收到《关于国家自然科学基金资助项目批准及有关事项的通知》（以下简称《批准通知》）后，请认真阅读本填报说明，参照国家自然科学基金相关项目管理办法及《国家自然科学基金资助项目资金管理办法》（请查阅国家自然科学基金委员会官方网站首页“政策法规”-“管理办法”栏目），按《批准通知》的要求认真填写和提交《国家自然科学基金委员会资助项目计划书》（以下简称《计划书》）。
- 二、填写《计划书》时要求科学严谨、实事求是、表述清晰、准确。《计划书》经国家自然科学基金委员会相关项目管理部门审核批准后，将作为项目研究计划执行和检查、验收的依据。
- 三、《计划书》各部分填写要求如下：
 - （一）简表：由系统自动生成。
 - （二）摘要及关键词：各类获资助项目都必须填写中、英文摘要及关键词。
 - （三）项目组主要成员：计划书中列出姓名的项目组主要成员由系统自动生成，与申请书原成员保持一致，不可随意调整。如果批准通知中“项目评审意见及修改意见表”中“对研究方案的修改意见”栏目有调整项目组成员相关要求的，待项目开始执行后，按照项目成员变更程序另行办理。
 - （四）资金预算表：按批准资助的直接费用填报资金预算表和预算说明书，其中的劳务费、专家咨询费金额不应高于申请书中相应金额。国家重大科研仪器研制项目、重大项目还应按照预算评审后批复的直接费用各科目金额填报资金预算表、预算说明书及相应的预算明细表。
 - （五）正文：
 1. 面上项目、青年科学基金项目、地区科学基金项目：如果《批准通知》中没有修改要求的，只需选择“研究内容和研究目标按照申请书执行”即可；如果《批准通知》中“项目评审意见及修改意见表”中“对研究方案的修改意见”栏目明确要求调整研究期限和研究内容等的，须选择“根据研究方案修改意见更改”并填报相关修改内容。
 2. 重点项目、重点国际（地区）合作研究项目、重大项目、国家重大科研仪器研制项目：须选择“根据研究方案修改意见更改”，根据《批准通知》的要求填写研究（研制）内容，不得自行降低、更改研究目标（或仪器研制的技术性能与主要技术指标以及验收技术指标）或缩减研究（研制）内容。此外，还要突出以下几点：
 - （1）研究的难点和在实施过程中可能遇到的问题（或仪器研制风险），拟采用的研究（研制）方案和技术路线；
 - （2）项目主要参与者分工，合作研究单位之间的关系与分工，重大项目还需说明课题之间的关联；
 - （3）详细的年度研究（研制）计划。



3. 国家杰出青年科学基金、优秀青年科学基金和海外及港澳学者合作研究基金项目：须选择“根据研究方案修改意见更改”，按下列提纲撰写：
 - (1) 研究方向；
 - (2) 结合国内外研究现状，说明研究工作的学术思想和科学意义（限两个页面）；
 - (3) 研究内容、研究方案及预期目标（限两个页面）；
 - (4) 年度研究计划；
 - (5) 研究队伍的组成情况。
4. 国家自然科学基金基础科学中心项目：须选择“根据研究方案修改意见更改”，应当根据评审委员会和现场考察专家组的意见和建议，进一步完善并细化研究计划，作为评估和验收的依据。按下列提纲撰写：
 - (1) 五年拟开展的研究工作（包括主要研究方向、关键科学问题与研究内容）；
 - (2) 研究方案（包括骨干成员之间的分工及合作方式、学科交叉融合研究计划等）；
 - (3) 年度研究计划；
 - (4) 五年预期目标和可能取得的重大突破等；
 - (5) 研究队伍的组成情况。
5. 对于其他类型项目，参照面上项目的方式进行选择和填写。



简表

申请者信息	姓 名	王斌	性 别	男	出生年月	1988年01月	民 族	汉族
	学 位	博士			职称	讲师		
	电 话	18562872097		电子邮件	wbl988tt@163.com			
	传 真			个人网页				
	工 作 单 位	中国石油大学（华东）						
	所 在 院 系 所	信息与控制工程学院						
依托单位信息	名 称	中国石油大学（华东）					代码	25706108A1489
	联 系 人	谭树成		电子邮件	tsc1980@upc.edu.cn			
	电 话	053286981837		网站地址	http://www.upc.edu.cn/			
合作单位信息	单 位 名 称							代 码
项目基本信息	项 目 名 称	天然气水合物储层宽频介电测井响应数值/物理模拟研究						
	资 助 类 别	青年科学基金项目			亚 类 说 明			
	附 注 说 明							
	申 请 代 码	D040901:勘探地球物理学			E091005:海洋资源开发利用			
	基 地 类 别							
	执 行 年 限	2018.01-2020.12						
	直 接 费 用	24万元						

**项目摘要****中文摘要(500字以内):**

天然气水合物是一种极具潜力的新型能源。地球物理测井可较好地对天然气水合物储层进行定性识别,但天然气水合物饱和度的准确定量评价无论在测井方法或解释模型方面都存在许多困难,常规的油气储层测井评价理论不再完全适用。

本项目以前期所提出的宽频介电测井方法为基础,拟进一步研究该方法对天然气水合物储层的响应特性和响应机理,并建立相应的水合物饱和度评价方法。首先,结合仿真与理论研究,建立宽频介电测井辐射电磁脉冲的传播理论模型,揭示影响探测性能的因素及影响机制;然后,研究影响含水合物多孔介质电学频散特性的因素,明确各因素与水合物饱和度之间的关联机理;最后,明确仪器响应、地层介电频散、水合物饱和度之间的内在关联机理,研究利用宽频介电测井定量计算水合物饱和度的方法。

研究成果将为宽频介电测井仪器的开发提供理论和数据基础,为天然气水合物勘探开发中的水合物饱和度定量评价提供更有效的测井技术手段和理论支持。

关键词: 天然气水合物; 水合物饱和度; 介电特性; 测井; 介电响应机理

Abstract(limited to 4000 words):

Natural gas hydrate is potentially a new energy source. The gas hydrate reservoir can be recognized qualitatively through geophysical well logging techniques, however, it is rather difficult to quantitatively evaluate the gas hydrate saturation due to the lack of appropriate well logging methods and interpretation models. The traditional well logging evaluation theory for oil and gas reservoir cannot be used for natural gas hydrate any more.

Based on the new broadband dielectric logging method proposed in the previous work, this project focuses on investigating the characteristics and mechanism of the well logging responses to gas hydrate reservoir and establishing the corresponding evaluation method for gas hydrate. Firstly, the physical model of EM pulses radiated by the broadband dielectric logging tool is established through simulation and theoretical analysis, then the factors affecting the detection performance and the underlying mechanism are studied. Secondly, the factors affecting the frequency dispersion of the dielectric characteristics of the hydrate-bearing porous media are identified and the mechanism of the relation between these factors and hydrate saturation are investigated. Thirdly, the mechanism of the relation among the instrument response, frequency dispersion of the dielectric characteristics and hydrate saturation is disclosed and the hydrate saturation estimation method based on the broadband dielectric logging is proposed.

The outcome of this project aims to enhance the existing theory and data foundation for the development of broadband dielectric logging, and to provide an innovative logging method and theoretical supports for quantitatively evaluating the gas hydrate saturation.

Keywords: Gas Hydrate; Hydrate Saturation; Dielectric Properties; Well Logging; Dielectric Response Mechanism



项目组主要成员

编号	姓名	出生年月	性别	职称	学位	单位名称	电话	证件号码	项目分工	每年工作 时间 (月)
1	王斌	1988.01	男	讲师	博士	中国石油大学(华东)	18562872097	370702198801112215	项目负责人	10
2	邢兰昌	1983.02	男	副教授	博士	中国石油大学(华东)	053286981335	371427198302015535	物理模拟实验	6
3	李国林	1987.07	男	讲师	博士	中国石油大学(华东)	053286981335	370784198707234018	数值仿真、电路调试	6
4	祁雨	1992.09	男	硕士生	学士	中国石油大学(华东)	053286981335	411326199209255839	电磁场理论研究、数值仿真	8
5	朱泰	1992.03	男	硕士生	学士	中国石油大学(华东)	053286981335	372925199203205712	物理模拟实验、仪器性能测试	8
6	李馨	1994.07	女	硕士生	学士	中国石油大学(华东)	053286981335	372301199407250327	数值仿真、物理模拟实验	8
总人数		高级		中级		初级		博士后	博士生	硕士生
6		1		2						3

6.2 主持山东省自然科学基金（ZR2017BEE026）

山东省自然科学基金 资助项目立项任务书

项目 基本 信息	项目名称	天然气水合物储层宽频介电测井响应机理及饱和度评价方法研究				
	立项编号	ZR2017BEE026		项目类别	博士基金	
	执行期限	2017-08至2019-12		资助经费	9.00万元	
	学科分类	海洋资源开发利用		学科代码	E091005	
项目 承担 人 信息	姓名	王斌	性别	男	身份证号	370702198801112215
	电子邮箱	wangbin2015@upc.edu.cn			联系电话	18562872097
	单位名称	中国石油大学（华东）信息与控制工程学院			专业技术 职务	讲师
	所在单位(院系)	信息与控制工程学院			主管部门	中国石油大学（华东）
	所在省级以上重点实验室	无				
项目组成员（与申请书一致，不包含主持人）						
姓名	职称	工作单位	任务分工	每年工作 时间（月）	签名	
邢兰昌	副教授	中国石油大学（华东）	模拟储层试验	8	邢兰昌	
李国林	讲师	中国石油大学（华东）	数值仿真、电路调试	8	李国林	
祁雨	硕士生	中国石油大学（华东）	电磁场理论研究、数值仿真	10	祁雨	
朱泰	硕士生	中国石油大学（华东）	模拟储层试验、仪器性能测试	10	朱泰	
李馨	硕士生	中国石油大学（华东）	数值仿真、模拟储层试验	10	李馨	
需呈交科技报告（篇）						
年度进展报告			最终(技术)报告(必须填，一般为1)			
0			1			
注：严格按照科技报告的有关规定呈交科技报告。项目执行中，年度或中期审核前应呈交进展报告；项目完成后三个月内、开展验收前，须呈交最终（技术）报告。未完成科技报告任务的，项目不予结题。						

资助经费预算表 (单位: 万元)		
科目	预算经费	备注(计算依据与说明)
项目资助总额	9.00	
一、项目直接费用	7.50	
1、设备费	0.00	
(1)设备购置费	0.00	
(2)设备试制费	0.00	
(3)设备改造与租赁费	0.00	
2、材料费	4.00	
3、测试化验加工费	0.00	
4、燃料动力费	0.00	
5、差旅/会议/国际合作与交流费	1.50	
6、出版/文献/信息传播/知识产权事务费	1.70	
7、劳务费	0.30	
8、专家咨询费	0.00	
9、其他支出	0.00	
二、项目间接经费 (比例:17%)	1.50	
1、绩效支出	1.05	
2、管理费	0.45	
3、房屋占用/日常水电气暖消耗	0.00	
三、自筹资金	0.00	
<p>项目负责人承诺: 本人接受山东省自然科学基金的资助, 并将严格遵守山东省自然科学基金委员会关于资助项目管理和财务管理的各项规定, 认真开展研究工作, 按照项目申请书中的内容完成各项指标。按时报送有关材料, 及时报告重大变动情况, 对资助项目发表的论著和取得的研究成果按规定进行标注。</p> <p>项目负责人签字: <u>王文斌</u> 2017 年 11 月 21 日</p>		
依托单位审核意见		山东省自然科学基金委员会办公室审查意见
<p>我单位同意承担该项目, 将保证项目负责人及其研究队伍的稳定和项目实施所需的条件, 严格遵守山东省自然科学基金委员会有关资助项目管理、财务等各项规定, 并做好督促协调工作。</p> <p>依托单位 (公章) 2017 年 11 月 21 日</p>		<p>(公章) 年 月 日</p>

(正反面打印, 一式三份)

山东省自然科学基金委员会办公室2017年制

6.3 主持山东省重点研发计划（2018GGX101020）

山东省重点研发计划 项目任务书

项目编号: 2018GGX101020
项目名称: 基于超宽带脉冲的介电测井仪器设计与应用研究
项目主管部门 (甲方): 中国石油大学 (华东)
项目承担单位 (乙方): 中国石油大学 (华东)
项目协作单位: 中国石油大学 (华东) 石油工业训练中心
项目负责人: 王斌
联系电话: 18562872097
起止时间: 2018 年 01 月至 2020 年 01 月

山东省科学技术厅
二〇一七年制

填 写 说 明

1. 本任务书系省科技厅为组织山东省重点研发计划项目研究而设计，任务书甲方为科技发展计划项目主管部门，乙方为项目承担单位。

2. 本任务书部分内容由山东省科技计划管理信息系统自动生成，承担单位可根据项目实际情况进行补充修改。

3. 本任务书需用 A4 纸打印，一式四份，项目主管部门一份，项目承担单位一份；省科技厅两份。

一、项目基本信息表

单位名称	中国石油大学 (华东)			主管部门	中国石油大学 (华东)	
单位类型	[01]	01.高等院校 02.科研院所 03.国有企业 04.集体企业 05.私营企业 06.有限责任公司 07.股份有限公司 08.股份合作企业 09.联营企业 10.其它				
通讯地址	山东省青岛市黄岛区长江西路66号			邮政编码	266580	
项目负责人	姓名	性别	出生年月	身份证号码	联系电话	
	王斌	男	1988-01-11	370702198801112215	18562872097	
	传真		手机	E-mail		
	053286983326		18562872097	wangbin2015@upc.edu.cn		
职工总数	3385	人	大专以上人员	3125	人	研究开发人员 1659 人
项目起始时间	2018-01-01			计划完成时间	2020-01-01	
技术领域	[01]	01. 电子信息 02.新材料 03. 先进制造 04. 新能源与高效节能 05. 交通运输 06. 现代服务业 07. 化工及建材 08. 轻工纺织 09.农业高技术 10. 农业生产 11. 农业设施装备 12. 农业现代产业 13. 新农村建设 14. 海洋科技 15. 资源与节约 16. 环境与可持续发展 17. 人口与健康 18. 中医药现代化 19. 公共安全 20. 生物技术 21.城镇发展与其他社会事业 22. 高新技术创新服务				
项目类别	[1] 1.科研 2.中试 3.新产品开发					
研究方式	[1] 1.本单位独立完成 2.产学研结合 3.引进消化再创新					
主要优势	[3][6][1](按优势大小选择三项) 1.重大理论突破 2.技术工艺创新突出 3.市场前景广阔 4.经济效益显著 5.社会效益显著 6.形成自主知识产权 7. 其它					
项目完成时 预期成果走向	知识产权 情况	专利	其中发明专利	技术标准	著作权	动植物新品种
		2	2	0	0	0
	科技报告 (篇)	立项报告	进展报告	专题报告	最终(技术)报告	合计
		1	1	1	1	4
	技术水平	[02] 1.国际领先 2.国际先进 3.国内领先 4.国内先进 5.省内领先 6.省内先进				
	市场前景	[03] 1.出口创汇 2.替代进口 3.填补国内空白 4.填补省内空白				
	产业化后 经济效益	年增销售收入(万元)	年增税收(万元)	年增利润(万元)	创汇(万美元)	
		100.00	20.00	50.00	30.00	

二、主要研究内容

A、运用复模式匹配理论研究宽带脉冲在近井眼区域的传播特性，揭示电磁波传播规律对仪器探测性能的影响机理。

介电测井使用远高于感应测井的微波频段，在地层中传播的电磁能量是地质信息的载体，电磁波的传播规律直接影响仪器的探测深度、聚焦范围等性能。金属钻铤、泥浆井眼、侵入带等区域构成了开放式单导体波导结构，仪器发射脉冲的频带覆盖范围从几十兆赫到上千兆赫，电磁波的传导、辐射过程十分复杂，在井眼周围区域允许众多电磁波模式存在，电磁波以哪些模式传导、模式的场强分布、辐射场所占比例等都将影响仪器的响应区域。为了对仪器探测范围、聚焦能力进行优化控制，揭示脉冲信号、地层参数和仪器响应之间的内在联系，我们将利用电磁场数值方法分析电磁波空间分布情况，同时引入复模式匹配理论，分析近井眼区域波导模式的特性，通过研究各个模式能量占总场强的比重，对宽带电磁脉冲在近井眼范围的传播特性进行研究，探索复杂泥浆侵入情况、井眼构成等因素对仪器探测性能的影响。

B、研究井眼中宽带脉冲的发射接收机制，设计并优化UWB 井眼天线以提高仪器性能。

现有的介电测井仪器使用缝隙天线、偶极天线等作为发射接收装置，这些天线无法满足脉冲信号的带宽需求，如果在已有仪器基础上进行研究，将严重限制宽频法优势的发挥。近年来，科学家们对脉冲井眼雷达进行了大量的研究，这促进了UWB 井眼天线的发展。针对宽带介电测井仪的工作特点，优化设计专用的UWB 井眼天线是本课题工作的一部分。我们拟结合复模式匹配理论，探索井眼天线对宽带脉冲的发射机制，研究天线的激发场对于不同电磁波模式的耦合效率，针对仪器的探测需求，揭示发射天线结构与仪器探测范围之间的内在联系，完成对井眼天线的优化设计。

C、搭建测试短节，研究样机对不同含流体饱和度地层的探测性能。

通过数值模拟和物理实验考查改变宽频介电测井仪参数（脉冲带宽、脉冲波形、收发天线源距、测量短节结构等）与地层参数（泥浆侵入情况、地层框架、含流体饱和度、流体种类等）对测井响应的影响规律。拟采用基于GPU 加速的时域有限差分法来提高仿真效率，使仿真模型尽可能模拟实际情况。在得到优化参数的仿真结果基础上，搭建测试短节，配合实验室测试平台获取仪器在已标定电学参数的样本地层中的时域、频域响应，改变样本的地层框架成分、含流体饱和度等参数，探索仪器在不同地层中的性能变化，验证仿真结果的正确性。

D、在明确仪器探测过程的基础上，研究宽频介电测井响应的数值反演算法。

结合通过仿真与实验得到的时域、频域测井响应曲线，依据明确标定的地层电学信息，引入时频分析手段，创新地将二维测井信息扩展到时间-频率-深度三维空间，将隐含在原始测井数据中的地层信息提取出来，从而提高仪器分辨率，使仪器的宽频优势得到充分发挥；进一步探索从时频测井数据中获取地质参数在径向深度分布的手段，与已标定的地层参数相比较，构建完整的近井眼介电信息反演方法。

三、主要技术指标

- 1、制作超宽带井眼天线，工作频率覆盖250MHz 至2GHz 范围 ($S_{11} \leq -10\text{dB}$)，满足圆柱形钻杆共形需求。
- 2、制作基于超宽带脉冲的介电测井短节样机，短节集成度高，长度小于800mm，工作温度范围覆盖-10℃-100℃，短期不高于150℃。径向探测深度达到300mm，轴向分辨率高于5mm。
- 3、提出针对超宽带介电测井的反演算法，能够实现不同径向深度介电参数的提取，反演方法可实现对厚度大于10mm 的薄储层分辨。

四、主要创新点及先进性

创新点：

- 1、以超宽带脉冲作为探测信号，不仅通过一次测量便可获取整个带宽下连续的地层介电频散信息，而且大大简化了多点扫频法带来的复杂探测周期问题，降低了因单频测量误差造成对地质参数错误评估的可能。此外，基于单次脉冲的方法可提高的信号功率，提升系统信噪比，保证测井准确性。
- 2、引入时频手段，研究针对宽频法的解释算法，创新地将测井曲线扩展到时间-频率-深度三维空间，将隐含在原始测井数据中的地层信息提取出来，使仪器的宽频优势得到充分发挥，进一步提高测井的准确性及效率。
- 3、运用电磁场数值分析与经典理论相结合的方法，对超宽频带电磁波传播规律进行系统分析。首次运用复模式匹配理论来研究能量在模式空间的分布情况，从根本上掌握宽带脉冲激发、辐射规律。

先进性：

我国在介电测井领域，一直以仿制国外仪器为主，总体行业水平与国际先进水平存在代差。目前最先进的介电频散测量是基于多点频测量后拟合实现的，本课题研究的宽频介电测井方法，能够提供连续带宽的介电频散测量，且该方法是第一种具备这种能力的测井方法，样机将成为我国第一台具备自主知识产权的介电测井仪器，通过优化改良，有望使我国在介电测井行业达到国际先进水平。

五、项目经费预算

五、项目经费预算				
项目计划总投资		21.60 万元	其中已完成投资	0.00 万元
计划新增投资来源	单位自筹		0.00 万元	
	金融贷款		0.00 万元	
	财政拨款	21.60 万元	其中:国家财政拨款	0.00 万元
			省科技经费	21.60 万元
			地方政府配套	0.00 万元
	其它		0.00 万元	
新增投资中省科技经费支出预算	直接经费		设备费	3.60 万元
			材料费	8.00 万元
			测试化验加工费	0.00 万元
			燃料动力费	0.00 万元
			差旅会议国际合作与交流费	3.50 万元
			出版/文献/信息传播/知识产权事务费	3.00 万元
			劳务费	0.50 万元
			专家咨询费	0.00 万元
			其它费用	0.00 万元
	间接费用		承担单位为项目研究提供的房屋占用, 日常水、电、气、暖消耗	0.00 万元
			有关管理费用的补助支出	1.52 万元
			激励科研人员的绩效支出	1.48 万元
			其它费用	0.00 万元

六、项目进度安排

	开始时间	截止时间	完成的主要指标(要可考核)
计划进度	2018-01-01	2018-06-30	搭建针对超宽带介电测井的井眼天线测试平台,完成井眼天线设计及性能优化,在此基础上申请发明专利一项。
	2018-07-01	2018-12-31	完成超宽带介电测井仪器样机制作,并结合地层模型,在实验室内完成对其主要性能指标的测试。
	2019-01-01	2019-06-30	结合数值仿真与实验数据,明确电磁波在地层中的传播规律与接收信号的内在联系,揭示宽频介电测井评价地层流体饱和度的机理,发表核心论文一篇。
	2019-07-01	2020-01-01	完成宽频介电测井仪器样机测试,形成一套具有自主知识产权的介电测井仪器,并针对新仪器申请发明专利一项。

七、项目课题组成员

[illegible]

八、任务书签订各方意见

项目主管部门（甲方）

负责人（签字）

郝芳



项目承担单位（乙方）

项目负责人（签字）

耿彦

财务负责人（盖章）

耿彦印



省科技厅主管处、单位

负责人（签字）



九、共同条款

1. 乙方必须按要求编报年度计划执行情况、下一年度经费预算和有关统计报表，交甲方汇总后，及时上报省科技厅。逾期不报，省科技厅有权暂停拨款。

2. 任务书执行过程中，乙方如需调整任务，向甲方提出变更内容及其理由的申请报告，经甲方审核后报省科技厅审定后实施。未接到正式批准书以前，双方须按原任务书履行，否则后果由自行调整的一方负责。

3. 乙方因某种原因（如：与项目申请书内容有出入、挪用经费、技术措施或某些条件不落实）致使计划无法执行，而要求中止，应视不同情况，部分、全部退还所拨经费；如乙方没有提出中止任务书的要求，甲方可根据调查情况有权提出中止的处理建议，报省科技厅审核批准后执行。

4. 甲方根据应用技术研发资金开支的规定，监督经费的使用情况。凡不符合规定的开支，甲方负责提出调整意见。必要时，省科技厅有权直接提出调整或撤销意见。

5. 乙方应严格按照规定提交相应的科技报告：立项下达后、任务书签署前，应呈交立项报告；项目执行中，年度或中期审核前应呈交进展报告；专题报告[指实验（试验）报告、调研报告、工程报告、测试报告、评估报告等蕴含科研活动细节及基础数据的报告]根据项目执行情况据实呈交；项目完成后三个月内、申请验收前，须呈交最终（技术）报告。对未提交相应科技报告或者科技报告质量达不到合格标准的项目，按不通过验收或不予结题处理。

6. 本任务书签订各方均负有相应的责任。若有争议或纠纷时，按山东省重点研发计划管理办法有关条款处理。

项目编号：27R1505023A

中国石油大学（华东）

自主创新科研计划项目

计划任务书

项目名称：基于瞬变信号随钻电阻率地质导向的理论
研究及设计

项目类型：青年基金

所属学科：地球物理学、电子技术

负责人：王斌 联系电话：18562872097

电子邮件：wangbin2015@upc.edu.cn

依托单位：信息与控制工程学院

研究期限：2015 年 9 月 至 2017 年 9 月

2015 年 9 月 24 日填

一、基本信息

负责人信息	姓 名	王斌	性 别	男	出生年月	1988.1
	最后学位	博士	授予时间	2015.6	职 称	讲师
	主要研究方向	电法测井、电磁场数值计算				
	所属科研机构	信息与控制工程学院				
承担单位		信息与控制工程学院		合作单位		
项目信息	项目名称	基于瞬变信号随钻电阻率地质导向的理论研究及设计				
	隶属学科	地球物理学、电子技术			批准金额(万元)	5.0
	项目类型	A.青年基金				
	起止时间	2015 年 9 月 至 2017 年 9 月				
	主题词(3个)	地质导向; 瞬变信号; 随钻测井				
	预期成果	<input checked="" type="checkbox"/> 专著、论文 <input checked="" type="checkbox"/> 专利				
项目组成员	姓名	所在单位	职称	本项目中承担的任务	签字	
	王斌	信控学院自动化系	讲师	电法测井、 电磁场数值计算	王斌	
	郭亮	信控学院自动化系	讲师	电阻率测井、 电阻率成像	郭亮	
	王圣杰	信控学院自动化系	在读硕士研究生	电阻率测井硬件设计、 信号处理	王圣杰	
	涂梦雨	信控学院自动化系	在读硕士研究生	电阻率测井、 电磁场数值计算	涂梦雨	
	刘亚伟	信控学院自动化系	在读硕士研究生	电阻率测井硬件设计、 信号处理	刘亚伟	
<p>项目摘要(限400字以内):</p> <p>地质导向技术通过测量近钻头多种地质、工程参数来对所钻地层进行实时评价,采用地质导向技术可以大大提高钻头在储层内轨迹的控制能力。本项目在已有电阻率地质导向仪器的基础上,提出了一种基于瞬变宽频信号的地质导向方法,着重研究了宽带信号在复杂分层储层中的传播及仪器响应特性,深入探究电磁波在地层界面处的反射机理,并针对该仪器提出了一种基于时频分析的数据解释、后处理方法。</p> <p>以电磁场理论分析和基于图形处理器(GPU)的并行时域有限差分法为主要研究手段,建立含有多个不同角度界面的地层模型,研究了井眼、钻铤等结构对瞬变信号传播的影响,以及宽带信号在分层地层中的传播特性;通过仿真数据与实验室测试的结合,对仪器工程参数、收发天线、信号的带宽等进行最优化设计;结合时频分析技术,利用接收信号频率成分的时变特性,提出一种针对该地质导向仪的解释方法。本项目的研究成果将为瞬变电阻率地质导向这种新方法的应用奠定理论基础。</p>						

注:1.“承担单位”、“合作单位”填写负责人所在院部等二级单位;2.项目“隶属学科”填二级或以下学科;3.项目组成员“所在单位”填写所在院部等二级单位。4.若为“研究生创新项目”,则项目组成员中第一位应为其导师。

二、研究目标、主要研究内容

1. 研究目标

掌握宽频瞬变信号在井眼周围复杂地层的传播特性,明晰电磁波在遇到不同类型地层边界时的反射机理;根据理论原理及仿真结果,确定最适合用作地质导向的瞬变信号波形和频率范围,使得仪器具备良好的分辨率和探测深度,并针对其优化接收发送天线,提高电磁波收发效率;设计针对该地质导向技术的解释方法,确定适合的小波类型,并优化尺度参数。以上目标的实现将为基于瞬变信号的电阻率地质导向技术的应用奠定理论基础。

2. 主要研究内容

(1) 对近钻头电阻率测量仪发射瞬变信号的传播特性进行建模仿真,通过仿真获得宽频瞬变信号在井眼地层中的传播基本特性。

研究近钻头电阻率地质导向仪器在不同岩性,含水、油饱和度地层运行时的电磁波传播特性,研究发射机辐射出的电磁波在井眼及井眼周围地层中的分布情况,明确电磁能量的存在模式及传输机理。

(2) 研究金属钻头、钻铤及钻井液对瞬变信号的影响,明确收发天线的安装位置、源距等几何参数。

仿真建模真实的金属钻头、钻铤结构,分析仪器本身结构对宽频信号的影响,并研究接收器得到一次场的传播特性,为仪器的解释方法的设计提供理论依据。探索水基钻井液、油基钻井液等不同井眼环境对瞬变信号传播的影响,对仪器的安装位置,与钻头之间的距离,以及源距等参数进行优化。

(3) 对仪器在各种地层中对不同边界的响应情况进行研究,探索地层界面对电磁波造成反射的机理。

为使得地质导向仪器能对地层边界做出准确判断,进而使钻杆在最佳地质目标内钻进,就需要仪器兼备足够的探测深度以及高分辨率。对不同地质特性的地层边界以及角度距离的地层边界进行建模仿真,研究瞬变信号波形、带宽等参数与探测深度分辨率之间的联系,对瞬变信号进行优化,并根据井眼、仪器的工业设计对电磁波收发装置进行优化改良。

(4) 结合仿真结果,研究针对瞬变信号地质导向技术的解释方法。

以通过计算机仿真得到的大量数据为基础,探索对测量数据进行时频分析的方法,研究地层边界与测量数据之间的对应关系,优化小波类型、尺度参数等,从而给出针对瞬变地质导向的恰当解释手段。

(5) 实验验证仿真结果及理论分析结果。

根据研究结果提出宽频瞬变地质导向仪的制备需求,利用实验室已有设备或其他加工平台进行加工,通过实验室验证仪器响应与地层边界间的关系,修正理论和仿真获得的参数。根据优化参数进行实际上井测试,通过实验结果进一步优化设计参数及仪器响应的解释方法。

三、预期成果及考核指标（预期成果及考核指标应切实可行，须量化可考核）

本项目相关研究成果拟以学术论文形式在国内外重要期刊上发表至少 2 篇，且均被 SCI 收录。

四、项目研究进度计划

2015.9-2015.12

建立不同岩性、含水、含油地层的电学模型；

2016.1-2016.3

对瞬变信号在单一地层的传播规律进行仿真计算，提取瞬变电磁波的时变场分布，分析其传播特性，根据仿真结果确定最佳的瞬变信号波形、频率等参数。

2016.4-2016.6

对不同源距、安装位置等几何参数的瞬变电阻率地质导向仪的电磁场传播情况进行研究，对源距、收发天线等结构进行优化设计。

2016.6-2016.8

研究在与地层界面平行放置时，仪器对单一、多层地层的响应及瞬变信号在复杂地层的传播规律。

2016.9-2016.12

建立与钻进方向具有一定夹角的地层模型，研究仪器对地层界面方位角的预判能力。

2017.1-2017.3

结合已得到的实验数据和机理分析，以时频变换为工具解释测井数据，优化用于变换的各个参量，使仪器得到最高分辨率。

2017.4-2017.6

搭建实验室测试平台和样机，结合多种射频测试仪器，完成对瞬变电阻率地质导向仪的实验室验证。

2017.6-2017.8

结合实验室数据，修正理论和仿真获得的优化参数，并以更为丰富的实验结果为指导，对数据解释方法及后处理进行进一步改良。

五、经费预算表

(单位: 万元)

科目	申请经费	计算依据与说明
一.研究经费		
1.科研业务费		
(1) 测试/化验/加工费		
(2) 会议费/差旅费		
(3) 出版物/文献/信息传播费/知识产权事物费	1.6	论文发表、查新和专利费, 以及购买图书、复印费
(4) 其它 (说明列应具体阐述)		
2.实验材料费		
(1) 原材料 / 试剂 / 药品购置费		
(2) 其它 (请注明)	1.35	购买办公用打印机硒鼓 2 个, 用于数据存储硬盘 6 块, 升级计算机内存条等电脑配件, 打印纸等其他办公耗
3.仪器设备费 (小型)		
(1) 购置	1.7	购买高性能计算平台 2 台
(2) 试制	0.2	用于实验室测试电路及测试平台搭建
(3) 维修、租赁		
二.国际合作与交流费		
三.劳务费 (详细说明)	0.15	三名研究生 0.05×3
四.专家咨询费		
合 计	5	

六、计划任务书各方签约

1. 项目负责人承诺

本人确认本计划任务书及附件内容真实、准确。将严格按照《中国石油大学（华东）自主创新科研计划项目管理办法（试行）》与本计划任务书的规定，认真履行项目负责人职责，积极组织开展研究工作，合理安排研究经费，按时报送有关材料并接受检查。若在项目执行过程中违反有关规定，本人将承担全部责任。

负责人（签字）：

2015年10月9日

2. 承担单位及合作单位承诺

（1）承担单位

已经按照学校有关规定与项目申报要求对计划任务书内容进行了审核。我单位将根据项目研究内容，落实项目研究所需条件；认真履行项目承担单位的管理职责。

负责人（签字）：

2015年10月12日

（2）合作单位

同意参加合作研究，将按照学校有关规定，认真履行项目合作单位的管理职责。

负责人（签字）：

（公章）

年 月 日

3. 科技处审核意见

同意立项

负责人（签章）：

2015年10月9日

4. 学校自主创新科研计划领导小组审批意见

同意立项

负责人（签章）：

2015年10月9日

项目编号: 15CX02120A

中国石油大学（华东）

自主创新科研计划项目

结题报告

项目名称: 基于瞬变信号随钻电阻率地质导向的理论研究
及设计

所属学科: 地球物理学、电子技术

研究期限: 2015 年 9 月—— 2017 年 9 月

负 责 人: 王斌

承担单位: 信息与控制工程学院

联系电话: 18562872097

电子邮件: wangbin2015@upc.edu.cn

2017 年 12 月 9 日填

一、预期成果与考核指标完成情况（与任务书对比填写）

已发表会议论文一篇，并被 EI 检索，申请两项发明专利，已获得一项发明专利授权。

基金已升级为国家自然科学基金（41704124）和山东省自然科学基金（ZR2017BEE026）。

二、研究内容执行情况（任务书主要研究内容完成情况，详细填写）

（1）对近钻头电阻率测量仪发射瞬变信号的传播特性进行建模仿真，通过仿真获得宽频瞬变信号在井眼地层中的传播基本特性。

通过对斯伦贝谢公司的 MWD 工具 Ecoscope 进行时域有限差分法及有限元法建模仿真，获得单一 2MHz 频率下钻具穿过不同井眼地层时的传播特性及仪器响应，进而选择 1kHz-200MHz 下带宽的脉冲信号作为发射信号，结合复模式匹配理论与数值仿真算法获得宽带响应，得到结论：

- a、传统单一频率近钻头电磁波测井比瞬变信号探测深度更大
- b、瞬变信号在近井眼地层传播色散严重，高频成分穿透深度浅
- c、瞬变信号携带信息量远高于单一频率信号，但反演难度远高于单一频率

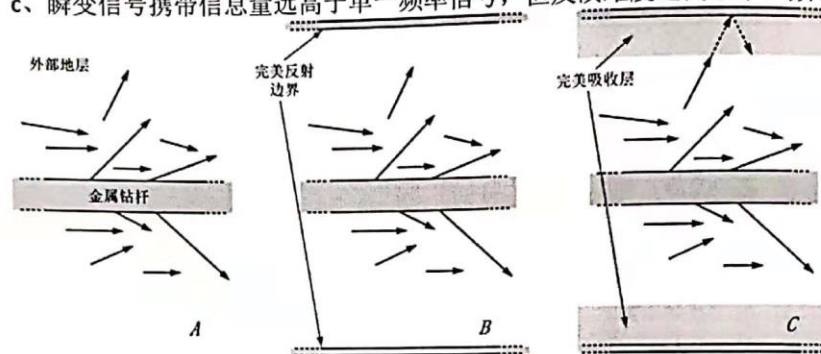


图 1.利用复模式匹配理论离散单导体开波导中辐射模的示意图

（2）研究金属钻头、钻铤及钻井液对瞬变信号的影响，明确收发天线的安装位置、源距等几何参数。

首先基于已有的 Ecoscope 钻具建模仿真，直接给已有收发系统加载宽带脉冲信号，然后分析其结构、井眼等对脉冲收发影响，优化天线设计。得到结论：

- a、使用线圈发射宽带脉冲时，由于线圈本身谐振频率固定，故不同频率电磁波的反射系数、驻波比差异较大，造成发射出去的脉冲失真严重
- b、针对脉冲带宽，设计了收发天线

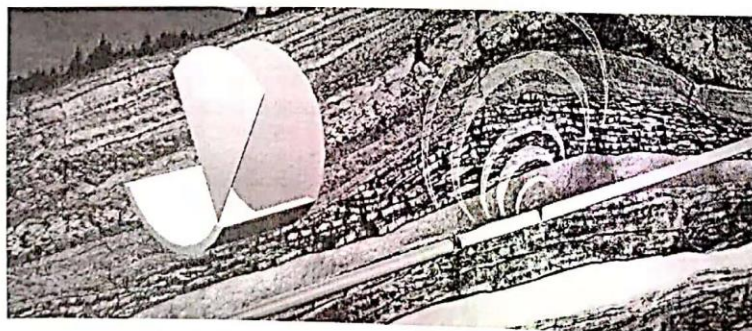


图 2.利用超宽带天线向井眼外发射瞬变脉冲

（3）对仪器在各种地层中对不同边界的响应情况进行研究，探索地层界面对

电磁波造成反射的机理。

为使得地质导向仪器能对地层边界做出准确判断，进而使钻杆在最佳地质目标内钻进，就需要仪器兼备足够的探测深度以及高分辨率。对不同地质特性的地层边界以及角度距离的地层边界进行建模仿真，研究瞬变信号波形、带宽等参数与探测深度分辨率之间的联系，对瞬变信号进行优化，并根据井眼、仪器的工业设计对电磁波收发装置进行优化改良。

(4) 结合仿真结果，研究针对瞬变信号地质导向技术的解释方法。

以通过计算机仿真得到的大量数据为基础，探索对测量数据进行时频分析的方法，研究地层边界与测量数据之间的对应关系，优化小波类型、尺度参数等。

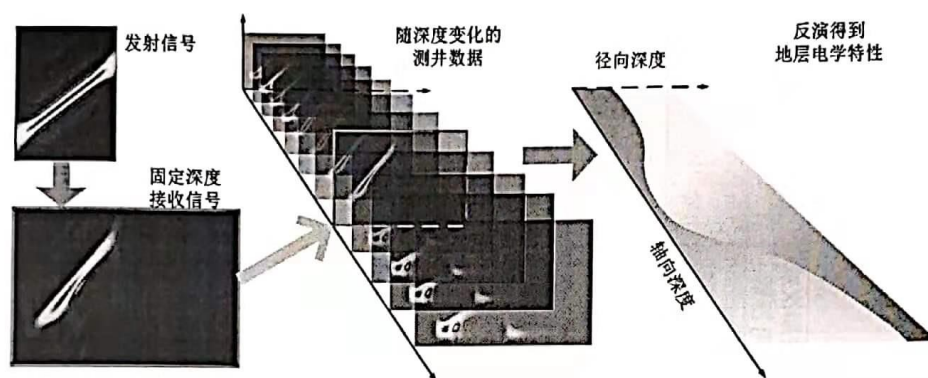


图 3.利用时频分析法对井眼外地层地质参数进行反演

三、主要成果目录和数据统计表

1、论文成果

序号	论文名称	第一作者	论文状态	发表期次或 录用日期	收录情况	标注 情况	期刊名称
1	Numerical Study on Complex Resistivity Measurement of Porous Media Containing Gas Hydrate	王斌	已录用	2017年11月	EI		PIERS2017

注：“论文状态”是指“已发表”或“已录用”，“已发表”论文放在前面，“已录用”论文排在后面；

“收录情况”是指被四大检索系统收录情况；

“标注情况”是指是否标有“中央高校基本科研业务费专项资金资助”（supported by “the Fundamental Research Funds for the Central Universities”）。

2、项目升级情况

序号	项目名称	项目编号	项目来源	经费（万元）	负责人	项目起止时间
1	天然气水合物储层宽频介电测井响应数值/物理模拟研究	41704124	国家自然科学基金	24	王斌	2018.01.01-2020.12.31
2	天然气水合物储层宽频介电测井响应机理及饱和度评价方法研究	ZR2017BEE026	山东省自然科学基金	9	王斌	2017.08.01-2019.12.31

3、其他成果

序号	成果名称	成果类型	成果等级	项目负责人 排名	成果编号	获得成果日期
1	近井眼地层的介电常数频散特性在宽频谱的连续测量方法	发明专利授权		1	201510885216.5	2017年11月
2	含天然气水合物多孔介质阻抗测量装置的仿真和解析方法	发明专利申请		1	2017111061908.3	2017年11月

4、项目成果数据统计表




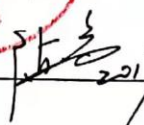
资助经费	资助总额	5 万元		研究期限	计划完成时间		2015.09-2017.09									
	实际支出金额	5 万元			实际完成年月		2015.09-2017.09									
学术交流	大会特邀报告 (篇)		分组报告 (篇)		邀请讲学 (次)		被邀请讲学 (次)									
	国际	1	国际		国际		国际									
	国内		国内		国内		国内									
	举办国际、国内学术会议次数及参加人数:															
发表论著	期刊发表 (篇)		论文集 (篇)		专著出版 (本)		编写教材 (本)									
	国际		国际	1	主编		主编									
	国内		国内		参编		参编									
	收录情况 SCI: 篇; EI: 1 篇; ISTP: 篇; ISR: 篇; 其它收录:															
发明专利	申请 (项)		已授权 (项)		国际 (项)	国内 (项)	经济效益 (万元)									
	2		1													
学术奖励 (获奖类别、等级、项数)	国 家 级				省 部 级											
	国际学术奖				其 它											
人才培养 (人)	博士后	博士 (已获学位)		硕士 (已获学位)		学士 (已获学位)										
	入选科技人才计划类别、次数:															
项目升级情况	本项目的延续研究获得上级部门资助情况 (项目类型、编号、名称、资助金额、研究期限等): 国家自然科学基金, 41704124, “天然气水合物储层宽频介电测井响应数值/物理模拟研究”, 24 万元, 2018.01.01-2020.12.31 山东省自然科学基金, ZR2017BEE026, “天然气水合物储层宽频介电测井响应机理及饱和度评价方法研究”, 9 万元, 2017.08.01-2019.12.31															

四、主要研究人员名单

序号	姓名	出生年月	职务/职称	工作单位
1.	王斌	1988.1	讲师	信控学院自动化系
2.	郭亮	1981.1	讲师	信控学院自动化系
3.	王圣杰	1992.3	在读硕士研究生	信控学院自动化系
4.	涂梦雨	1994.1	在读硕士研究生	信控学院自动化系
5.	刘亚伟	1993.5	在读硕士研究生	信控学院自动化系
6.				
7.				
8.				

(金额单位: 万元)

五、项目经费决算表

基于瞬变信号随钻电阻率地质导向的理论研究及设计			
项目名称			项目编号
项目负责人	王斌		15CX02120A
资助经费	5		剩余经费
			0
科 目	预算经费	经费支出	说 明
1、科研业务费	1.6	1.6	----
(1) 测试化验加工费			
(2) 出版/文献/信息传播/知识产权事务费	1.6	1.6	论文发表、查新和专利费, 以及购买图书、复印费
(3) 会议费/差旅费			
(4) 其他			
2、实验材料费	1.55	1.55	----
(1) 原材料/试剂/药品购置费	1.55	1.55	购买办公用打印机硒鼓2个, 用于数据存储硬盘6块, 升级计算机内存条等电脑配件, 打印纸等其他办公耗
(2) 其它			
3、仪器设备费	1.7	1.7	----
(1) 购置	1.7	1.7	购买高性能计算平台2台
(2) 试制			
4、国际合作与交流经费			
5、劳务费	0.15	0.15	研究生3人*0.05万元=0.15万元
6、专家咨询费			
合 计	5	5	----
财务部门 审核意见	  (公章) 2017 年 12 月 12 日		
审计部门 审核意见	  (公章) 2017 年 12 月 12 日		

六、项目负责人责任承诺:

本结题报告所填内容全部属实。

负责人(签字):

张武

2017 年 12 月 9 日

七、项目承担单位审查意见

负责人(签字):

王宇仁

公章

2017 年 12 月 20 日



八、学校自主创新科研计划领导小组审批意见

准予结题



负责人(签章):

郝芳

年 月 日

项目批准号：18CX02112A

中国石油大学（华东）
自主创新科研计划项目
计划任务书

项目名称：用于地层流体饱和度评估的脉冲介电测井仪器研究

项目类型：青年基金 项目亚类：一般项目

研究期限：2018 年 1 月至 2020 年 12 月

负责人：王斌 联系电话：18562872097

电子邮箱：wangbin2015@upc.edu.cn

依托院部：信息与控制工程学院

2018 年 1 月 10 日填

一、基本信息

负责人信息	姓 名	王斌	性 别	男	出生年月	1988.01
	最后学位	博士	授予时间	2015.06	职 称	讲师
	主要研究方向	电法测井、介电测井、介电常数测量				
	所属科研机构					
承担单位		信息与控制工程学院		合作单位		
项目信息	项目名称	用于地层流体饱和度评估的脉冲介电测井仪器研究				
	隶属学科	勘探地球物理学			批准金额(万元)	15
	项目类型	A.青年基金				
	起止时间	2018年1月至2020年12月				
	主题词(3个)	介电测井; 流体饱和度评估; 井眼天线				
	预期成果	<input checked="" type="checkbox"/> 专著、论文 <input checked="" type="checkbox"/> 专利 <input type="checkbox"/> 软件 <input type="checkbox"/> 样机、样品 <input type="checkbox"/> 其它				
项目组成员	姓名	所在单位	职称	本项目中承担的任务	签字	
	王斌	信息与控制工程学院	讲师	主持, 电磁仿真, 仪器搭建、调试, 理论推导	王斌	
	邢兰昌	信息与控制工程学院	副教授	电磁仿真、仪器搭建、测试	邢兰昌	
	郭亮	信息与控制工程学院	副教授	理论推导、电磁仿真	郭亮	
	张仲濠	信息与控制工程学院	研究生	仪器搭建、测试	张仲濠	
	张新铭	信息与控制工程学院	研究生	电磁仿真、理论推导	张新铭	
<p>项目摘要(限400字以内):</p> <p>宽频介电测井作为一种新型测井方法, 通过测量地层介电频散可提供流体饱和度等多种地质信息, 对稠油油藏、储层剩油评估等具有重要意义, 探索新的频散测量方法、分析测量机理是值得研究的课题。本项目提出利用超宽带瞬变脉冲作为探测信号, 以实现对地层介电频散特性在连续带宽下测量的新思路。首先, 探索宽带电磁脉冲在含流体地层的传播反射规律, 结合复模式匹配理论和时域数值方法分析电磁能量在井眼周围的分布特性, 揭示地层介电特性与仪器响应之间的内在联系, 研究新方法的正演、反演机制; 然后, 结合仿真与实验, 分析宽带信号的辐射、接收规律, 设计应用于新方法的井眼天线, 搭建参数优化的实验测井短节, 研究仪器在不同流体饱和度地层样本中的响应, 探索高效、准确的测井数据解释方法, 实现基于脉冲的宽频介电测井。本研究为基于瞬变脉冲的宽频介电测井新方法奠定理论基础, 为通过近井眼介电频散测量评估储层流体饱和度方法的发展提供新的思路。</p>						

注: 1. “承担单位”、“合作单位”填写负责人所在院部等二级单位; 2. 项目“隶属学科”填二级或以下学科; 3. 项目组成员“所在单位”填写所在院部等二级单位。4. 若为“研究生创新项目”, 则项目组成员中第一位应为其导师。

二、研究目标、主要研究内容

1. 研究目标

本课题立足于介电测井的国际前沿问题,提出一种基于脉冲的宽频介电测井方法,利用单次脉冲实现在宽频段对地层介电频散和介电信息的连续、完整测量,可大大简化频散测量的扫频过程。系统开展宽频带下电磁波在近井眼区域传播的物理过程分析,建立宽频介电测井的理论和硬件模型,揭示仪器探测地层参数的内在机理,结合 UWB 井眼天线研究,对仪器探测性能进行优化,设计、制作实验短节,并针对宽频方法提出基于时频分析的测井数据反演算法。为实现实时、高分辨率、可靠的地层流体饱和度评估奠定基础。

2. 主要研究内容

A、运用复模式匹配理论研究宽带脉冲在近井眼区域的传播特性,揭示宽频仪器对地层电学参数的响应机理。

为了揭示脉冲信号、地层参数和仪器响应之间的内在联系,我们将利用电磁场数值方法分析电磁波空间分布情况,同时引入复模式匹配理论,分析近井眼区域波导模式的特性,通过研究各个模式能量占总场强的比重,对宽带电磁脉冲在近井眼范围的传播特性进行研究,探索复杂泥浆侵入情况、井眼构成等因素对仪器探测性能的影响。

B、研究井眼中宽带脉冲的发射接收机制,设计并优化 UWB 井眼天线。

我们拟结合复模式匹配理论,探索井眼天线对宽带脉冲的发射机制,研究天线的激发场对于不同电磁波模式的耦合效率,针对仪器的探测需求,揭示发射天线结构与仪器探测范围之间的内在联系,完成对井眼天线的优化设计。

C、研究地层参数对仪器探测结果的影响机理。

通过数值模拟和物理实验考查改变宽频介电测井仪参数与地层参数对测井响应的影响规律。拟采用基于 GPU 加速的时域有限差分法来提高仿真效率,得到仪器在复杂地层中的响应,再结合复模式匹配理论对仪器响应受地层参数影响的机理进行探索。在得到优化参数的仿真结果基础上,搭建测试短节,配合实验室测试平台获取仪器在已标定电学参数的样本地层中的时域、频域响应,验证仿真结果的正确性。

D、在明确仪器探测过程的基础上,研究宽频介电测井响应的数值反演算法。

结合通过仿真与实验得到的时域、频域测井响应曲线,依据明确标定的地层电学信息,引入时频分析手段,创新地将二维测井信息扩展到时间-频率-深度三维空间,将隐含在原始测井数据中的地层信息提取出来,从而提高仪器分辨率,使仪器的宽频优势得到充分发挥,构建完整的近井眼介电信息反演方法。

三、预期成果及考核指标（预期成果及考核指标应切实可行，须量化可考核）

（1）掌握宽带脉冲在近井眼地层的传播辐射规律和 UWB 天线发射宽带脉冲信号的机制；

（2）建立适用于宽带介电测井的分析模型，揭示电磁波传播、地层参数与仪器响应、探测性能之间的内在联系，掌握仪器在复杂井眼环境中的测量机理；

（3）制造高性能的宽带介电测井短节样机；

（4）在国际、国内期刊发表学术论文 3 篇，其中 SCI 收录至少 1 篇，或 EI 收录至少 2 篇；

（5）授权发明专利 1 项；

（6）培养研究生 2-3 名；

四、项目研究进度计划

2018/01-2018/06 搭建测试超宽带井眼天线性能的测试平台，结合电磁场数值方法与物理实验优化设计天线参数。

建立电磁脉冲在金属钻铤外地层传播的数学物理模型，研究宽带电磁波的传播分布规律，获取复杂地层电磁波传导、辐射模式的数值解和解析解。

2018/07-2018/12 构建宽带天线在井眼环境中辐射电磁波的数学物理模型，结合电磁场数值分析与复模式匹配理论，获取模式空间下电磁能量的分布情况。

进而探索天线辐射场对地层中电磁波传播特性的作用机理。

2019/01-2019/06 对各种不同含流体饱和度的地层模型进行仿真，明确电磁波在地层中的传播规律与接收信号的内在联系。

根据前面正问题的仿真结果，搭建仪器响应的硬件测试平台。

2019/07-2019/12 通过实验考察各种不同的激励信号参数、地层参数、井眼参数等条件下获得的测井信号的特点。

将数值仿真与物理实验结果进行对照，在验证结果正确性的基础上，采集各种参数下获取的响应结果。

2020/01-2020/06 在大量物理实验和仿真结果的基础上，引入时频分析方法，研究宽频介电测井数据的解释方法，与地质参数对照验证其正确性，从而提高测井方法的分辨率和准确性。

2020/07-2020/12 考察各种异常情况对测井结果的影响，进一步修正仪器的设计与数据反演算法，总结研究工作，撰写论文，撰写结题报告。

五、经费预算表

(金额单位: 万元)

经费预算表

科目名称	申请经费	计算依据与说明(必填)
1、仪器设备费	4	
(1) 购置	4	用于购置梳状波发生器、脉冲信号源、频谱分析模块等
(2) 试制		
(3) 维修、租赁		
2、实验材料费	4	用于购置测试短节用材料、连接线、连接头等改造测试平台用气体导管、转接口、流量阀等
3、测试化验加工费		
4、差旅费	3	用于参加国内学术会议、样本及仪器测试、调研所产生的差旅费
5、会议费		
6、国际合作与交流费		
7、出版物/文献/信息传播费/知识产权事物费	2	申请专利、发表论文购买图书文献等所产生费用
8、劳务费	2	支付直接参与研究的研究生之劳务费
9、专家咨询费		
10、其它		
合 计	15	

注: 资助经费不得购置常规性办公耗材或用品, 不得购置通用性办公设备(如计算机、打印机等)。

六、计划任务书各方签约

1. 项目负责人承诺

本人确认本计划任务书及附件内容真实、准确。将严格按照《中国石油大学（华东）自主创新科研计划项目管理办法（试行）》与本计划任务书的规定，认真履行项目负责人职责，积极组织开展研究工作，合理安排研究经费，按时报送有关材料并接受检查。若在项目执行过程中违反有关规定，本人将承担全部责任。

负责人（签字）：

2018 年 1 月 11 日

2. 承担单位及合作单位承诺

（1）承担单位

已经按照学校有关规定与项目申报要求对计划任务书内容进行了审核。我单位将根据项目研究内容，落实项目研究所需条件；认真履行项目承担单位的管理职责。

负责人（签字）：

2018 年 1 月 11 日

（公章）

（2）合作单位

同意参加合作研究，将按照学校有关规定，认真履行项目合作单位的管理职责。

负责人（签字）：

（公章）

年 月 日

3. 科技处审核意见



负责人（签字）：



年 月 日



（公章）

4. 学校自主创新科研计划领导小组审批意见



负责人（签字）：



年 月 日



中国石油大学（华东）
青年教师教学改革项目申请书

项 目 名 称：面向测控专业的科研案例式《电
磁场与微波技术》课程教学研究
与探索

项目主持人：王斌

所 在 单 位：信息与控制工程学院

联 系 电 话：18562872097

电 子 邮 箱：wangbin2015@upc.edu.cn

申 报 日 期：2018 年 3 月 19 日

教 务 处

一、简表

项目	名 称	面向测控专业的科研案例式《电磁场与微波技术》课程教学研究与探索											
	起止时间	2018 年 5 月-2020 年 5 月			预期成果	1 建立面向测控专业的《电磁场与微波技术》案例式教学体系； 2 完成案例式教学课程讲义编写、完善多媒体课件； 3 教学研究论文 1-2 篇(核心期刊 1 篇)。							
项目 申 请 人	姓 名	王斌		性别	男	民族	汉族	出生年月	1988.01				
	专业技术职务			讲师		最终学历 / 学位		博士					
	主要教学工作简历	时 间	课程名称		授课对象		学时	所在单位					
		2018.03	测量仪表与自动化		建环 16 级 1-2 班		26	信控学院					
		2017.09	化工仪表		化工 15 级 1-3 班		24	信控学院					
		2017.09	化工仪表		化工 15 级 4-6 班		24	信控学院					
		2017.09	测控技术与测控网络系统		测控 14 级 01-02 班		32	信控学院					
		2017.03	测量仪表与自动化		建环 15 级 1-2 班		26	信控学院					
		2016.09	测控技术与测控网络系统		测控 14 级 01-02 班		32	信控学院					
		2016.03	过程控制仪表与装置		自动化 13 级 1-2 班		8	信控学院					
		2015.09	化工仪表		化工 13 级 1-3 班		8	信控学院					
	相关教学研究项目和成果	时 间	项目或成果名称				在研、结题情况及排名						
		2015.09-2017.09	工程教育专业认证背景下《传感器原理》课程双语教学体系研究				结题第六						
		2018.02	教学研究论文：《实验技术与管理》含天然气水合物多孔介质电参数测量系统仿真实验研究				审稿中第一						
项目组主要成员 (不含主持人)	姓名	年龄	职称	专业	承担任务		单位	个人签名					
	邢兰昌	35	副教授	测控计量技术与仪器	为制定课程教学目标、梳理教学内容提		信控学院						
	潘浩	38	讲师	测控计量技术与仪器	案例库建设,教学效果评价方法研究		信控学院						
	马士腾	29	实验师	自动化	讲义、课件制作,教学内容梳理		信控学院						
其它人员													

二、背景和意义

1、国内外研究现状

《电磁场与微波技术》这门课程是高等院校电子信息工程、通讯工程、电子科学与技术等专业的重要专业课程之一。该课程主要包括：矢量分析、静态电磁场、时变电磁场、平面波、导行波、传输线理论、微波网络基础、天线等知识[1-2]。主要培养学生运用场的观点对工程电磁问题进行分析 and 计算，完成学生对电磁场与电磁波的理论概念建立，让学生掌握对电磁场电磁波的分析方法[3]。

《电磁场与微波技术》的教学与学习具有以下特点：随着信息时代的发展，作为信息主要载体、重要检测手段的微波技术，不仅在计算机、卫星通讯、雷达等传统行业继续发挥重要作用，而且被广泛应用到遥感检测、矿藏探测、量子通讯等众多高新技术领域，同时，在人们的日常生活中也扮演了重要角色。因此，《电磁场与微波技术》正在成为电子专业以外如测控专业类学生在目前以及今后都是不可缺少的主干专业课程[4]。然而，它的前续课程如高等数学、大学物理等都较为抽象，加之课程本身推导过程繁琐、概念抽象、理论性强、涉及知识点多且杂，学生往往缺乏感性认识，往往对这门课程，教师感到“难教”，学生感到“难学”，而这一状况与无线电技术高速发展，国内外对微波、电磁测量等领域人才的迫切需求产生了矛盾[5]。

案例教学法是教师组织学生通过对案例的调研，思考，分析和实践的活动，加深学生对理论的理解，激发学生学习兴趣，提高学生分析解决问题的能力[6-7]。现代案例式教学是 1901 年最早应用于哈佛大学的法学和医学专业教学，20 世纪初，开始应用于管理专业的教学，内容、方法、经验日趋丰富和完善，并在世界范围内产生了巨大影响[8]。在我国，案例教学法从 20 世纪末开始被应用到理工科专业课教学中[9-13]，在《电磁场与微波技术》课堂教学中应用案例式教学法的探索最早开始于 2005 年左右，在随后不断探索中，面向不同专业背景、专业的学生，因材施教[5]。针对电力专业学生，通过引入电击穿、电磁加热案例，讲解涡流、趋肤效应等概念[14]；针对煤炭相关专业学生，引入矿井通讯、煤岩破裂电磁辐射问题[15]；针对通讯专业学生，引入广播天线极化问题等[16-17]。电磁场与电磁场理论中有许多基础性和探索性问题，是创新型教学改革的好典范，在教学过程中引入科研项目导向或工程导向的教学实践，学生整体水平得到显著提高，对电磁场的理解更加透彻，参加电磁学相关竞赛和毕业设计的学生数量明显增加，也从侧面说明此教学方法在提高《电磁场与微波技术》教学效果和调动学生积极性上成效显著[18]。

综合案例教学法在国内的发展,以及在《电磁场与微波技术》课程教学的应用,与传统以教师为主导的教学法相比较,案例教学法有以下几个方面优势:更加注重学生的主体性和自主性的发挥,在力图对一个问题寻求多种解决方案的过程中,培养和形成创造性思维;有利于提高学生分析问题和解决实际问题的能力;有利于促使学生培养良好的探索性思维习惯;可以促进学生的沟通和交流。

然而,总的来说针对《电磁场与微波技术》课程的案例式教学还处于起步阶段,尚无针对测控技术与仪器等检测类专业的案例式教学报道,仍有许多问题等待探索研究:

〈1〉案例库资源不足。缺少适合测控技术与仪器专业的案例,例如电磁传感器、遥感类的案例非常匮乏。

〈2〉案例教学的反馈评价机制有待完善。在教学过程中虽强调以学生为主体,但实际操作中还是以教师讲解为主,对学生创新能力培养不足。

〈3〉缺乏针对《电磁场与微波技术》课程案例式教学的教案及多媒体教学方法。

2、研究意义

实践证明,若能恰当的运用实例教学法,往往能收到事半功倍的教学效果,《电磁场与微波技术》在工程实践和日常生活诸多领域中有着广泛应用。在教学过程中,要让学生把课程中概念和规律表示清楚,需要很好的空间想象力和扎实的数学基础,学生往往会有畏难情绪,加之教材中很少有实际应用的例子,尤其测控技术与仪器专业课程以传感器原理、检测仪表等为主,繁杂的理论学习若不结合实际应用,往往令学生看不到微波技术的应用前景,学习积极性不高,影响了教学效果。

在我校对测控技术与仪器专业新修订的培养计划中,《电磁场与微波技术》成为该专业学生大二下学期的专业课程。在对测控专业学生进行《电磁场与微波技术》课程教学中,教师若能结合测控专业特点运用案例式教学法,结合科研项目或工程实践,将与微波检测技术相关的实际案例通过演示实验使学生了解应用背景,再将问题交给学生分析,结合仿真软件让学生动手完成仿真实验,最后在课上针对各自结论进一步剖析,对相关案例进行总结。会使学生从实例中得到启迪,对虚拟的电磁场概念形成形象认知,达到举一反三、独立解决问题的目的,同时弥补了教材的不足,使学生从繁琐的公示记忆中摆脱出来,解决实际工程问题的能力也得到提高。同时完善面向测控类专业《电磁场与微波技术》课程教学的教案及多媒体教学手段,积累相关经验,为全面提高学生解决复杂工程问题的能力打下基础,为建成符合工程教育专业

认证的《电磁场与微波技术》课程体系提供支持。

3、参考文献

- [1] 田雨波, 张贞凯. “电磁场理论”教学改革初探[J]. 电气电子教学学报, 2008, 30(1):11-13.
- [2] 叶宇煌. “电磁场与微波技术”课程设置初探[J]. 高等理科教育, 2003(s1):124-125.
- [3] 曾军英, 甘俊英, 应自炉, 等. 基于卓越工程师背景下的电磁场与微波技术课程教学优化实践[C]// 教学管理与课程建设学术会议. 2012.
- [4] 袁国华, 李九生, 申屠南瑛, 等. “电磁场理论与微波技术”精品课程建设与教学实践[J]. 中国电力教育, 2012(8):51-52.
- [5] 王士彬, 张莲, 万沛霖, 等. “电磁场”课程教学内容改革的实践[J]. 电气电子教学学报, 2006, 28(5):8-11.
- [6] 张家军, 靳玉乐. 论案例教学的本质与特点[J]. 中国教育学刊, 2004(1):48-50.
- [7] 郑金洲. 案例教学指南[M]. 华东师范大学出版社, 2000.
- [8] 郑金洲. 案例教学:教师专业发展的新途径[J]. 教育理论与实践, 2002(7):36-41.
- [9] 雷海艳. 浅谈现代案例教学模式[J]. 长春理工大学学报:社会科学版, 2007, 20(1):28-30.
- [10] 李景鹤. 化工原理课案例教学的探讨[J]. 大连理工大学学报(社会科学版), 1995(2):40-42.
- [11] 刘金华. “数字电子技术基础”课程引入案例教学的探讨[J]. 湖北理工学院学报, 2009, 25(4):57-59.
- [12] 马慧. 案例教学在大学物理教学中的研究与实践[D]. 湖南大学, 2009.
- [13] 谢志江, 孙红岩, 蒋和生, 等. 案例教学法在工科教学中的应用[J]. 高等工程教育研究, 2003(5):75-77.
- [14] 张爱清, 叶新荣, 丁绪星. 实例教学法在“电磁场与电磁波”教学中的应用[J]. 中国电力教育, 2010(12):63-64.
- [15] 张剑英, 郭秀兰, 李诗华. “电磁场理论”课程教学中两个实例的应用[J]. 电气电子教学学报, 2005, 27(2):30-32.
- [16] 任仪, 郝宏刚, 尹波. 基于工程案例的《电磁场与电磁波》教学实践[J]. 读写算:教师版, 2012(11):69-70.
- [17] 马愈昭, 许明妍, 范懿. 电磁场与微波技术课程的三种特色教学手段[J]. 武汉大学学报(理学版), 2012(s2):109-112.
- [18] 莫锦军. CST 仿真实例在电磁场与电磁波教学中的应用[C]// 教育部中南地区高等学校电子电气基础课程教学研究会学术年会. 2014.

三、研究内容、方案和进程

(一) 研究内容和拟解决的关键问题

1、研究内容

(1) 面向测控专业以电磁检测为应用背景的案例库建设。

在针对测控技术与仪器专业开设的《电磁场与微波技术》课程中，要引入以案例教学为基础的教学方法改革，建立完备、合理的案例库是前提。如果要使案例教学发挥最佳效果，案例库的建立需要与测控技术与仪器专业背景紧密集合，需要对以下问题进行深入探讨：(a) 明确通过案例教学进行《电磁场与微波技术》的教学目标；(b) 如何与测控专业课程体系紧密联系；(c) 如何在案例教学中使学生有效地、高效地掌握课程理论内容。

(2) 面向测控专业案例教学的反馈机制和教学目标达成度评价机制建设。

考试是总结性评价方式的典型方法，虽然在考试试卷的信度和效度较高的条件下能够对整个学习过程进行检验，在一定程度上能够表示出课程目标的实现程度，但往往在评价学生在学习本门课程后获得的创新能力和实践能力提高方面，成效甚微。案例式教学是伴随理论教学同步进行的，教师在进行教学方法改革时，应关注形成性评价方式，建立完善的反馈机制，能够对尚未达到要求的学生及时地发现问题并予以有步骤地矫正，对已经达标的学生进行强化和鼓励，从而实现全体学生的学习效果。同时，完善针对测控专业案例教学的目标达成度评价机制建设，将案例教学的评价得分，纳入最终教学目标达成度评估中，使案例教学效果最大化。

(3) 完成针对测控专业的《电磁场与微波技术》教案编写，建立相应的多媒体演示教学体系。

《电磁场与微波技术》课程的静电场、平面波、导行波、天线等内容部分，均适合引入案例并结合案例完成理论教学，从而使原本难教、难学的理论知识变得简单有趣，同时锻炼学生独立解决问题的能力。因此，需要在案例库和对学生接受能力进行科学评估的基础上对教学内容进行梳理和筛选，特别是针对测控专业学生的知识背景，制定专门的教案。《电磁场与微波技术》课程中引入的案例，可与教师科研项目相结合，使学生接触学科前沿的同时，完成理论学习，为使得案例教学过程生动易懂，应建立相对应的多媒体演示教学、交互体系，提高案例教学效果。

2、拟解决的关键问题

(1) 以课程教学目标达成度评价为导向的案例库反馈机制的建立

可以将课程的案例教学过程和案例库的持续改进过程与一个自动控制系统相类比，即教学过程和案例库建设为前向通道、以目标达成度评价为导向的动态调整为反馈通道。只有反馈通道能够及时准确地获取前向通道的输出，并且能够与设定的目标进行负反馈，才能保证此“控制系统”的稳定性。获取前向通道的输出和与设定目标进行比较而形成负反馈的物理过程分别对应教学目标达成度评价的跟踪机制和跟随案例教学同时进行的适时调整机制两个方面。此跟踪机制和反馈机制的建立是本项目拟解决的第一个关键问题，同时也是重点和难点问题。

(2) 测控专业特色与《电磁场与微波技术》课程内容的契合

如果要使案例教学发挥最佳，案例库的建立需要与测控技术与仪器专业背景紧密结合，需要明确通过《电磁场与微波技术》教学对测控专业学生培养目标实现的帮助是什么，在目标导向的基础上，结合测控专业特色，深入探索如何将案例库建设、案例教学开展与测控专业课程体系紧密联系，如何使学生在学习本门课程效果最大化的同时，完成学生解决复杂工程问题能力的培养。在此基础上，选择与之相适应的案例教学手段，结合两者的契合点对《电磁场与微波技术》各章节内容的性质和特点进行分析，进而对所选定的案例库、教学手段进行适当调整，从而为取得较好的案例教学效果提供保证。因此，寻找测控专业与课程内容的结合点为本项目需要解决的第二个关键问题。

(3) 测控专业教师讲授水平和面向测控专业课程教学资源的设计

教师是课堂案例教学的组织者和实施者，在案例教学过程中起主导作用，主要体现在案例库的建设、案例背景的分析展开、对学生的引导等方面，这要求教师在对《电磁场与微波技术》课程内容本身非常熟悉的基础上，结合测控专业背景和学生特点，综合运用案例教学法，让学生更容易接受原本枯燥的理论知识，教师的讲授水平是能否取得好的案例教学效果的关键。课程讲义、教案以及多媒体教学手段，是辅助教师开展案例式教学的工具，经过对测控专业工程专业认证背景下培养方案的研究，目前尚未发现适合我院测控专业《电磁场与微波技术》课程的成型教材，也无面向测控专业的案例式教学研究相关报道。在案例教学改革的过程中，课件与讲义质量的高低直接影响着教师课堂授课与学生课下针对案例学习的效果。因此提高测控专业教师在本门课的授课水平、完善讲义、课件建设，为建立本专业《电磁场与微波技术》案例式教学体系需要解决的又一个关键问题。

（二）改革方案设计和解决问题的方法

本项目针对面向测控技术与仪器专业开设的《电磁场与微波技术》课程开展基于案例教学法改革的探索与实践，提出以培养学生解决复杂工程问题能力为教学目标，结合教师科研项目、测控专业应用背景，引入传感器、检测等应用实例，建立课程教学案例库。完成案例教学法的《电磁场与微波技术》教案讲义撰写，探索案例教学过程中应用多媒体交互手段的方法，最终，通过建立每个案例教学小周期的反馈机制，以及最终建立基于成果、学习效果的课程教学目标达成评价机制，通过开展教学实践、学习效果评价和教学目标达成度评价来获得教学目标达成度，进而应用教学目标达成度指标对教学体系形成反馈以实现持续改进机制，从而完成《电磁场与微波技术》案例教学课程建设与持续改进的闭环，最终形成一套符合测控专业发展要求和工程教育专业认证标准的《电磁场与微波技术》课程案例教学体系。

本项目研究方案的设计如图 1 所示：

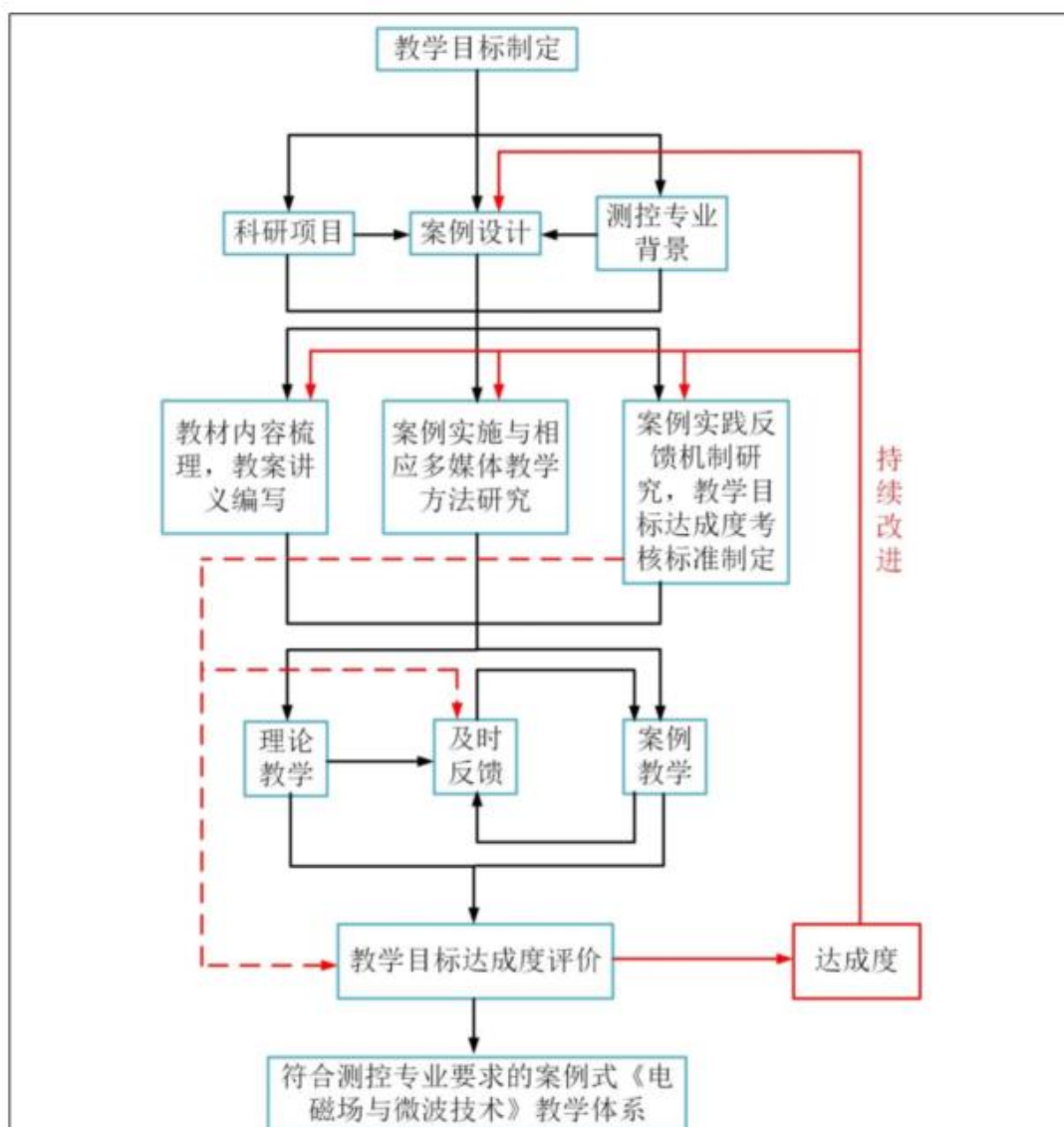


图 1 研究方案设计

研究方案中解决问题的步骤和方法具体说明如下：

(1) 以测控专业教学目标为导向的《电磁场与微波技术》案例库建设

第一步，查阅工程教育认证相关的文献资料，研究目前最新的测控技术与仪器专业认证的通用标准，根据专业的毕业要求和培养目标制定《电磁场与微波技术》课程的教学目标；

第二步，结合测控专业背景特点、本专业学生未来发展动向、授课教师科研项目，初步制定面

向测控专业的《电磁场与微波技术》案例库：

第三步，以测控专业教学目标为导向的《电磁场与微波技术》案例库持续改进机制。

(2) 完成《电磁场与微波技术》案例教学教案编写，建立案例教学目标达成度考核标准。

第一步，针对课程教学目标对学生接受能力进行评估，具体可采用如下手段：调查学生的大学物理、模拟电子技术和数字电子技术的学习成绩、选择有代表性的学生进行课前座谈；

第二步，对教学内容进行筛选和梳理，将《电磁场与微波技术》课程内容以及对应案例库案例分为两类——基础理论类（如矢量计算、麦氏方程等）和应用原理类（如导行电磁波、极化磁化、天线等），依据教学大纲和教学目标对各章节知识点的性质和特点进行梳理，为每一个知识点和案例设定教学方法，并依据实际情况注意多种案例融合和交叉使用；

第三步，确定板书和多媒体课件的分工和设计原则，确定板书和多媒体课件各自承载的内容，如板书内容包括内容提纲、演示软件编写等，然后完成教案编写、多媒体课件的详细设计；

第四步，梳理教学过程中的几项指标作为评价点，探索科学合理的形成性评价具体方法，如形成性测验、案例完成成果检查、随堂成果汇报、课堂演讲等，建立案例教学目标达成度考核标准。

(3) 进行理论、案例教学的同步实践，完成案例教学的动态跟踪、调整。

第一步，以理论教学的作业、随堂测试等教学效果为指导，收集案例教学中的形成性和总结性评价结果和相关材料作为事证，采用一定的评价工具，如量规（Rubric）对事证进行分析；

第二步，以分析结果为指导，对案例教学进行动态跟踪，及时发现不足，建立案例教学的及时反馈、动态调整闭环机制。

(4) 基于学习效果评价结果的教学目标达成度评价机制。

第一步，丰富总结性评价方法，结合最终报告、大作业、案例总结等，以教学目标为导向，建立弹性灵活的教学目标达成度评价机制；

第二步，结合达成度评价结果，对案例库、教学资源、达成度评价本身持续改进，最终形成具有闭环反馈、自我完善功能的《电磁场与微波技术》案例式教学体系。

<p>（三）创新点和预期成果（包括成果形式等）</p> <p>1、创新点</p> <p>（1）提出以教学目标为导向，面向测控专业的《电磁场与微波技术》案例式教学体系，结合测控专业背景和科研项目，建立适合测控专业的案例库，并引入闭环反馈体质，最终形成一套完善的案例式教学体系。</p> <p>（2）提出基于教学目标达成度评价的教学方法动态调整模式，即首先结合教学目标建立案例库，初步确定与之适应的教案、多媒体教学手段等，然后在教学实践中不断进行教学效果反馈，及时对案例教学进行调节，并最终结合教学目标达成度，实现案例库、教学资源的持续更新、改进。</p> <p>2、预期目标</p> <p>（1）建立面向测控专业的《电磁场与微波技术》案例式教学体系（研究报告、论文）；</p> <p>（2）完成案例式教学课程讲义编写、完善多媒体课件；</p> <p>（3）教学研究论文 1-2 篇（核心期刊 1 篇）。</p>
<p>（四）实施范围和推广应用价值</p> <p>1、实施范围</p> <p>2017 版及以后的测控专业本科培养方案在大二下学期新设置《电磁场与微波技术》课程，首次开课时间为 2018-2019 学年第二学期，在此之前并无任何教学资源、经验可循。本项目的理论研究成果将来可直接用于指导 2017 级及之后的测控专业《电磁场与微波技术》课程的教学实践，教学实践结果也用于为理论研究提供基础资料。</p> <p>本项目研究采用工程教育认证理念和参照认证标准对《电磁场与微波技术》课程进行案例教学的改革与实践，保证了改革方向的正确性和课程建设的规范性，为将来开展测控专业的工程教育专业认证提供支撑。</p> <p>2、推广应用价值</p> <p>本院自动化专业、电子信息工程专业、电气工程专业培养方案中设置了《工程电磁学》课程，与测控专业开设的《电磁场与微波技术》同属无线电微波类课程，具有理论体系相似，原理相通的特点。本项目针对测控专业进行的《电磁场与微波技术》案例式教学改革实践，可为本院其他专业面向专业认证的《工程电磁学》教学方法改革提供基础和借鉴。同时为其他高校测控专业的《电磁场与微波技术》或类似课程的改革提供理论支持。</p>

（五）项目研究进程安排

本项目执行期为两年，以下分四个阶段（每6个月为一阶段）制定研究进程：

第一阶段：

参照最新的测控专业认证标准，提出针对测控专业的《电磁场与微波技术》案例式教学目标，制定面向测控专业背景的案例库建设指导原则，进一步完善教学内容的筛选和梳理。

第二阶段：

完成以测控专业教学目标为导向的《电磁场与微波技术》案例库建设，依照课程教学目标、教学内容筛选和梳理情况，完成《电磁场与微波技术》案例教学课程讲义的编写；建立基于诊断性评价和形成性评价的教学方法动态调整模式；围绕具体案例进一步细化、完善板书和多媒体课件的设计与课件的制作。

第三阶段：

开展理论教学、案例式教学的同步实践，结合诊断性动态反馈机制，对案例教学模式及时改进、完善，完成教学目标的达成度评价，并对达成度结果进行详细分析。

第四阶段：

结合达成度评价结果，完成对案例库、教学资源的持续改进，初步建立面向测控专业的《电磁场与微波技术》案例式教学体系，完成研究报告、教学论文的撰写。

四、研究基础

项目组成员已进行过的相关研究

1、项目申请人（王斌）

（1）申请人硕博专业均为无线电物理（山东大学），主修课程包括《电动力学》、《微波技术与天线》、《高等电磁学》、《计算电磁学》等电磁场相关专业课程，**在专业知识、技能应用等方面具有较好基础。**

（2）申请人主讲《测量仪表与自动化》、《化工仪表》等检测类课程，作为主要参与人参加了工程教育专业认证背景下《传感器原理》课程双语教学体系研究等校级教改项目，熟悉测控技术与仪器专业背景、培养方案，参与 2017 级工程教育专业认证下的测控技术与仪器专业培养方案制定，并主笔《电磁场与微波技术》课程教学大纲。主持国家自然科学基金、山东省自然科学基金等多项科研项目，科研内容涵盖电磁波测井、介电常数检测、电阻率检测等电磁场微波检测相关背景。**目前积累了一定的教学资源，如讲义初稿、教案、参考资料等。**

（3）申请人作为第一作者已投稿教学研究论文一篇，论文题目和摘要如下：

题目：含天然气水合物多孔介质电参数测量系统仿真实验研究

摘要：为使学生接触专业科研前沿，更好地培养学生科研能力、创新意识，以科研项目中的天然气水合物在多孔介质中生成、分解过程研究为背景，将含水合物介质电参数测量系统开发中的部分研究内容引入到实验教学当中，设计了基于有限元数值方法的含水合物多孔介质电参数测量的仿真实验。基于实际反应釜及复电阻率测量装置，建立数值模型；采用全波有限元方法，对模型中的电磁场进行仿真计算，获得空间电磁分量分布；通过设置不同尺寸的水合物，结合仿真结果后处理方法，得到不同的水合物分布对应的视电学参数。通过该实验可使学生熟悉电磁场的基本知识，学习有限元电磁仿真的建模、参数设置、结果分析等方法，有利于培养学生的科学探索精神，也为实际科研项目的开展提供技术参考。

2、项目组主要成员

邢兰昌

主持工程教育专业认证背景下《传感器原理》课程双语教学体系研究等校级教改项目一项，发表教学研究论文《实验课双语教学探索与实践》、《跨专业教学方法与特点的探讨》、《电-声-热多参数联合测试系统开发》三篇。

潘浩

主持和参加了《测量仪表与自动化》校级精品课程建设，《传感器与检测基础》研究性教学模式探索、工程教育专业认证背景下《传感器原理》课程双语教学体系研究等校级教改项目，在教学内容、教学方法、考试改革等方面进行了相关研究。

马士腾

参与教改项目《基于 OPC UA 远程虚拟仿真模型库》、《控制系统执行器特性测试系统开发》、《构筑跨专业智能汽车竞赛平台，提升大学生创新能力的研究与实践》。参与虚拟仿真培训系统开发一项，负责常减压、加氢等装置监控界面及交互功能开发，同时负责管理软件开发。

中国石油大学(华东)教务处

教学〔2018〕16号

关于公布2018年 校级教学改革项目名单的通知

各教学学院部、有关单位：

为进一步深化教学改革，不断提高人才培养质量，学校组织开展了2018年教学改革项目立项工作。经教师申报、单位推荐和专家评审，共确立各类教学改革项目220项，其中常规教学研究与改革项目121项（重大项目5项，重点项目20项，一般项目96项），专项教学改革项目99项（研究性教学方法改革项目12项，混合式教学方法改革项目15项，考试改革项目12项，青年教师教学改革项目30项，教学实验技术改革项目30项），现将名单予以公布，并就有关事项通知如下：

1. 学校依据《中国石油大学(华东)教学改革项目管理办法》，对立项项目提供经费支持，并着重做好重大项目和重点项目的管理工作。

2. 各教学学院部要做好一般项目和专项教改项目的立项启动、中期检查和结项验收工作，加强对项目的检查和指导。

3. 各项目组要按照立项任务书要求，认真开展项目研究与改革，确保各项目如期完成预定任务和目标。

教务处

2018年5月7日

附件5 青年教师教学改革项目名单

项目编号	项目名称	负责人	主要完成单位
QN201801	基于 MATLAB 平台的《数字图像处理》课程教学实践	王 斌	地球科学与技术学院
QN201802	基于 BOPPPS 框架的科研资源辅助教学模式研究与实践——以《渗流力学》(双语)课程为例	孙晓飞	石油工程学院
QN201803	石油工程微流控创新实验平台的构建与实践	姚传进	石油工程学院
QN201804	工程流体力学植入 CFD 教学探索与实践	刘玉泉	石油工程学院
QN201805	基于 5E 理论的渗流力学教学模式改革与实践	刘永革	石油工程学院
QN201806	化工安全方向专业课教学数字资源库建设	平 平	化学工程学院
QN201807	工程教育认证理念引导下的流态化工程课程教学改革与实践	朱丽云	化学工程学院
QN201808	新工科范式下项目驱动的精密机械设计工程教学研究	纪佳馨	机电工程学院
QN201809	基于仿生无人机的多学科交叉融合人工智能人才培养模式探索与实践	罗 德	机电工程学院
QN201810	基于移动学习的专业外语混合教学模式研究及资源建设	黄梦婕	机电工程学院
QN201811	兴趣驱动下以强化学生实践能力为导向的设计心理学多元化教学方法改革	刘旭堂	机电工程学院
QN201812	面向创新型人才培养的车辆工程专业实验教学体系研究	孙少华	机电工程学院
QN201813	面向测控专业的科研案例式《电磁场与微波技术》课程教学研究与探索	王 斌	信息与控制工程学院
QN201814	适应新工科理念的“工程热力学”混合式教学探索与实践	张秀霞	储运与建筑工程学院
QN201815	基于 VR 技术的储运生产实习方案研究	陈 雷	储运与建筑工程学院
QN201816	基于 LIPRI 的卓越《软件需求工程》成果驱动全英文教学改革	卢清华	计算机与通信工程学院
QN201817	《云计算技术与应用》的 PBL 教学模式探索与实践	王 勃	计算机与通信工程学院
QN201818	对分课堂在全英文专业课程中的实践应用	王芳芳	经济管理学院
QN201819	以应用为导向的《胶体与界面化学》互动式教学研究	王秀凤	理学院
QN201820	基于案例和项目学习的《数学实验》课程教学改革	张 健	理学院
QN201821	“需求定制式”化学综合实验课程建设与实践	温聪颖	理学院
QN201822	《高等数学》数值实例库建设	梁锡军	理学院

6.7 参与校级教改项目（QN201516）

项目编号: QN201516

中国石油大学（华东） 青年教师教学改革项目申请书

项 目 名 称: 工程教育专业认证背景下《传感器原理》
课程双语教学体系研究

项目主持人: 邢兰昌

所 在 单 位: 信息与控制工程学院

联 系 电 话: 18561597851

电 子 邮 箱: xinglc@upc.edu.cn

申 报 日 期: 2015-09-05

教 务 处

一、简表

项目	名 称	工程教育专业认证背景下《传感器原理》课程双语教学体系研究						
	起止时间	2015.09-2017.09		预期成果		(1) 面向测控专业工程教育专业认证标准的《传感器原理》双语教学体系; (2) 完成双语课程讲义编写、完善多媒体课件; (3) 教学研究论文 1-2 篇 (核心期刊 1 篇)。		
项 目 申 请 人	姓 名	邢兰昌	性 别	男	民 族	汉	出生年月	1983.02
	专业技术职务		讲 师		最终学历 / 学位			博 士
	主要教学工作简历	时 间	课 程 名 称		授 课 对 象		学 时	所 在 单 位
		2015.03	传感器原理 (双语) (新开课)		测控 13 级 1-2 班		40	信控学院
		2014.09	电机与电器 (全英文) (新开课)		电气国际班 13 级		48	信控学院
		2014.09	现代测试技术		测控 11 级 1-2 班		40	信控学院
		2014.05	测量仪表与自动化		建环 11 级 1-2 班		26	储建学院
		2013.12	学科前沿知识专题讲座		测控 10 级 1-2 班		2	信控学院
		2013.07	测控、自动化专业导论		自 12 级 1-3 班 测控 12 级 1-2 班		4	信控学院
		2012.12	成分分析仪表		自 09 级 1-4 班 测控 09 级 1-2 班		8	信控学院
		2012.06	自动化仪表与 DCS		自 09 级 1-4 班		4	信控学院
		2012.04	传感器与检测基础		自 09 级 1-4 班		8	信控学院
相关教学研究项目和成果	时 间	项目或成果名称					在研、结题情况及排名	
	2015.04 2013.05	教学研究论文: 《传感器原理及应用》实验课双语教学探索与实践 《测量仪表与自动化》跨专业教学方法与特点的探讨					第一作者 第一作者	

项目 组 主 要 成 员 (不含主持人)	姓名	年龄	职称	专业	承担任务	单位	个人签名
	耿艳峰	46	教授	控制科学与工程	为制定课程教学目标、梳理教学内容提供指导	信控学院	
	华陈权	44	副教授	测试计量技术与仪器	教学内容梳理	信控学院	
	石天明	58	教授	检测技术与自动化装置	双语教学方法 和学习效果评价方法研究	信控学院	
	鄢志丹	32	讲师	测试计量技术与仪器	英语参考资料整理	信控学院	
	王斌	28	讲师	无线电物理	讲义和课件的文字校对、图片美化、动画制作	信控学院	
其它 人员							

2015 年学校青年教师教学改革项目名单

项目编号	项目名称	负责人	所在单位
QN201501	工程教育认证环境下MOOC平台与课堂相结合的教学模式探索	宋 璠	地球科学与技术学院
QN201502	基于互联网研究性学习的原子核物理课程教学模式改革研究与实践	王新光	地球科学与技术学院
QN201503	翻转课堂教学模式下《岩石力学》(双语)教学改革研究	黄 勇	石油工程学院
QN201504	水电模拟渗流实验教学改革创新	付帅师	石油工程学院
QN201505	参与式教学在全英文课程《化学原理二》中的实践探索	贾 寒	石油工程学院
QN201506	基于MOOC理念的石油炼制工程微课资源建设	宁 汇	化学工程学院
QN201507	Seminar 教学模式在高分子化学本科教学中的探索与实践	夏 薇	化学工程学院
QN201508	化工安全与环保翻转式教学方法探讨与实践	韩丰磊	化学工程学院
QN201509	过程装备控制虚拟仿真创新实验教学平台建设	张 兰	化学工程学院
QN201510	基于微信公众平台的安全监测与监控课程辅助教学平台设计与适用性研究	王明达	机电工程学院
QN201511	机械完整性检测双语课程建设与探索	殷晓康	机电工程学院
QN201512	基于翻转课堂的双语教学改革研究及其在过程安全课程中的应用实践	王彦富	机电工程学院
QN201513	基于学生创新能力培养的测试技术层次化实验教学改革研究	张 辛	机电工程学院
QN201514	电工电子学课程初步翻转教学改革研究与探索	曹玉苹	信息与控制工程学院
QN201515	基于翻转课堂的自动控制原理课程教学研究	张 欣	信息与控制工程学院

项目编号	项目名称	负责人	所在单位
QN201516	工程教育专业认证背景下传感器原理课程双语教学体系研究	邢兰昌	信息与控制工程学院
QN201517	建筑力学课程 PDCA 模式教学改革探讨	张立松	储运与建筑工程学院
QN201518	基于竞赛模式的结构试验课程开放式试验教学研究	黄思凝	储运与建筑工程学院
QN201519	物联网专业基于 CDIO 工程教育模式探索	张晓东	计算机与通信工程学院
QN201520	促进个人知识形成的离散数学课程改革与实践	张红霞	计算机与通信工程学院
QN201521	融合通信专业知识的案例式程序设计教学模式探索	陈海华	计算机与通信工程学院
QN201522	基于计算思维的面向问题求解模式的教学改革研究	付文霞	计算机与通信工程学院
QN201523	能力培养导向的管理学课程体验式教学体系设计与实践	吕肖东	经济管理学院
QN201524	大班教学环境下经管类课程多维互动式教学改革与实践	刘 锴	经济管理学院
QN201525	以学生为中心的工程估价新建构主义教学改革	付 芳	经济管理学院
QN201526	基于学生创新能力培养的原子物理学教学改革与探索	周 伟	理学院
QN201527	基于微课的翻转课堂教学模式在高等数学教学中的应用研究	邢丽丽	理学院
QN201528	基本问题教学的结构化学课程探索	傅 惠	理学院
QN201529	基于“翻转课堂”理念的线性代数教学方法研究与实践	吴国丽	理学院
QN201530	高等数学教学中物理背景的案例研究	孙建国	理学院
QN201531	大学物理教学中应用演示实验的教学方法研究	展凯云	理学院
QN201532	项目化教学在分子物理课程中的探索与实践	王兆杰	理学院

6.8 参与山东省自然科学基金（ZR2019MEE095）

山东省自然科学基金
资助项目立项任务书

项目 基本 信息	项目名称	天然气水合物沉积物低频电极化机理与模型以及水合物饱和度计算方法研究				
	立项编号	ZR2019MEE095		项目类别	面上项目	
	执行期限	2019-07至2022-06		资助经费	12.00万元	
	学科分类	海洋资源开发利用		学科代码	E091005	
项目 承担 人 信息	姓名	邢兰昌	性别	男	身份证号	371427198302015535
	电子邮箱	xinglc@upc.edu.cn			联系电话	053286982918
	单位名称	中国石油大学（华东）			专业技术 职务	副教授
	所在单位(院系)	信息与控制工程学院测控技术与仪器系			主管部门	中国石油大学（华东）
	所在省级以上重点实验室		控制科学与工程重点学科			
项目组成员（与申请书一致，不包含主持人）						
姓名	职称	工作单位		任务分工	每年工作 时间（月）	签名
耿艳峰	教授	中国石油大学（华东）		研究方案论证与咨询	3	
华陈权	副教授	中国石油大学（华东）		实验方案设计论证与咨询	4	
王斌	讲师	中国石油大学（华东）		电磁场数值建模和仿真数据处理	6	
陈琳	讲师	中国石油大学（华东）		水合物饱和度模型建立	8	
曹胜昌	硕士研究生	中国石油大学（华东）		实验系统改造与模拟实验	10	
黄子轩	硕士研究生	中国石油大学（华东）		复电阻率数据Femix与模型建立	10	
贺世超	硕士研究生	中国石油大学（华东）		电磁场数值模拟与数据分析	10	
齐淑英	硕士研究生	中国石油大学（华东）		水合物饱和度模型建立	10	
需呈交科技报告（篇）						
年度进展报告				最终(技术)报告(必须填，一般为1)		
1				1		
注：严格按照科技报告的有关规定呈交科技报告。项目执行中，年度或中期审核前应呈交进展报告；项目完成后三个月内、开展验收前，须呈交最终（技术）报告。未完成科技报告任务的，项目不予结题。						

资助经费预算表 (单位: 万元)		
科目	预算经费	备注(计算依据与说明)
项目资助总额	12.00	
一、项目直接费用	10.00	
1、设备费	0.00	
(1)设备购置费	0.00	
(2)设备试制费	0.00	
(3)设备改造与租赁费	0.00	
2、材料费	3.70	四氢呋喃0.4万, 实验气体2.0万, 管路配件等1.3万。
3、测试化验加工费	0.00	
4、燃料动力费	0.00	
5、差旅/会议/国际合作与交流费	1.20	参加学术会议, 共3人次, 平均每人每次花费0.4万, 3人次×0.4万=1.2万。
6、出版/文献/信息传播/知识产权事务费	2.70	论文发表费1.5万, 发明专利申请相关知识产权事务费1.2万。
7、劳务费	2.40	参与项目的硕士研究生4人×10月/年×3年×0.02万/(人月)=2.4万。
8、专家咨询费	0.00	
9、其他支出	0.00	
二、项目间接经费 (比例:20%)	2.00	
1、绩效支出	1.40	项目组成员绩效支出, 间接费用减去单位管理费后结余的部分。
2、管理费	0.60	单位管理费, 总经费5%
3、房屋占用/日常水电气暖消耗	0.00	
三、自筹资金	0.00	
<p>项目负责人承诺: 本人接受山东省自然科学基金的资助, 并将严格遵守山东省自然科学基金委员会关于资助项目管理和财务管理的各项规定, 认真开展研究工作, 按照项目申请书中的内容完成各项指标。按时报送有关材料, 及时报告重大变动情况, 对资助项目发表的论著和取得的科研成果按规定进行标注。</p> <p>项目负责人签字: _____ 年 月 日</p>		
依托单位审核意见		山东省自然科学基金委员会办公室审查意见
<p>我单位同意承担该项目, 将保证项目负责人及其研究队伍的稳定和项目实施所需的条件, 严格遵守山东省自然科学基金委员会有关资助项目管理、财务等各项规定, 并做好督促协调工作。</p> <p style="text-align: right;">依托单位 (公章)</p> <p style="text-align: right;">年 月 日</p>		<p style="text-align: right;">(公章)</p> <p style="text-align: right;">年 月 日</p>

(正反面打印, 一式三份)

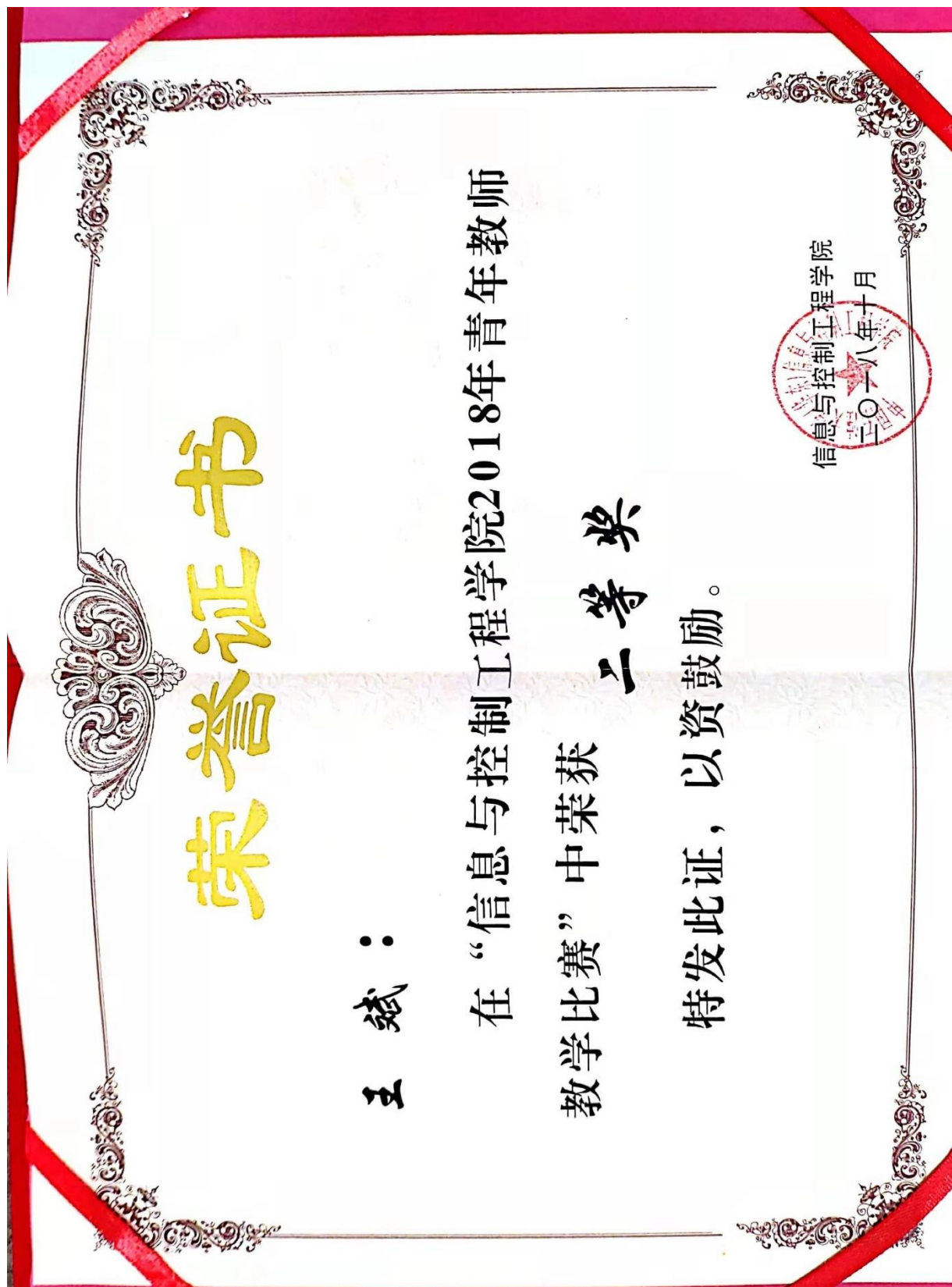
山东省自然科学基金委员会办公室2017年制

7. 教学比赛获奖证明材料

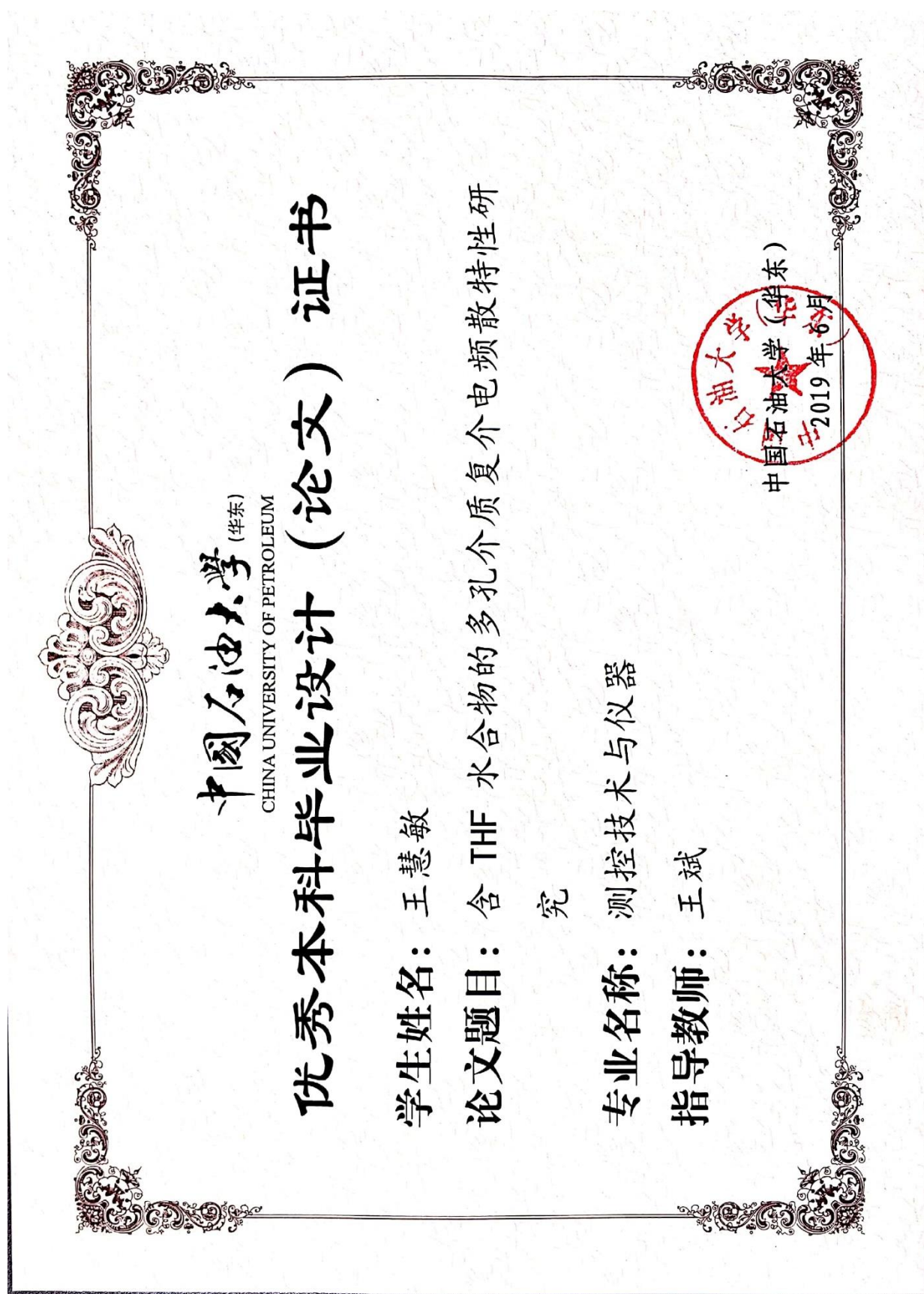
7.1 校级教学比赛获奖



7.2 院级教学比赛获奖



8. 指导学生学位论文获得校优秀论文



9. 参与平台、课程建设证明材料

9.1 作为骨干参与《测量仪表与自动化》在线开放课程建设

附件 1:

中国石油大学（华东） 在线开放课程立项申报书

课 程 名 称_____测量仪表与自动化_____

课程负责人_____孙 良_____

课 程 类 型_____学科基础课_____

所 在 单 位_____信息与控制工程学院_____

申 报 日 期_____2017-5-28_____

教务处制

二〇一七年五月

一、课程团队情况

课程负责人						
基本信息	姓名	孙良	性别	女	出生年月	1970-09
	学历	研究生	学位	博士	电话	13780689870
	职称	副教授	电子邮箱	sunl@upc.edu.cn		
授课情况	主讲课程名称		课程类别	授课对象	学时	学生数
	化工仪表		必修	化工	48	300
	过程控制仪表与装置		必修	自动化	48	120
	测量仪表与自动化		必修	储运	32	180
教学研究情况	1. 主持的教学研究课题（含课题名称、来源、年限，不超过 5 项）					
	年限	项目名称			来源	
	2014-2016	《测量仪表与自动化》课程研究性教学方法探索与实践			校级教改项目	
	2016-2018	混合教学模式的探索与实践			校级教改项目	
	2012-2014	《测量仪表与自动化》精品课程建设			校级教改项目	
	2014-2016	《过程控制仪表与装置》重点课程建设			校级教改项目	
	2016-2018	《过程控制仪表与装置》教材编写及出版			校级规划教材	
	2. 作为第一署名人发表的教学研究论文（含题目、刊物名称、时间，不超过 5 项）					
	时间	论文			期刊	
	2016.8	工科专业基础课研究性教学模式的探索与思考			《化工高等教育》	
	2016.10	研究性课堂教学模式的探索与实践			《电气电子教学学报》	
	2013.5	“测量仪表与自动化”教学方法改革的探索与实践			《中国电力教育》	
	2002.3	CAI 课件的设计与使用方法			《石油教育》	
	2002.5	考试改革的实践与思考			《石油教育》	
	3. 获得的教学表彰/奖励（不超过 5 项）					
	项目名称		授予单位	等级	排名	时间
《测量仪表与自动化》优秀教材		中国石油和化学工业联合会	一等	3	2015.03	
自动化专业工程时间教学新模式的研究与时间		中国石油大学	一等	3	2008.3	
过程控制仪表及装置教学改革与实践		中国石油大学	三等	2	2002.3	
自动调节装置 CAI 课件获优秀 CAI 软件		中国石油大学	二等	1	2001.10	
考试改革的实践与思考获优秀教育研究论文		中国石油大学	一等	1	2005.4	

课程团队及分工				
姓名	年龄	职称	学科专业	承担任务分工
孙良	47	副教授	控制理论与控制工程	课程负责人
涂玲	38	讲师	控制理论与控制工程	理论与实验教学
潘浩	38	讲师	控制理论与控制工程	理论与实验教学
王维波	40	讲师	固体地球物理学	理论与实验教学
王斌	29	讲师	无线电物理	理论与实验教学
宋曙芹	53	实验师	控制理论与控制工程	实验教学
马士腾	28	实验师	控制理论与控制工程	实验教学
陈卫红	50	高级实验师	计算机科学与工程	实验教学

关于公布学校2018年在线开放课程建设项目名单的通知

发布时间：2018-05-15 作者： 浏览次数：575

各教学院部：

为充分利用现代教育信息技术推进教学改革，促进我校优质教学资源开发和共享，学校组织开展了2018年在线开放课程立项工作。

经教师自主申报、学院推荐、学校评审，现公布立项名单（名单附后），并就有关事宜通知如下：

1. 在线开放课程以项目方式进行管理。学校负责立项课程全部制作经费，并按照课程建设进度及运行情况资助相应建设经费。
2. 学院加强对在线开放课程建设的指导和过程检查，确保各立项课程按时完成建设任务。
3. 各课程组按照立项申报书规划，优化课程设计，加快建设进度，力争2018年12月份前上线运行。

教务处

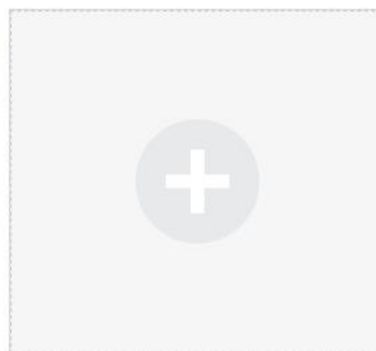
2018年5月15日

2018年在线开放课程立项名单

序号	课程名称	负责人	单位
1	沉积学	陈世悦	地球科学与技术学院
2	中外石油文化	张卫东	石油工程学院
3	科学精神与科学研究方法	蒲春生	石油工程学院
4	渗流力学	杜殿发	石油工程学院
5	化学反应工程	刘会娥	化学工程学院
6	工程材料学	王彦芳	机电工程学院
7	机械CAD基础	牛文杰	机电工程学院
8	设计改变生活	金 涛	机电工程学院
9	测量仪表与自动化	孙 良	信息与控制工程学院
10	电力拖动自动控制系统	冯兴田	信息与控制工程学院
11	电路分析	马文忠	信息与控制工程学院
12	电路与模拟电子技术	张冬至	信息与控制工程学院
13	输油管道设计与管理	刘 刚	储运与建筑工程学院
14	钢结构原理	高福聚	储运与建筑工程学院
15	计算机操作系统	李华昱	计算机与通信工程学院
16	大学计算机	李 昕	计算机与通信工程学院
17	创造学基础	寇瑞红	经济管理学院
18	创业基础	安贵鑫	经济管理学院
19	数学八讲	王 涛	理学院
20	量子力学	孙 强	理学院
21	近代物理实验	周丽霞	理学院
22	大学物理	刘 冰	理学院
23	犯罪学	冷 凌	文学院



我教的课 | 我学的课



注：实际负责理论授课，课程资源整合，课程网站建设、维护，网络课程录像等实质性工作。

9.2 主持《测控技术与测控网络系统》、《电磁场与微波技术》在线课程建设



中国石化大学(华东)
CHINA UNIVERSITY OF PETROLEUM

石大云课堂

请输入课程名称或编号

退出

[主页](#)
[我的课程](#)
[课程排行](#)
[资源中心](#)
[课程联盟](#)
[帮助中心](#)



王斌

登录时间: 2020-01-05 15:53
在线总时长: 50小时45分
登录次数: 69

安全设置

互动提醒

- 1门课程有未读课程通知
- 1门课程有待批测试
- 2门课程有未批选课申请
- 1门课程有需要解管的问题
- 17个系统通知未读

最新资源

通知公告

- 2019-09-05 如何在云课堂开设新课---“教务选课”功能介绍
- 2019-02-22 石大云课堂新版软件V8.0使用指导
- 2019-02-22 石大云课堂新版V8.0手机端软件下载
- 2019-11-08 理学院第二届“教学活动月”系列报告之一
- 2019-07-03 “石大云课堂”教学平台培训通知

日程安排

一月 2020

Su	Mo	Tu	We	Th	Fr	Sa
29	30	31	1	2	3	4
5	6	7	8	9	10	11
12	13	14	15	16	17	18
19	20	21	22	23	24	25
26	27	28	29	30	31	1

课程列表



测控技术与测控网络系统

课程编号: 05122120
主讲教师: 王斌

课程管理 课程预览



测量仪表与自动化

课程编号: 05101120
主讲教师: 王斌

课程管理 课程预览



电磁场与微波技术

课程编号: 05354120
主讲教师: 王斌

课程管理 课程预览

电磁场与微波技术

编号: 05354120 主讲教师: 王斌

[教学管理](#)
[课程建设](#)
[学习分析](#)
[课程预览](#)
[系统帮助](#)

栏目设置

- 课程学习
- 课程资源
- 基本信息
- 单元学习
- 课程活动
- 随堂教学

页面样式

>> 课程资源

课程资源

- 电磁场与微波技术
 - 知识点拓展
 - 课堂讲述ppt
 - 回收站
 - 名词解释
 - 相关英文书籍

新建目录 在线编辑 上传文件 添加URL 引用资源中心 导入资源 移动

电磁场与微波技术 返回上一级目录

目录名称	属性	操作	状态
知识点拓展			发布
课堂讲述ppt			发布
回收站			发布
名词解释			发布
相关英文书籍			发布

附件 2

国家级一流本科课程申报书 (2019 年)

课程名称：测量仪表与自动化

专业类代码：0000

授课教师（课程负责人）：孙良

联系电话：13780689870

申报类型：☐线下一流课程

☒线上线下混合式一流课程

☐社会实践一流课程

申报学校：中国石油大学（华东）

推荐单位：

填表日期：

中华人民共和国教育部制
二〇一九年十一月

一、课程基本信息





(一) 线下一流课程

课程名称			
课程编码+选课编码 (教务系统中的编码)			
课程类型	<input type="radio"/> 文化素质课 <input type="radio"/> 公共基础课 <input type="radio"/> 专业课	<input type="checkbox"/> 实验课	
课程性质	<input type="radio"/> 必修 <input type="radio"/> 选修		
开课年级			
面向专业			
学 时			
学 分			
先修(前序)课程名称			
后续课程名称			
主要教材	书名、书号、作者、出版社、出版时间(上传封面及版权页)		
最近两期开课时间	2018年9月1日—2019年1月15日(上传教务系统截图)		
	2019年3月1日—2019年7月1日(上传教务系统截图)		
最近两期学生总人数			

注:(教务系统截图须至少包含课程编码、选课编码、开课时间、授课教师姓名等信息)

(二) 线上线下混合式一流课程

课程名称	测量仪表与自动化		
课程编码 (教务系统中的编码)	05101120 测量仪表与自动化(限选) 05119120 化工仪表(必修) BY05102301 化工仪表及自动化(必修)		
课程类型	<input type="radio"/> 文化素质课 <input type="radio"/> 公共基础课 <input checked="" type="radio"/> 专业课	<input type="checkbox"/> 实验课	
课程性质	<input checked="" type="radio"/> 必修 <input checked="" type="radio"/> 选修		
开课年级	二年级(建环)/三年级(化工、储运、能动、能源化工)		
面向专业	化工、储运、建环、能动、能源化工		
学 时	总学时: 32 线上学时: 课堂学时: 20		
学 分	2		
先修(前序)课程名称	电工电子学、流体力学、化工原理		
后续课程名称	测量仪表与自动化课程设计		
主要教材	书名、书号、作者、出版社、出版时间(上传封面及版权页)		

	<p>测量仪表与自动化，杜鹃、廖明燕、孙良、王钊；中国石油大学出版社；2013年9月</p>  
最近两期开课时间	<p>2018年9月1日— 2019年1月15日（上传教务系统截图）</p>  <p>2019年3月1日— 2019年7月1日（上传教务系统截图）</p> 
最近两期学生总人数	469
使用的在线课程	<p>○国家精品在线开放课程及名称 ○国家虚拟仿真实验教学一流课程及名称 ●否（填写课程名称、学校、负责人、网址） 《测量仪表与自动化》，中国石油大学，孙良， https://mooc1-1.chaoxing.com/course/courseOutline?courseId=205292624&edit=true 使用方式： ●MOOC ○SPOC</p>

注：（教务系统截图须至少包含课程编码、选课编码、开课时间、授课教师姓名等信息）

（三）社会实践一流课程

课程名称	
课程编码 (教务系统中的编码)	

课程类别	<input type="radio"/> 创新创业类 <input type="radio"/> 思想政治理论课类 <input type="radio"/> 专业类 <input type="radio"/> 其他（填写）
课程性质	<input type="radio"/> 必修 <input type="radio"/> 选修
开课年级	
面向专业	
实践基地	名称及所在地：
学 时	总学时： 理论课学时： 实践学时：
学 分	
最近两期开课时间	年 月 日— 年 月 日（上传教务系统截图）
	年 月 日— 年 月 日（上传教务系统截图）
最近两期学生总人数	

注：（教务系统截图须至少包含课程编码、选课编码、开课时间、授课教师姓名等信息）

二、授课教师（教学团队）

课程团队主要成员								
（序号 1 为课程负责人，课程负责人及团队其他主要成员总人数限 5 人之内）								
序号	姓名	单位	出生年月	职务	职称	手机号码	电子邮箱	教学任务
1	孙良	控制	1970.9		副教授	13780689870	sunli@upc.edu.cn	网站建设、授课
2	涂玲	控制	1979.9		讲师	18560643590	tuling@upc.edu.cn	网站建设、授课
3	潘浩	控制	1979.9		讲师	13969863327	upc_panhao@126.com	网站建设、授课
4	王维波	控制	1977.2		讲师	18561517236	wangwb@upc.edu.cn	网站建设、授课
5	王斌	控制	1988.1		讲师	18562872097	wangbin2015@upc.edu.cn	网站建设、授课
授课教师（课程负责人）教学情况（300 字以内）								
（教学经历：近 5 年来在承担学校教学任务、开展教学研究、获得教学奖励方面的情况） 1、承担的教学任务 <p>近 5 年，承担化工专业《化工仪表》课程，建环专业《测量仪表与自动化》和《测量仪表与自动化课程设计》，自动化专业《过程控制仪表与装置》、《工业网络控制系统》等课程。</p> 2、主持教改项目								

10. 参加国际学术会议证明材料

PIERS 2017 in Singapore

Progress In Electromagnetics Research Symposium

Dr. Eng Leong Tan
School of Electrical and Electronic Engineering
Nanyang Technological University
50 Nanyang Ave, Singapore 639798
Email: eeltan@ntu.edu.sg
Tel: +65 67906190
Fax: +65 67933318

November 16, 2017

Dr. Bin Wang
College of Information and Control Engineering
China University of Petroleum
QingDao, ShanDong
China

Dear Dr. Bin Wang

It is our pleasure to inform you that PIERS 2017 in Singapore has accepted the following article(s) to be presented in the conference:

- 170619125306: Numerical Study on Complex Resistivity Measurement of Porous Media Containing Gas Hydrate

I am writing to cordially invite you to participate in the coming Progress in Electromagnetics Research Symposium (PIERS) to be held on November 19–22, 2017 in Singapore. Each participant should complete the registration process for the symposium and pay non-refundable registration fee. There is no financial subsistence provided for our invitees.

For detailed information on the symposium, program updates, registration fee, etc., please visit the symposium website at
<http://www.piers.org/piers2017Singapore/>

We very much look forward to your participation at PIERS 2017 in Singapore.

On behalf of the Organizing Committee,

Sincerely,



Eng Leong Tan
General Chair
PIERS 2017 in Singapore



注：参会是与 IEEE FELLOW 日本东北大学佐藤源之教授合影

Session 2A8
FocusSession.SC5: Inverse Problems for
Scientific, Industrial and Biomedical
Applications 2

Tuesday AM, November 21, 2017

Room LT14

Organized by Cheng-Gang Xie, Xudong Chen

Chaired by Cheng-Gang Xie, Xudong Chen

- 09:00 Numerical Study on Complex Resistivity Measurement of Porous Media Containing Gas Hydrate
Bin Wang (China University of Petroleum); Lanchang Xing (China University of Petroleum);
- 09:20 Permittivity Imaging Method by Incorporating Range Points Migration and Ellipsometry for UWB Short Range Radar
Tatsuo Takatori (The University of Electro-Communications); Yong Huang (Fuji Electric Co., Ltd.); Takahiro Kudo (Fuji Electric Co., Ltd.); Shouhei Kidera (University of Electro-Communications);
- 09:40 Super-resolution Doppler Velocity Estimation by Gaussian-kernel Based Range-Doppler Conversion for UWB Radar
Masafumi Setsu (The University of Electro-Communications); Shouhei Kidera (University of Electro-Communications);



注：于 2017 年 11 月 21 日上午九点做题为“Complex Resistivity Measurement of Porous Media Containing Gas Hydrate”的会议报告

11. 其他证明材料

11.1 青年教师卓越教学能力培养计划

结业证书

编号: 201806004039

王 斌:

圆满完成中国石油大学（华东）
青年教师卓越教学能力培养计划
所有培训内容，准予结业。

中国石油大学（华东）教师教学发展中心
2018年6月

培训内容

项目	内 容	主讲人
专题讲座	站讲台，做引路人	中山大学 王金发
	移动互联网时代教学实践与案例创新分享	华中师大 田 媛
	高教研究论文写作	西南交大 闫月勤
	校教学名师讲坛	学校教学名师
教学工作坊	思维科学与有效教学	思维专家 吴亚滨
	对分课堂实践探索	石工学院 张卫东
	教学科研互动发展，促进学科建设水平提升	机电学院 刘永红
视频自学	浅谈驾驭课堂的动力与能力	华中农大 郑用睦
课堂观摩	基于 MOOC/SPOC 的课程教学改革	哈工大 战德臣
	应用物理化学	石工学院 贾 寒
	材料物理	理学院 甄玉花
校外交流	“知识-素质-能力”三位一体课堂教学观摩与研讨会（自愿申请）	
教学诊断	教学录像分析（自愿申请）	
教学研讨	教学改革经验分享	
结业总结	总结研讨学习收获及体会	



11.3 积极参加集体活动，代表学院取得优异成绩

